HYPERVELOCITY IMPACT WITH FLOW AND SHOCK PENETRATION THROUGH FLUID, PLASTIC, AND ELASTIC ZONES

By

BOB ADRIAN HARDAGE

Bachelor of Science
Oklahoma State University
Stillwater, Oklahoma
1961

Master of Science
Oklahoma State University
Stillwater, Oklahoma
1967

Submitted to the Faculty of the Graduate College
of the Oklahoma State University
in partial fulfillment of the requirements
for the degree of
DOCTOR OF PHILOSOPHY
May, 1967

HYPERVELOCITY IMPACT WITH FLOW AND SHOCK

PENETRATION THROUGH FLUID, PLASTIC,

AND ELASTIC ZONES

Thesis Approved:

Francis C. Todd
Thesis Adviser

Leon W. Schroeder

William J. Leiss

John E. Moore

N N Durham
Dean of the Graduate College

PREFACE

This work presents a complete numerical solution of the hypervelocity impact of a microparticle on an aluminum surface. The solution follows the flow from the instant of contact and continues until inviscid fluid flow is not a valid assumption. The shock in the inviscid region couples to the plastic region, and that in turn couples to the elastic region. The monitoring of the motion of the physical boundaries of the target and impacting projectile is an important part of the complete solution.

Dr. F. C. Todd acted as my advisor and guide throughout the study. I owe this man more than I can ever repay; the completion of the problem was a result of his wisdom and patience.

The problem involved many hours of computer time. I am grateful to W. M. Alexander and Otto Berg for arranging computer time at Goddard Space Flight Center. Mr. W. F. Cahill of the Theoretical Division at Goddard, and his secretary, Mrs. White, were very helpful to me during my stays there. The long nights with the computers were made enjoyable because of the courtesies extended by Mr. Elmer Terry and his staff of operators: Jim Ridgeley, Sterling Gilmore, Jim Green, and G. Griffith.

Computer programs always involve much "debugging" time. I wish to thank K. O. Baker, Ken Slavin and their staff of operators for arranging many short "debugging" runs on the computer at Continental Oil Company, Ponca City, Oklahoma. Mrs. Marylynn Luther of Conoco was of

much assistance in the removal of these "bugs". Mr. Sam Wax and Mr. McEaddy were also of much help in finding certain "bugs" while at Goddard.

Credit should be extended to Dr. B. A. Sodek, who preceded me in this work. He solved the early time behavior of the impact when the inviscid fluid approximation is valid, and much of his program was incorporated into the present version.

I am grateful to Mr. S. E. Elliott of Phillips Petroleum Company for allowing me to complete the thesis while working for Phillips and for his encouragement during the trying times of converting the computer printout into meaningful physical answers. Don Goff of Phillips prepared several of the figures in the text.

The work was supported by NASA contract NASr-7 which is administered through the Research Foundation of Oklahoma State University.

TABLE OF CONTENTS

TABLE OF CONTENTS (Continued)

LIST OF TABLES

LIST OF FIGURES

LIST OF FIGURES (Continued)

LIST OF FIGURES (Continued)

LIST OF FIGURES (Continued)

CHAPTER I

INTRODUCTION AND STATEMENT OF THE PROBLEM

Several interesting phenomena are observed when a small particle moving at hypersonic velocity strikes a metal surface (8). Very soon after impact a light flash is emitted, and after this flashing the impact creates a crater several times larger than the projectile. The time at which the light is emitted and the size of the crater depend upon the size of the impacting particle. The crater usually has a raised, curled lip around its periphery. During the crater formation, high speed photography reveals that a fine, high velocity spray is ejected from the circumference of the crater.

Micrometeoroids are small, rapidly moving particles in outer space which have a mass of less than 10^{-4} gram and velocities that range from 30,000 to 240,000 feet per second. The smallest stable volume of a crystal is approximately thirty molecules, so the mass of these micro-particles could be as small as 10^{-20} or 10^{-21} gram. Those particles with a mass that is less than 10^{-11} or 10^{-12} gram are pushed beyond the earth's orbit by the excess of radiation pressure from the sun over the gravitational force.

Donn has reported that meteor residue should have a generally spherical shape and should be composed of iron-nickel alloys or silicate minerals, and the latter are mainly enstatite or olivine (12). Donn also states that penetration measurements made by Explorer XVI for

particles in the 10^{-9} gram range are one to two orders of magnitude below "microphone measurements" for these same particles. "Microphone measurements" refer to the detector for micrometeoroids that is mounted on many space vehicles. This discrepancy would arise from impacts of two different kinds of particles: fluffy and compact. All terrestial samples of space particles, called micrometeorites, are compact, but evidently, porous particles are much more numerous in space.

The NASA project which has supported this thesis began as an analytical study of micrometeoroid impact on a plane aluminum surface. Dr. F. C. Todd, project supervisor, has prepared a model of hypervelocity impact which includes: 1) the formation of a plasma from the impacting particle and the aluminum target, and 2) the creation of strong shock waves that move radially from the point of impact out into the aluminum target and back into the impacting micrometeoroid.

The transition of the hot plasma back to its normal state results in the light flash because some energy is lost by means of visible and UV radiation. The shock waves initiate a fluid flow that ejects some target material to create the crater.

Lake reported on a theoretical solution to the shock propagation problem (18). Sodek make a theoretical study of the properties of the impact of a spherical micrometeoroid on a semi-infinite aluminum target (32). Bruce devised a theoretical determination of the essential properties of an exploding aluminum plasma (7). Lake and Sodek confirm the assumptions of the proposed impact model. In particular, their work predicts that pressures of several megabars are created by the impact. At such pressures, the target and projectile are converted

into a hot, dense plasma; and any material movement can initially be described as nonviscous, hydrodynamic flow. Experimental work is in progress to verify these theoretical findings.

Statement of the Problem

This thesis is concerned with extending the theoretical studies of shock wave propagation and crater formation that result from hypervelocity impact. Both Lake and Sodek assumed inviscid hydrodynamic flow. Sodek solved the problem of a normal density aluminum sphere impacting on an aluminum surface. This thesis examines the impact of a porous, spherical rock upon an aluminum surface, and the solution is extended beyond the time when inviscid hydrodynamic flow is a valid assumption.

At time T=0.0, a porous stone micrometeoroid is assumed to have just made contact with the aluminum target. The target is at rest, and the micrometeoroid is moving toward the target at a velocity V. The appropriate dynamical equations are solved, numerically, to give:

1. The size of the crater created by the impact.
2. An estimate of the mass, momentum, and energy of the material ejected from the crater.
3. The behavior of the shock-wave propagation in the fluid, plastic, and elastic zones of the aluminum target.
4. The deformation of the micrometeoroid.

Presentation of the Problem

The theory of shock waves and the equations needed to describe the

impact process are discussed in Chapter II. Appropriate dynamical equations are developed for use with the fluid, plastic, and elastic states of aluminum.

Equations of state are described for these three states of aluminimum and also for the porous, stone micrometeoroid. The viscosity function which is required to describe plastic flow is included in the discussion.

The conversion of the necessary equations to finite difference form is discussed in Chapter III. The finite difference techniques, that allow the physical boundaries of the problem to be accurately monitored, are discussed in detail.

The solutions are presented in Chapter IV in the form of crater and pressure profiles. Five groups of solutions are given; each group for a specific value of micrometeoroid density and velocity. The five impact cases are:

impact velocity = 6.25 km/sec	density = 2.0 gm/cc
impact velocity = 7.5 km/sec	density = 2.0 gm/cc
impact velocity = 20 km/sec	density = 2.0 gm/cc
impact velocity = 20 km/sec	density = 0.5 gm/cc
impact velocity = 72 km/sec	density = 0.5 gm/cc

One solution is obtained that compares the impact of a micrometeoroid of radius R with a micrometeoroid of radius 1.5 R.

CHAPTER II

DYNAMICAL EQUATIONS

Conservation Equations

The equations expressing conservation of mass, momentum, and energy are the fundamental dynamical equations used in this study. These equations can be expressed in two different forms depending upon the type of coordinate frame that is employed for reference. The Eulerian coordinate frame describes the values of the flow variables at fixed points in space. Such a coordinate frame is fixed, and the material moves through the stationary space points of the coordinate system. The Lagrangian coordinate system describes dynamical variables in terms of the motion of individual elements of the material. This type of reference frame is not fixed in space but moves with the material. In two and three dimensional problems, the Eulerial representation is preferred from both a mathematical and a physical point of view.

Derivations of the conservation equations can be found in many books; e. g., Bird, et al., (5) or Handbook of Physics (10). In their vector form, the equations in Eulerian coordinates are:

conservation of mass, or the conservation equation

$$(1) \quad \frac{D\rho}{Dt} + \rho \vec{\nabla} \cdot \vec{V} = 0$$

conservation of momentum, or the equation of motion

$$(2) \quad \rho \frac{D\vec{V}}{Dt} + \vec{\nabla} p - \vec{\nabla} \cdot \vec{S}_{ij} = 0$$

conservation of energy, or the energy equation

$$(3)\quad \rho \frac{DE}{Dt} + \vec{\nabla}\cdot(p\vec{V}) - \vec{\nabla}\cdot(S_{ij} V_i) = 0$$

This form for the energy equation was derived by Steward (36) by the assumption of adiabatic energy flow. With this equation to describe the behavior of a shocked material, the decompression and any subsequent compression of the material remains on a single adiabat. This equation does not affect the increase in entropy by the initial shock front.

The velocity vector, $\vec{V}$, of the material under consideration has the components (v_i, v_j, v_k), ρ is the density, p is the pressure, and E is the total energy. These four variables, V, ρ, p, and E, are dependent variables, so a fourth equation is needed in order to obtain a solution. The fourth equation is the equation of state, and it is discussed later in this chapter.

Several other terms should be explained. The operator, $\frac{D}{Dt}$, is defined by the following relation.

$$(4)\quad \frac{D}{Dt} = \frac{\partial}{\partial t} + \vec{v}\cdot\vec{\nabla}$$

The quantity, S_{ij}, is the stress tensor. For inviscid fluid flow, $S_{ij}=0$. For plastic, or viscous flow, it is given by

$$(5)\quad S_{ij} = \left(\eta_B - \tfrac{2}{3}\eta\right) d_{ij}\delta_{ij} + 2\eta\, d_{ij}$$

Where η_B is the bulk viscosity, η is the shear viscosity, and δ_{ij} is the Kronecker delta. It is generally assumed that $\eta_B=0$ (11). The d_{ij} are the strain rate components

$$(6) \quad d_{ij} = \frac{1}{2}\left(\frac{\partial v_i}{\partial x_j} + \frac{\partial v_j}{\partial x_i}\right)$$

If the material is elastic and not strained above its elastic limit, then the following relation is employed for S_{ij}

$$(7) \quad S_{ij} = \lambda e_{ij} \delta_{ij} + 2\mu e_{ij}$$

The constant, μ, is the modulus of rigidity, and λ is Lame's lambda. The values of the tensor, e_{ij}, are the strain components

$$(8) \quad e_{ij} = \frac{1}{2}\left(\frac{\partial r_i}{\partial x_j} + \frac{\partial r_j}{\partial x_i}\right)$$

The r_i and r_j are the components of the displacement vector of the material resulting from plastic deformation, only. A uniform body displacement from the body moving through space at constant velocity does not affect the magnitudes of r_i and r_j.

The Rankine-Hugoniot Equations

The shock front appears in the dynamical equations as the positions at which the velocity, the density, and the other dependent variables are discontinuous. It is necessary to have conditions that relate the state of the material on one side of the shock front to the state on the other side. These conditions are called the Rankine-Hugoniot jump conditions.

Bradley (6) gives a good derivation of these jump equations. In essence, the equations simply state the conservation of mass, momentum, and energy. Let p_o, ρ_o, and E_o be the values of the pressure, the density and the specific internal energy ahead of the shock front, and

p_1 , ρ_1 , and E_1 be the values behind the front. Assume that the material ahead of the front is at rest, that the front moves at a velocity V, and that the material behind the front moves with a velocity u_1. The Rankine-Hugoniot equations are then

conservation of mass flow

$$\rho_0 V = \rho_1 (V - u_1) \tag{9}$$

conservation of momentum

$$p_1 - p_0 = \rho_0 V u_1 \tag{10}$$

conservation of energy flow

$$p_1 u_1 = \tfrac{1}{2} \rho_0 V u_1^2 + \rho_0 V (E_1 - E_0) \tag{11}$$

A fourth boundary condition must be included in the Rankine-Hugoniot conditions, and this condition is that the entropy must increase across a shock front. An entropy increase occurs across a shock front because more energy is expended in shock compression than is expended in an adiabatic compression. Any equation of state to describe shock compression must account for this increase in entropy.

These above, Rankine-Hugoniot equations relate the variables on the two sides of a shock front, and the Eulerian dynamical equations relate the variables at points away from the shock front. A shock wave propagation problem may be solved with the Rankine-Hugoniot equations as boundary conditions at the shock front. This technique is called shock fitting, and it is a cumbersome way to obtain a solution. If the shock front is changed from a true discontinuity to a narrow region in which all variables have large but continuous gradients, then it is not necessary to use the shock fitting technique. The Rankine-Hugoniot

equations still hold, but their explicit use as boundary conditions is not needed. This technique was suggested by J. von Neumann and R. D. Richtmyer (37).

In the plastic and elastic regions of aluminum, the smearing out of the shock front is accomplished by including the viscous effects of the stress tensor in the equations of motion and the energy equation.

In the early stages of the impact process, when inviscid fluid flow may be assumed, this smearing of the shock is accomplished by introducing a psuedo viscosity effect. This effect is an artificial dissipation that is added to the pressure. A form for the artificial dissipation was suggested by Landshoff (20), and it has the form

$$(12) \qquad q = -C_1^2 \vec{\nabla}\cdot\vec{V}\left(C_2 + |\vec{\nabla}\cdot\vec{V}|\right)$$

C_1 and C_2 are adjustable constants, and V is the material velocity vector. The psuedo viscosity effect is obtained by replacing p in the fluid flow equations by the sum (p + q). The value of q is always chosen as positive for compression; i.e., when $\vec{\nabla}\cdot\vec{V} < 0$. It is made equal to zero for expansion; i.e., when $\vec{\nabla}\cdot\vec{V} > 0$.

Equations for Fluid Region

When a micrometeoroid strikes an aluminum surface at hypervelocity, pressures of several million atmospheres are created in both the aluminium and the micrometeoroid (18), (32). At such pressures, both materials may be treated analytically, as inviscid fluids. When inviscid fluid flow is assumed, the dynamical equations simplify to

$$(13) \qquad \frac{\partial \rho}{\partial t} = -\nabla(\rho \vec{V})$$

$$(14) \qquad \rho\left(\frac{d\vec{V}}{dt} + (\vec{V}\cdot\nabla)\vec{V}\right) = -\vec{\nabla}p$$

$$(15) \qquad \rho\left(\frac{dE}{dt} + (\vec{V}\cdot\nabla)E\right) = -\nabla\cdot(p\vec{V})$$

These equations are in Cartesian coordinates. In agreement with the preceding members of this group at O. S. U., the solution for the considerably expanded problem in this thesis was solved in spherical coordinates. In spherical coordinates, the conservation of mass equation assumes the following form.

$$(16) \qquad \frac{\partial\rho}{\partial t} = -\frac{1}{r^2}\frac{\partial}{\partial r}(r^2\rho u) - \frac{1}{r\sin\theta}\frac{\partial}{\partial\theta}(\rho w\sin\theta)$$

The equation for the conservation of momentum reduces to two equations which are for radial and polar flow. The azimuthal, or longitudinal flow is assumed to be zero; i.e., in the velocity relation, V(u,w,v), V_ϕ is zero so the relation for the velocity becomes V(u,w,0). The other two components of the velocity are u_r and w_θ. In the discussion of the conversion of the equations to the polar form with this restriction on the velocity, the following vector identity is useful

$$(17) \qquad (\vec{V}\cdot\nabla)\vec{V} = \frac{1}{2}\vec{\nabla}V^2 - \vec{V}\times\vec{\nabla}\times\vec{V}$$

When v_ϕ is set equal to zero

$$(18) \qquad \frac{1}{2}\vec{\nabla}V^2 = \frac{1}{2}\vec{r}_0\frac{\partial}{\partial r}(u^2+w^2) + \frac{1}{2}\vec{\theta}_0\frac{1}{r}\frac{\partial}{\partial\theta}(u^2+w^2)$$

and

$$(19)\quad \vec{\nabla}\times\vec{\nabla}\times\vec{v} = \vec{r}_o\left[\omega\frac{\partial\omega}{\partial r}+\frac{\omega^2}{r}-\frac{\omega}{r}\frac{\partial u}{\partial\theta}\right] - \vec{\theta}_o\left[u\frac{\partial\omega}{\partial r}+\frac{\omega u}{r}-\frac{u}{r}\frac{\partial u}{\partial\theta}\right]$$

Substitute the identity in Equation 17 into Equation 14 and use Equations 18 and 19 to evaluate $(\vec{v}\cdot\vec{\nabla})\vec{v}$. The radial component of the resulting equation for flow in the radial direction, r_o, becomes

$$(20)\quad \rho\frac{\partial u}{\partial t}+\rho u\frac{\partial u}{\partial r}+\rho\frac{w}{r}\frac{\partial u}{\partial\theta}-\rho\frac{\omega^2}{r} = -\frac{\partial p}{\partial r}$$

Multiply the relation for the conservation of mass, Equation 16, by u and add the resulting relation to Equation 20. After these manipulations, the radial component for the equation of motion may be written

$$(21)\quad \frac{\partial(\rho u)}{\partial t} = -\frac{1}{r^2}\frac{\partial}{\partial r}(r^2\rho u^2) - \frac{1}{r\sin\theta}\frac{\partial}{\partial\theta}(\rho w u\sin\theta) + \rho\frac{\omega^2}{r} - \frac{\partial p}{\partial r}$$

Return to Equations 17, 18, and 19 and the polar, or θ, component of the equation of motion may be written

$$(22)\quad \rho\frac{\partial w}{\partial t}+\rho\frac{w}{r}\frac{\partial w}{\partial\theta}+\rho u\frac{\partial w}{\partial r}+\frac{\rho w u}{r} = -\frac{1}{r}\frac{\partial p}{\partial\theta}$$

Multiply the conservation equation by w, add the result to Equation 22 and the angular equation of motion becomes

$$(23)\quad \frac{\partial(\rho w)}{\partial t} = -\frac{1}{r^2}\frac{\partial}{\partial r}(r^2\rho u w) - \frac{1}{r\sin\theta}\frac{\partial}{\partial\theta}(\rho w^2\sin\theta) - \frac{\rho w u}{r} - \frac{1}{r}\frac{\partial p}{\partial\theta}$$

The energy equation may be written

$$(24)\quad \rho\frac{\partial E}{\partial t}+u\frac{\partial E}{\partial r}+\frac{w}{r}\frac{\partial E}{\partial \theta}=-\frac{1}{r^2}\frac{\partial}{\partial r}(r^2 p u)-\frac{1}{r\sin\theta}\frac{\partial}{\partial \theta}(p w \sin\theta)$$

Multiply the conservation Equation 16 by E, add to 24, and the energy equation becomes

$$\frac{\partial(\rho E)}{\partial t}=-\frac{1}{r^2}\frac{\partial}{\partial r}(r^2\rho u E)-\frac{1}{r\sin\theta}\frac{\partial}{\partial \theta}(\rho w E \sin\theta)$$

$$(25)\qquad -\frac{1}{r^2}\frac{\partial}{\partial r}(r^2 p u)-\frac{1}{r\sin\theta}\frac{\partial}{\partial \theta}(p w \sin\theta)$$

Equations 16, 21, 23, and 25 are the forms of the dynamical equations that are used to describe the inviscid fluid flow which occurs early in the impact process. The equations are now in the "conservative" form which converts easily into accurate finite difference equations. The psuedo viscosity term, q, can be added to the pressure p in these equations in order to smear out the shock front and remove the jump discontinuity across the front.

The equation of state used for the fluid flow region is discussed in a later section of this chapter.

Equations for Plastic Region

The inviscid fluid model is not valid after the shock wave pressure has decreased to a magnitude of one to two hundred kilobars. This transition occurs after the shock wave has propagated a distance of two to several micrometeoroid radii into the aluminum target. The exact

distance depends on the initial velocity and mass. The appropriate model for this region is the plastic flow model.

The stress tensor in the equation of motion and in the energy equation must be evaluated in order to accurately describe plastic flow. The divergence of the stress tensor is given by the following relation (3).

$$\begin{aligned} div\ S_{ij} = {} & \frac{1}{3}\eta\,\vec{\nabla}(\vec{\nabla}\cdot\vec{V}) + \eta\,\nabla^2(\vec{V}) - \frac{2}{3}(\vec{\nabla}\cdot\vec{V})\,\vec{\nabla}\eta \\ & + 2\,(\vec{\nabla}\eta\cdot\vec{\nabla})\,\vec{V} + \vec{\nabla}\eta\times(\vec{\nabla}\times\vec{V}). \end{aligned} \tag{26}$$

where $\vec{v}$ is the material velocity, and η is the viscosity.

The radial, or r, component of this divergence must be added to the radial equation of motion in Equation 21, and the tangential, or , component must be added to Equation 23. In Appendix A, it is shown that the equations of motion are

$$\begin{aligned} \frac{\partial(\rho u)}{\partial t} = {} & -\frac{\partial(r^2\rho u^2)}{r^2\,\partial r} - \frac{\partial(\rho\omega r\sin\theta)}{r\sin\theta\,\partial\theta} + \rho\frac{w^2}{r} \\ & - \frac{\partial p}{\partial r} + \frac{1}{3}\eta\frac{\partial}{\partial r}\left[\vec{\nabla}\cdot\vec{V}\right] + \eta\left[\frac{1}{r^2}\frac{\partial}{\partial r}\left(r^2\frac{\partial u}{\partial r}\right)\right. \\ & \left. + \frac{1}{r^2\sin\theta}\frac{\partial}{\partial\theta}\left(\frac{\partial u}{\partial\theta}\sin\theta\right) - \frac{2u}{r^2} - 2\frac{\partial(w\sin\theta)}{r^2\sin\theta\,\partial\theta}\right] \\ & - \frac{2}{3}\frac{\partial\eta}{\partial r}\left[\vec{\nabla}\cdot\vec{V}\right] + 2\frac{\partial\eta}{\partial r}\frac{\partial u}{\partial r} + \frac{2}{r^2}\frac{\partial\eta}{\partial\theta}\frac{\partial u}{\partial\theta} \\ & + \frac{1}{r^2}\frac{\partial\eta}{\partial\theta}\left[\frac{\partial}{\partial r}(rw) - \frac{\partial u}{\partial\theta}\right] \end{aligned} \tag{27}$$

and

$$\frac{\partial(\rho w)}{\partial t} = -\frac{(\rho w^2 \sin\theta)}{r \sin\theta \partial\theta} - \frac{\partial(r^2 \rho u w)}{r^2 \partial r} - \frac{\rho u w}{r}$$

$$- \frac{1}{r}\frac{\partial p}{\partial \theta} + \frac{1}{3}\eta \frac{1}{r}\frac{\partial}{\partial\theta}\left[\vec{\nabla}\cdot\vec{V}\right]$$

$$+ \eta\left[\frac{1}{r^2}\frac{\partial}{\partial r}\left(r^2\frac{\partial w}{\partial r}\right) + \frac{1}{r^2\sin\theta}\frac{\partial}{\partial\theta}\left(\frac{\partial w}{\partial\theta}\sin\theta\right)\right.$$

(28)

$$\left. - \frac{w}{r^2\sin^2\theta} + \frac{2}{r^2}\frac{\partial u}{\partial\theta}\right] - \frac{2}{3}\frac{\partial\eta}{r\partial\theta}\left[\vec{\nabla}\cdot\vec{V}\right]$$

$$+ 2\frac{\partial\eta}{\partial r}\frac{\partial w}{\partial r} + \frac{2}{r^2}\frac{\partial\eta}{\partial\theta}\frac{\partial w}{\partial\theta}$$

$$- \frac{\partial\eta}{r\partial r}\left[\frac{\partial}{\partial r}(rw) - \frac{\partial u}{\partial\theta}\right]$$

The inclusion of the strain rate tensor in the energy equation adds many more terms to Equation 25. In Appendix A, it is shown that

the energy equation for the plastic zone is

$$\frac{\partial(\rho E)}{\partial t} = -\frac{\partial(r^2 \rho u E)}{r^2 \partial r} - \frac{\partial(\rho w E \sin\theta)}{r \sin\theta \partial\theta} - \frac{\partial(r^2 p u)}{r^2 \partial r}$$

$$- \frac{\partial(p w \sin\theta)}{r \sin\theta \partial\theta} + \left[\vec{\nabla}\cdot\vec{V}\right]^2$$

$$+ \frac{1}{2}\left(\frac{1}{r}\frac{\partial u}{\partial\theta} + \frac{\partial w}{\partial r} - \frac{w}{r}\right)\left[\vec{\nabla}\cdot\vec{V}\right]$$

$$+ u\left\{\frac{1}{3}\eta\frac{\partial}{\partial r}\left[\vec{\nabla}\cdot\vec{V}\right] + \eta\left[\frac{1}{r^2}\frac{\partial}{\partial r}\left(r^2\frac{\partial u}{\partial r}\right)\right.\right.$$

(29)

$$\left.\left. + \frac{\partial\left(\frac{\partial u}{\partial\theta}\sin\theta\right)}{r^2\sin\theta\,\partial\theta} - \frac{2u}{r^2} - \frac{2\frac{\partial}{\partial\theta}(w\sin\theta)}{r^2\sin\theta}\right]\right.$$

$$- \frac{2}{3}\frac{\partial\eta}{\partial r}\left[\vec{\nabla}\cdot\vec{V}\right] + 2\frac{\partial\eta}{\partial r}\frac{\partial u}{\partial r} + \frac{2}{r^2}\frac{\partial\eta}{\partial\theta}\frac{\partial u}{\partial\theta}$$

$$\left. + \frac{1}{r^2}\frac{\partial\eta}{\partial\theta}\left[\frac{\partial}{\partial r}(rw) - \frac{\partial u}{\partial\theta}\right]\right\} + w\left\{\frac{\eta}{3r}\frac{\partial}{\partial\theta}\left[\vec{\nabla}\cdot\vec{V}\right]\right.$$

$$+ \eta\left[\frac{\frac{\partial}{\partial r}\left(r^2\frac{\partial w}{\partial r}\right)}{r^2} + \frac{\frac{\partial}{\partial\theta}\left(\frac{\partial w}{\partial\theta}\sin\theta\right)}{r^2\sin\theta} - \frac{w}{r^2\sin^2\theta}\right.$$

$$\left. + \frac{2}{r^2}\frac{\partial u}{\partial\theta}\right] - \frac{2}{3r}\frac{\partial\eta}{\partial\theta}\left[\vec{\nabla}\cdot\vec{V}\right] + 2\frac{\partial\eta}{\partial r}\frac{\partial w}{\partial r}$$

$$\left. + 2\frac{\partial\eta}{\partial\theta}\frac{\partial w}{\partial\theta} - \frac{1}{r}\frac{\partial\eta}{\partial r}\left[\frac{\partial}{\partial r}(rw) - \frac{\partial u}{\partial\theta}\right]\right\}$$

Equations for the Elastic Region

In the plastic region, there is viscous flow of the material which results in a permanent distortion of the grain structure of the metal. As the peak pressure in the shock front continues to decrease with propagation away from the position of impact of a small body on a very large target, the pressure is not sufficiently large to produce a permanent distortion of the grain structure of the target. The material of the target in this undistorted region remains in the elastic state. The equations for the propagation of the shock through this region are the familiar equations for an elastic region.

The stress tensor was given in Equation 7; it is

$$S_{ij} = \lambda e_{ij} \delta_{ij} + 2\mu e_{ij}$$

where μ is the modulus of rigidity, and λ is Lame's lambda. The components of the strain tensor, e_{ij}, are defined in Equation 8. The divergence of the stress tensor must be added to the equation of motion, and the rotation for the divergence is (26)

$$(30) \quad \nabla \cdot S_{ij} = (\lambda + \mu) \vec{\nabla}(\vec{\nabla} \cdot \vec{r}) + \mu \nabla^2(\vec{r})$$

The radial component of this vector must be added to the radial component of motion, Equation 21, and the tangential component, θ, must be added to Equation 23. In Appendix B, it is shown that the radial equation of motion is

$$\frac{\partial(\rho u)}{\partial t} = -\frac{1}{r^2}\frac{\partial}{\partial r}(r^2\rho u^2) - \frac{\frac{\partial}{\partial\theta}(\rho uw\sin\theta)}{r\sin\theta} + \frac{\rho w^2}{r} - \frac{\partial p}{\partial r}$$

$$+ (\lambda+\mu)\frac{\partial}{\partial r}\left[\frac{1}{r^2}\frac{\partial}{\partial r}(r^2 v_r) + \frac{\frac{\partial}{\partial\theta}(v_\theta\sin\theta)}{r\sin\theta}\right]$$

(31)
$$+\mu\left[\frac{1}{r^2}\frac{\partial}{\partial r}\left(r^2\frac{\partial v_r}{\partial r}\right) + \frac{\frac{\partial}{\partial\theta}\left(\frac{\partial v_\theta}{\partial\theta}\sin\theta\right)}{r^2\sin\theta}\right.$$

$$\left. - \frac{2v_r}{r^2} - \frac{\frac{\partial}{\partial\theta}(v_\theta\sin\theta)}{r^2\sin\theta}\right]$$

The angular, or tangential equation of motion is

$$\frac{\partial(\rho w)}{\partial t} = -\frac{1}{r^2}\frac{\partial}{\partial r}(r^2\rho uw) - \frac{\frac{\partial}{\partial\theta}(\rho w^2\sin\theta)}{r\sin\theta} - \frac{\rho wu}{r} - \frac{1}{r}\frac{\partial p}{\partial\theta}$$

$$+ (\lambda+\mu)\frac{\partial}{r\partial\theta}\left[\frac{1}{r^2}\frac{\partial}{\partial r}(r^2 v_r) + \frac{\frac{\partial}{\partial\theta}(v_\theta\sin\theta)}{r\sin\theta}\right]$$

(32)
$$+\mu\left[\frac{1}{r^2}\frac{\partial}{\partial r}\left(r^2\frac{\partial v_\theta}{\partial r}\right) + \frac{\frac{\partial}{\partial\theta}\left(\frac{\partial v_\theta}{\partial\theta}\sin\theta\right)}{r^2\sin\theta}\right.$$

$$\left. - \frac{v_\theta}{r^2\sin^2\theta} + \frac{2}{r^2}\frac{\partial v_r}{\partial\theta}\right]$$

The energy equation is also derived in Appendix B.

$$\frac{\partial(\rho E)}{\partial t} = -\frac{1}{r^2}\frac{\partial}{\partial r}(r^2 \rho u E) - \frac{\frac{\partial}{\partial \theta}(\rho w E \sin\theta)}{r \sin\theta} - \frac{1}{r^2}\frac{\partial(r^2 \rho u)}{\partial r}$$

$$- \frac{\frac{\partial}{\partial \theta}(\rho w \sin\theta)}{r \sin\theta} + 2\left\{(\lambda+\mu)\frac{\partial}{\partial r}\left[\frac{1}{r^2}\frac{\partial}{\partial r}(r^2 v_r)\right.\right.$$

$$\left. + \frac{\frac{\partial}{\partial \theta}(v_\theta \sin\theta)}{r \sin\theta}\right] + \mu\left[\frac{1}{r^2}\frac{\partial}{\partial r}\left(r^2 \frac{\partial v_r}{\partial r}\right)\right.$$

$$\left.\left. + \frac{\frac{\partial}{\partial \theta}\left(\frac{\partial v_\theta}{\partial \theta}\sin\theta\right)}{r^2 \sin\theta} - \frac{2 v_r}{r} - \frac{2\frac{\partial}{\partial \theta}(v_\theta \sin\theta)}{r^2 \sin\theta}\right]\right\} \qquad (33)$$

$$+ \omega\left\{(\lambda+\mu)\frac{\partial}{r\partial\theta}\left[\frac{1}{r^2}\frac{\partial}{\partial r}(r^2 v_r) + \frac{\frac{\partial}{\partial \theta}(v_\theta \sin\theta)}{r \sin\theta}\right]\right.$$

$$+ \mu\left[\frac{1}{r^2}\frac{\partial}{\partial r}\left(r^2 \frac{\partial v_\theta}{\partial r}\right) + \frac{\frac{\partial}{\partial \theta}\left(\frac{\partial v_\theta}{\partial \theta}\sin\theta\right)}{r^2 \sin\theta} - \frac{v_\theta}{r^2 \sin^2\theta}\right.$$

$$\left.\left. + \frac{2}{r^2}\frac{\partial v_r}{\partial \theta}\right]\right\} + \left[\vec{\nabla}\cdot\vec{V}\right]\left[\frac{\partial v_r}{\partial r} + \frac{1}{r}\frac{\partial v_\theta}{\partial \theta} + \frac{2 v_r}{r}\right.$$

$$\left. + \frac{v_\theta}{r}\cot\theta + \frac{1}{2}\left(\frac{\partial v_\theta}{\partial r} - \frac{v_\theta}{r} + \frac{1}{r}\frac{\partial v_r}{\partial \theta}\right)\right]$$

Equations of State

This thesis is directed to obtain a solution for the impact of a sphere of porous rock onto a solid, thick slab of aluminum. To obtain this solution, four equations and a condition must be employed for each condition of matter. Three of the four equations are for the conservation of mass, momentum and energy. In the sections that immediately precede this section, these equations were obtained in spherical coordiantes for each of the three media; inviscid fluid, plastic and elastic materials. The fourth equation for the solution is an equation of state for each medium. The condition, mentioned above, is that the entropy content of the material must be increased by the passage of the shock front.

Four equations of state are required to obtain the desired solution. These equations of state are:

1. an equation for fluid aluminum
2. an equation for plastic aluminum
3. an equation for elastic aluminum
4. an equation for porous stone

Equations of state are presented for each of these four cases in the following discussion.

Equation of State for the Fluid Region of Aluminum

An equation of state from the work of Tillotson is used for the inviscid fluid range (35). The equation has the form

$$(34)\quad P = \left(a + \frac{b}{\frac{E}{E_0\eta^2} + 1}\right)\rho E + A\mu + B\mu^2$$

P is the pressure in megabars; E is the specific internal energy; ρ is the specific density; η is the ratio ρ/ρ_o, where ρ_o is the normal density, and $\mu=(\eta-1)$. The letters E_o, A, B, a and b represent constants. Their values for aluminum are:

$$a = 0.5$$

$$b = 1.63$$

$$A = 0.752 \text{ mb}$$

$$B = 0.650 \text{ mb}$$

$$E_o = 0.05 \text{ mb } \text{cm}^3/\text{gm}.$$

Equation of State for the Elastic Region of Aluminum

An equation of state was suggested by Lundergan for elastic aluminum (23). It has the form

$$P = 1044\left(1 - \frac{\rho_o}{\rho}\right) \tag{35}$$

Equation of State for Plastic Region of Aluminum

For the plastic range of aluminum, Lundergan (23) suggests the equation of state:

$$P = 744\left(1 - \frac{\rho_o}{\rho}\right) + 1.6 \tag{36}$$

Equation 36 does not agree well with Tillotson's equation in the fluid-plastic transition zone (see Figure 1). Since the equation is an empirical fit for experimental data below 31 kb, it should not be expected to be accurate in the vicinity of the fluid-plastic transition.

Lundergan suggests that for pressures greater than 31 kb, the plastic equation have the form

$$(37) \quad P = (\lambda + \tfrac{2}{3}\mu)\left[1 + b\left(1 - \frac{\rho_0}{\rho}\right)\right]\left(1 - \frac{\rho_0}{\rho}\right)$$

In this thesis, the equation of state for the plastic zone was chosen to have the form

$$(38) \quad P = C_1 + C_2\left(1 - \frac{\rho_0}{\rho}\right) + C_3\left(1 - \frac{\rho_0}{\rho}\right)^2$$

Lundergan (23) uses the equation of state proposed by Walsh, et al. (39) which is

$$P = 765\left(1 - \frac{\rho_0}{\rho}\right) + 1659\left(1 - \frac{\rho_0}{\rho}\right)^2 + 428\left(1 - \frac{\rho_0}{\rho}\right)^3$$

to predict that the high pressure at which the dual shock wave, plastic region begins. This equation predicts a pressure of 113 kb. When Tillotson's equation of state is used, the dual shock wave initiates at approximately 138 kb.

A numerical curve fitting technique was used on the IBM 7040 computer at Oklahoma State University to fit Equation 38 with Tillotson's equation at 138 kb. The constants in equation 38 were found to have the values

$$C_1 = 1.6 \text{ kb}$$

$$C_2 = 845.5 \text{ kb}$$

$$C_3 = 2145.7 \text{ kb}.$$

The resulting form of Equation 38 is plotted in Figure 1.

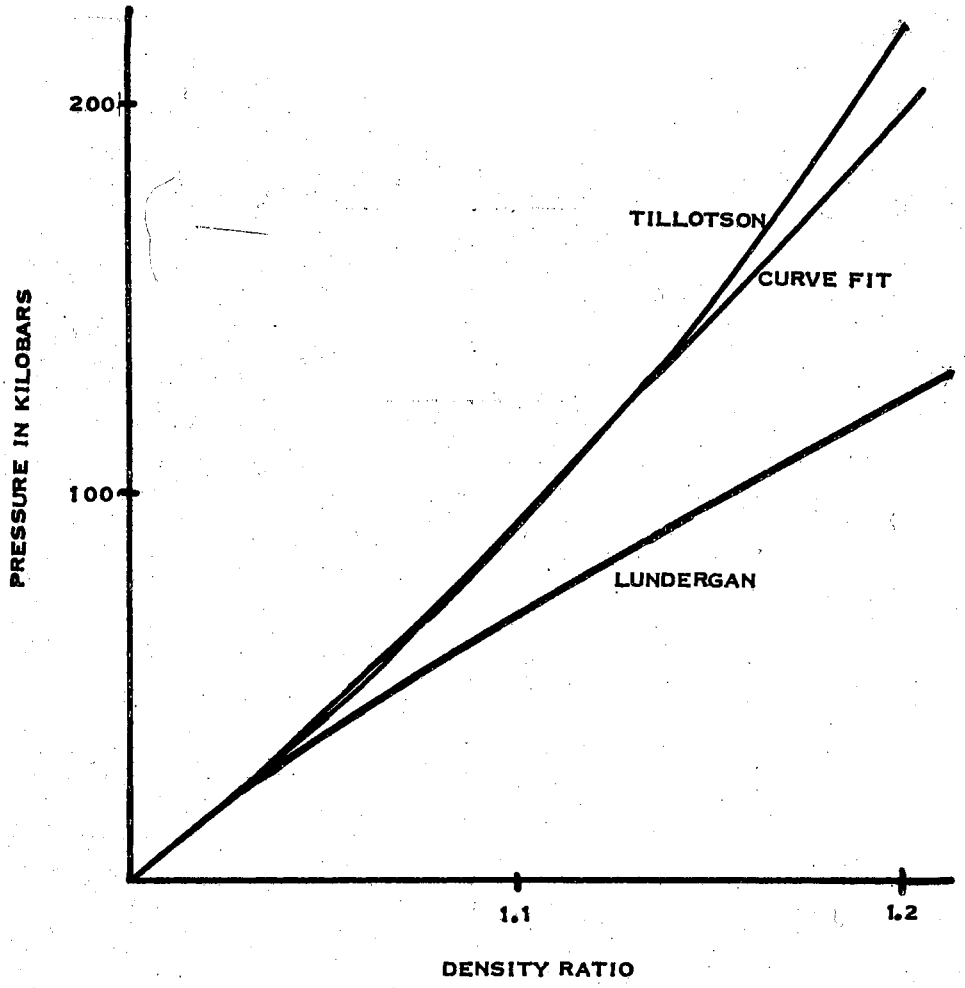

FIGURE 1 – PLASTIC EQUATIONS OF STATE

Lundergan states that the constant b in equation 37 should be approximately 2.5. The ratio of the constants in Equation 38 is

$$\frac{C_3}{C_2} = 2.54$$

From these considerations, Equation 38

1. fits Tillotson's equation at 138 kb
2. fits the elastic yield point at 6.4 kb
3. gives the approximate values of the constants: $\left(\lambda + \frac{2}{3}\mu\right)$ and b .

It should be noted that Bell also proposes that the equation of state for the plastic zone of aluminum should be parabolic (4).

Equation of State for Porous Stone

A somewhat complicated equation of state is employed to describe the pressures created in the impacting, porous micrometeoroid. Since the internal pressures in the micrometeoroid will be quite high and fluid flow behavior may be assumed, it appears that Tillotson's form of the equation of state would be appropriate. However, the following table, compiled by Wagner, et al., shows that the Hugoniot points of a porous body predicted by the Tillotson equation are not sufficiently close to the experimental points to warrant its use without modification (38).

Several Soviet papers have proposed an equation of state for porous materials which fits experimental data quite well (1), (2), (16), (17). McClosky (25) has modified and extended the Russian work, and Wagner, et al., (38), have corrected McClosky's work.

TABLE I

COMPARISON OF RUSSIAN EXPERIMENTAL DATA WITH TILLOTSON'S EQUATION OF STATE

Porosity	Compression	Pressure (Mb) Experimental	Tillotson
	Aluminum		
1.00	2.185	4.93	4.813
1.43	1.498	1.391	1.404
2.08	1.176	1.003	0.790
2.98	1.015	0.702	0.559
	Copper		
1.00	1.960	9.55	10.321
1.57	1.395	2.626	3.457
1.57	1.595	7.01	9.309
2.00	1.219	2.204	2.975
2.00	1.402	5.95	8.231
3.01	1.045	1.582	2.595
4.00	0.927	1.260	2.228
4.00	1.018	3.54	5.676
	Nickel		
1.00	1.946	9.56	8.811
1.43	1.364	2.908	2.678
1.75	1.261	2.469	2.372
1.75	1.295	6.87	4.517
3.00	0.941	1.639	1.251
3.00	0.949	4.67	2.845

The proposed equation of state assumes that the pressure, P, and the internal energy, E, can be written as the sum of three components.

$$(39) \quad P(\eta,T) = P_c(\eta) + P_n(\eta,T) + P_e(\eta,T)$$

$$(40) \quad E(\eta,T) = E_c(\eta) + E_n(\eta,T) + E_e(\eta,T)$$

In these equations, T is the temperature, η is the compression ratio ρ/ρ_0, where ρ is the density, and ρ_0 is the density at normal conditions. The subscripts have the following meanings: c indicates the cold compression; i.e., the effect of atomic lattice interactions at $0^{\circ}K$; n indicates the contribution due to thermal vibrations of lattice ions; and e represents the contribution of the thermal excitation of electrons.

At $0^{\circ}K$, only the electrons contribute to the pressure. The ions contribute only through their kinetic energy, and at $0^{\circ}K$ their kinetic energy may be assumed to be zero. The contribution of the electrons arises from their resistance to compressive forces, since compression raises the quantum states.

There is no unique way of representing repulsive force potentials. An early estimate was that the repulsive potential had the following form

$$(41) \quad E = -A\left[\frac{r_0}{r} - \frac{1}{n}\left(\frac{r_0}{r}\right)^n\right]$$

where E is the interaction energy of the crystal, and r_o is the interatomic distance when pressure and temperature are zero. Different authors use different values for n, but generally

$$7.84 \leq n \leq 9.1$$

The Russians found that repulsive forces could not be fitted by a power series because n must be changed as r changes. No single value of n will give the complete solution for a wide range of pressures. A more versatile equation is

$$(42) \qquad E = -A\left[\frac{n_0}{n} - \frac{\rho}{n_0}\exp\left\{\frac{1}{\rho}(n_0 - n)\right\}\right]$$

This form gives good agreement with experimental data when the constants are properly adjusted. The pressure is given by

$$(43) \qquad P = -\frac{\partial E}{\partial V}$$

Since $V = r^3$, then the "cold" pressure component is

$$(44) \qquad P_c(\eta) = A_1\left\{\eta^{2/3}\exp\left[b_1(1-\eta^{-1/3})\right] - \eta^{4/3}\right\}$$

The first term in Equation 44 represents the force from the repulsive potential of ions, and the second term represents the attractive potential of the ions. McClosky (25) describes the employment of certain physical constants to evaluate the constants A_1 and b_1.

The internal energy from this "cold" compression is represented by the following relation

$$(45) \qquad E_c = -\int P_c \, dV$$

Since $V = 1/\rho$ and $\eta = \frac{\rho}{\rho_0}$, change Equation 45 to an integration over η

$$(46) \qquad E_c = \frac{1}{\rho_0} \int_1^{\eta} P_c \frac{d\eta}{\eta^2}$$

or

$$(47) \quad E_c(\eta) = \frac{3A}{\rho_0}\left[\frac{1}{f_1} \exp\left[f_1(1-\eta^{-\frac{1}{3}})\right] - \eta^{1/3} - \frac{1}{f_1} + 1\right]$$

Equations 44 and 47 are valid only for $\eta \leq 2.5$. For higher compressions, the equations must agree with Thomas-Fermi statistics. McClosky makes the transition from Equation 44 to Thomas-Fermi statistics by writing

$$(48) \quad P_c(\eta) = P_c(\eta_b) + \left.\frac{dP_c}{d\eta}\right|_{\eta=\eta_b} (\eta - \eta_b) + A_2 (\eta - \eta_b)^2$$

The first term on the right is Equation 44, which is evaluated at $\eta = \eta_b$.

The constant A_2 may be evaluated by referring to Thomas-Fermi data to find a pressure $P_c(\eta_{TFC})$ at a high value for the compression ratio, η_{TFC}. The relation for A_2 becomes:

$$(49) \quad A_2 = \frac{1}{(\eta_{TFC} - \eta_b)^2}\left[P_c(\eta_{TFC}) - P_c(\eta_b)\right] - \frac{1}{(\eta_{TFC} - \eta_b)} \left.\frac{\partial P_c}{\partial \eta}\right|_{\eta=\eta_b}$$

For the nuclear component, the Debye theory must be valid at low temperatures. This requires that these relations hold:

$$(50) \quad E_N(\eta, T) = 9RT\left(\frac{T}{\Theta}\right)^3 \int_0^{\Theta/T} \frac{x^3\,dx}{e^x - 1}$$

and

$$(51) \quad P_N(\eta, T) = \gamma \rho E_N$$

where γ is the Gruneisen ratio.

At high temperatures, the thermal motion of the nuclei is properly described by the equation for a perfect gas. To describe the transition from the solid phase to the gas phase, the Soviets have proposed the following:

$$(52) \quad E_N(\eta, T) = \frac{3}{2}\,\frac{2+z}{1+z}\,RT$$

$$(53) \quad P_N(\eta, T) = \eta \rho_0\,\frac{3\gamma + z}{1+z}\,RT$$

where

$$(54) \quad z = \frac{\rho_0 RTA}{K\left(\frac{dP_c}{d\eta}\right)}$$

The atomic weight is A, and K is an empirical constant. These equations give the proper limiting forms because when T is small

$$E_N \sim 3RT$$
$$P_N \sim \eta \rho_0 \gamma E_N$$

Debye Theory

and when T is large

$$E_N \sim \frac{3}{2} RT$$
$$P_N \sim \eta \rho_0 RT$$

Perfect Gas.

The electronic thermal contribution at low temperature is given by Gilvarry (14)

$$(55) \quad E_e(\eta, T) = \frac{1}{2} \beta(\eta) T^2$$

$$(56) \quad P_e(\eta, T) = \frac{1}{2} \eta \rho_0 g(\eta) \beta(\eta) T^2$$

where β is the coefficient of electronic specific heat, and g is the electronic Grueisen's ratio; i.e., $g = P_e/(E_e/V)$

Latter's work shows that at high temperatures, the pressure and internal energy approach asymtotic values which are closely approximated by

$$(57) \quad E_e = \frac{3}{2} n T$$

$$(58) \quad P_e = \eta \rho_0 n T$$

where

$$(59) \quad n = \frac{0.85 X^{0.59}}{1 + 0.85 X^{0.59}} ZR$$

and

$$(60) \qquad X = \frac{T}{1.16 \times 10^4 Z^{4/3}}$$

The atomic number is Z (21). To interpolate between the low and the high temperature range, the Russians propose

$$(61) \qquad E_e(\eta, T) = \frac{9\mathcal{R}^2}{4\beta} \log\left[\cosh\left(\frac{2\beta T}{3\mathcal{R}}\right)\right]$$

$$(62) \qquad P_e(\eta, T) = \eta \rho_0 \frac{\mathcal{R}^2}{g\beta} \log\left[\cosh\left(\frac{g\beta T}{\mathcal{R}}\right)\right]$$

These equations give the proper limiting forms. For low temperatures, Equations 61 and 62 reduce to

$$E_e = \tfrac{1}{2}\beta T^2$$

$$P_e = \tfrac{1}{2}\eta \rho_0 g \beta T^2$$

and for high temperatures, they become

$$E_e = \tfrac{3}{2}\mathcal{R} T$$

$$P_e = \eta \rho_0 \mathcal{R} T$$

A valid criticism of Equations 61 and 62 has been presented by Wagner, et al., (38). Any thermodynamic equation must satisfy the equation of "thermodyanmic consistency"

$$(63) \qquad \left(\frac{\partial E}{\partial V}\right)_T = T^2 \frac{\partial}{\partial T}\left(\frac{P}{T}\right)$$

which is perhaps better known as the Maxwell equation

$$(64)\quad \left(\frac{\partial S}{\partial V}\right)_T = \left(\frac{\partial P}{\partial T}\right)_V$$

Equations 61 and 62 do not obey this relation. In these equations, E is internal energy, S is entropy, T is temperature, P is pressure, and V is volume. In retrospect, it should be mentioned that the interpolation equations for the nuclear contribution, equations 52 and 53, and the equations for the cold compenent, Equations 44 and 45, do obey the law of "thermodynamic consistence.

Since the electronic contribution is large at high pressures, this inaccuracy may cause significant errors. The alternative suggested by Wagner, et al., is to numerically interpolate Latter's high temperature data in tabular form.

Equations 44 to 62 were incorporated into a computer code, and tables of P (η,T) and E(η,T) were calculated. From these tables, a third pressure table was constructed with P having the coordinates ρ and E. This table was read in as input data to the impact problem. Selected pressure isotherms for a porous silicate rock are shown in Figures 2 and 3.

The dynamical equations are employed to calculate the density, ρ, and the internal energy, E. These two variables determine the coordinates of the pressure elements in the table, and the appropriate value of pressure is found by numerical interpolation.

Viscosity Models

The viscosity of a material is a function of the thermodynamic

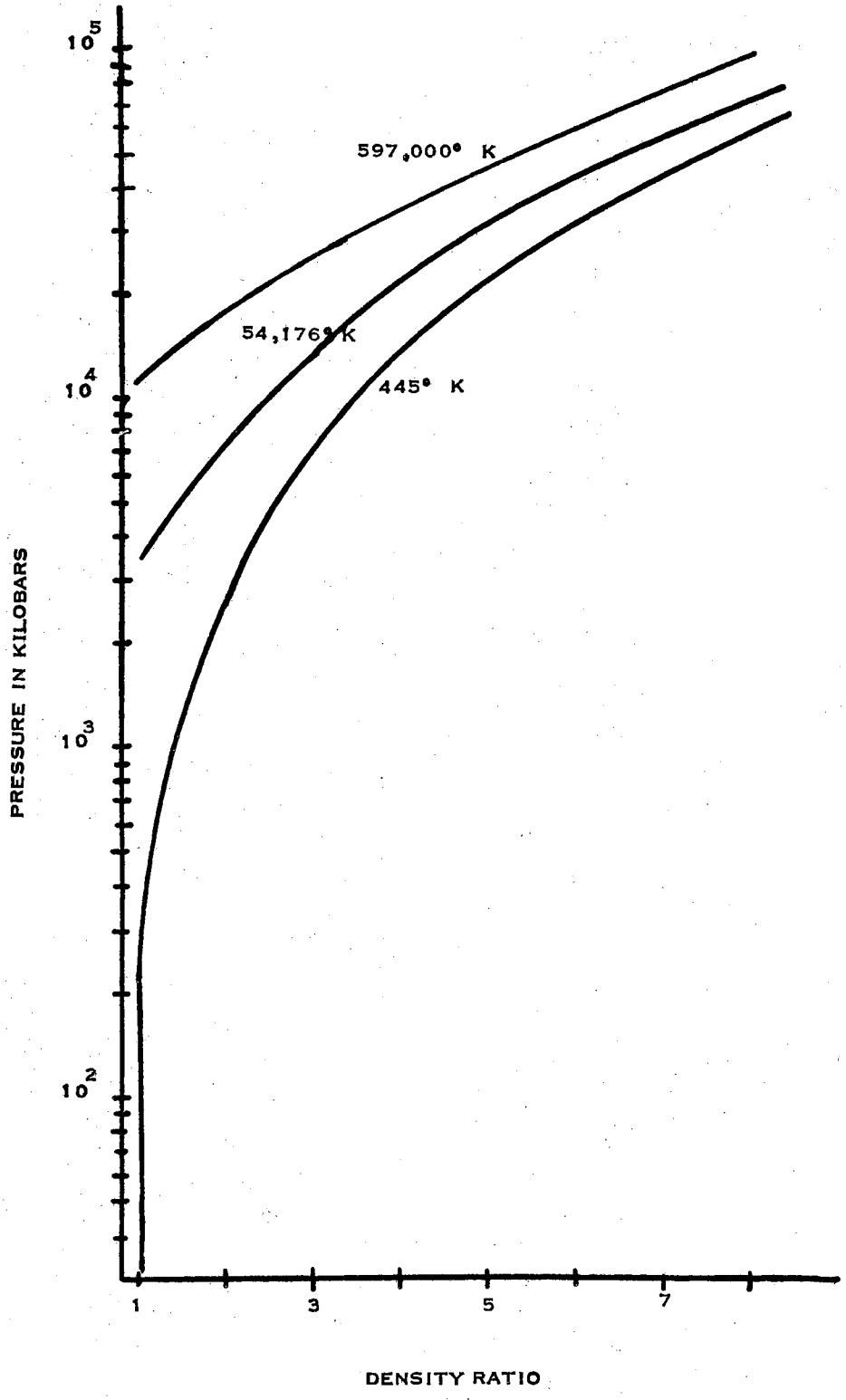

FIGURE 2 – PRESSURE ISOTHERMS FOR ROCK OF POROSITY 1

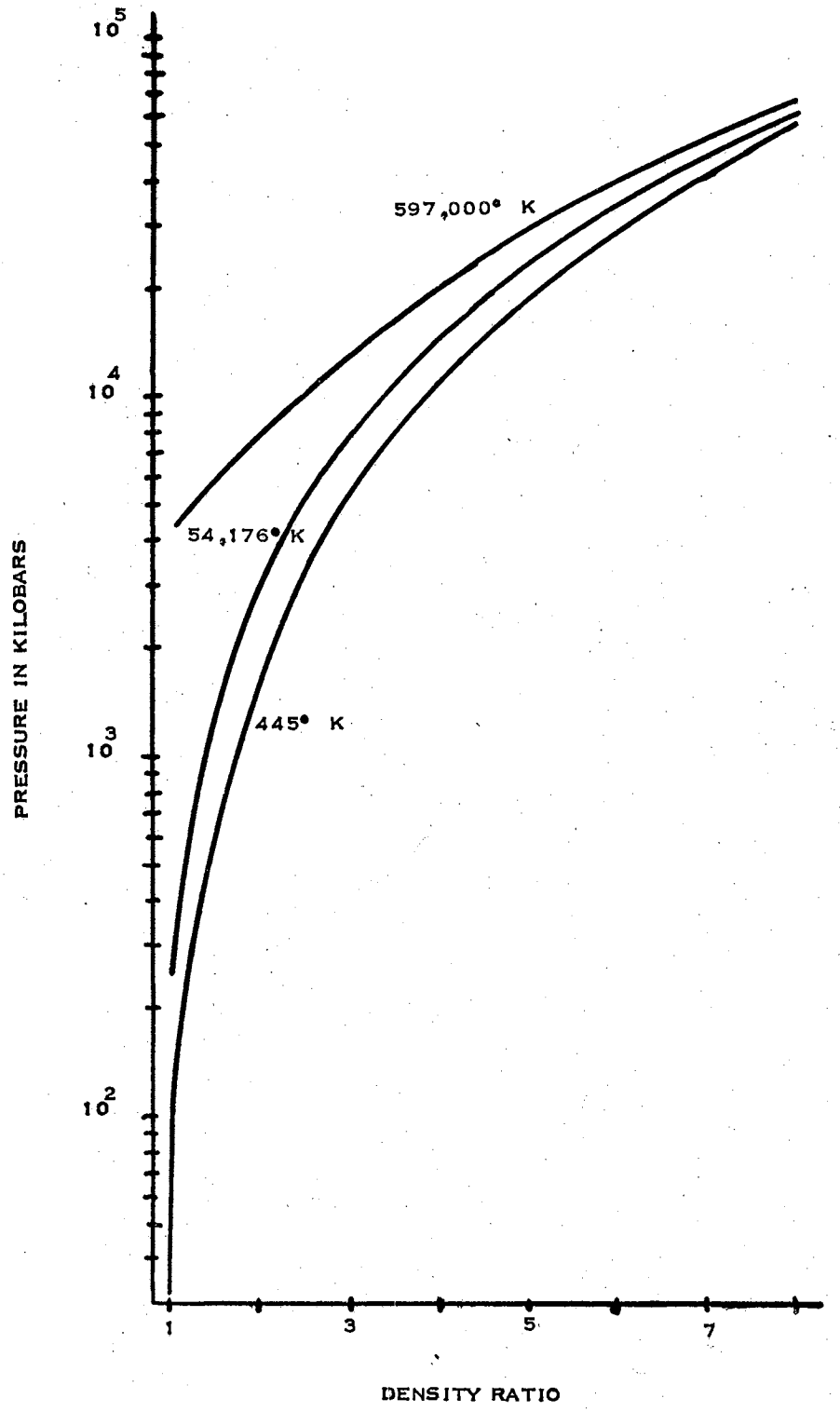

FIGURE 3 – PRESSURE ISOTHERMS FOR ROCK OF POROSITY 4

state of the material. For a homogeneous medium, the viscosity is a function of two thermodynamic properties. The usual choice for these variables are:

$$\eta = \eta(p, T) \quad \text{OR} \quad \eta = \eta(\rho, T)$$

Some general facts about the viscosity are:

1. The viscosity of a solid increases if the temperature increases and also increases if the pressure increases.
2. The viscosity of a liquid increases if the pressure increases but decreases if the temperature increases.
3. The viscosity of a gas increases if the temperature increases and also if the pressure increases.

Non-Newtonian flow can be explained in terms of a single viscosity coefficient if this coefficient is considered to be a function of the local rate of strain. For a liquid,

$$\eta = F(S)$$

where S is the strain rate tensor, and F is a positive, even function (13). In general notation

$$(65) \quad S = \frac{1}{2}\left(S_{11}^2 + S_{22}^2 + S_{33}^2\right) + S_{12}^2 + S_{13}^2 + S_{23}^2$$

where

$$(66) \quad S_{ij} = \frac{1}{2}\left(\frac{\partial v_i}{\partial x_j} + \frac{\partial v_j}{\partial x_i}\right)$$

For a plastic solid, the viscosity is a decreasing function of the strain rate tensor. Eirich (13) proposes the following model for the viscosity of a plastic solid

$$(67) \qquad \eta = \eta_0 + \frac{S_0}{|S|}$$

This model is used by Riney (31) to describe the plastic flow which occurs during a hypervelocity impact, and it is the model that is employed in this thesis. In the literature, plastic flow described by this model is called Bingham plastic flow. The terms in Equation 67 have the following meanings:

η_0 is the simple viscosity effect

S_0 is the yield value in shear

$|S|$ is the value of the strain rate tensor as defined in Equation 65.

S_0 and η_0 are not constants but are functions of pressure and temperature. For a plastic solid

$$\frac{\partial \eta_0}{\partial p} > 0 \qquad \text{and} \qquad \frac{\partial S_0}{\partial p} > 0$$

but

$$\frac{\partial \eta_0}{\partial T} < 0 \qquad \text{and} \qquad \frac{\partial S_0}{\partial T} < 0$$

The equations that describe the pressure and temperature dependence of η_0 and S_0 in this thesis are

$$\eta_0 = a_1 + a_2 p + a_3/E$$

$$S_0 = b_1 + b_2 p + b_3/E$$

E is the internal energy, which is a measure of the temperature. As a consequence, the conditions $\frac{\partial \eta_0}{\partial T} < 0$ and $\frac{\partial S_0}{\partial T} < 0$ are satisfied. The

constants a_1, a_2, a_3, b_1, b_2, and b_3 were picked by trial and error so that nominal values for η_0 and S_0 result at standard temperature and pressure.

If a pressure, or an energy gradient exist, then there will be a viscosity gradient since

$$\vec{\nabla}\eta = \frac{\partial \eta}{\partial p}\vec{\nabla}p + \frac{\partial \eta}{\partial E}\vec{\nabla}E$$

CHAPTER III

FINITE DIFFERENCE METHODS

Finite Difference Mesh

For the solution of the impact problem, the differential equations are converted to finite difference equations. In seeking the solution, the finite difference equations were applied to each cell, in turn, in a regularly arranged network, or mesh, of cells. Before discussing the conversion of the dynamic flow equations to finite difference equations, it is desirable to describe the arrangement of the mesh of cells. The selection of the coordinate system for the mesh of cells is made after the problem is fully defined. The problem is stated in the next paragraph.

At time t = 0, it is assumed that the spherical micrometeoroid has just touched the aluminum target. The target is assumed to be semi-infinite and to be at rest. The micrometeoroid has a velocity V normal to the target, and the point of impact determines the axis of symmetry. The physical situation is depicted in Figure 4. The line OZ represents the axis of symmetry for the fluid flow and shock wave behavior. The point P is the point of contact between the sphere and the aluminum.

The basic problem in obtaining a numerical solution is the conversion of the physical situation into a mathematical model that allows finite difference techniques to be employed to represent the physical

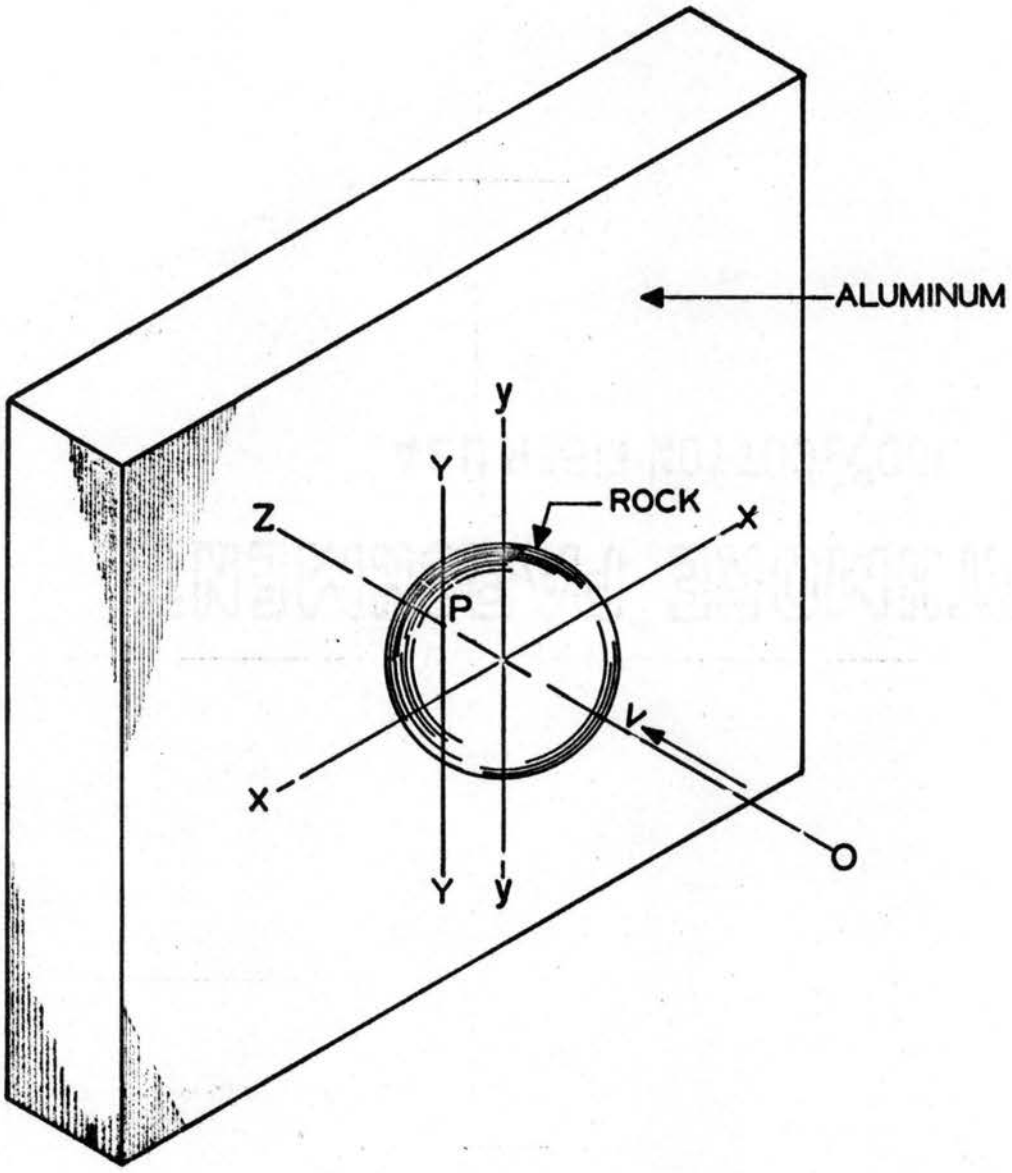

FIGURE 4 – IMPACT OF STONE SPHERE ON ALUMINUM TARGET

system. The problem is made to appear to be reduced to a two dimensional problem by considering only the plane determined by the lines OZ and YPY. Because of symmetry, the solution plane is further restricted by using only the half plane lying above the line OZ.

In order to apply finite difference techniques to the dynamical equations that describe the impact, the solution space must be covered by a grid of finite difference cells. This grid is constructed by placing the origin at point 0 and drawing lines of constant angle and lines of constant radius. The resulting picture of the impact is shown in Figure 5. The center of each cell in the mesh is given two coordinates (L,M). L represents the radial coordinate, and M the angular coordinate. The directions of increasing L and M are shown. Up to this position in this section, it has not been clearly emphasized that the cells in the mesh are of different thicknesses. The thickness may be explained by reference to the mesh in Figure 5. A typical radial line from the origin makes an angle, θ, with the line of symmetry, OZ. At any distance, r, from the origin along this typical radial line, the thickness of the cell is

$$r \sin\theta \, d\theta$$

After finding the solution in the single layer of cells that are shown in the figure, the complete solution is found by rotating the wedge shaped solution about the axis of symmetry, OZ. Since the thickness of the wedge is zero at the OZ-axis, there is no flow across the axis.

Equations of Dynamics in Finite Difference Form

The completed computer program for a long and complicated problem

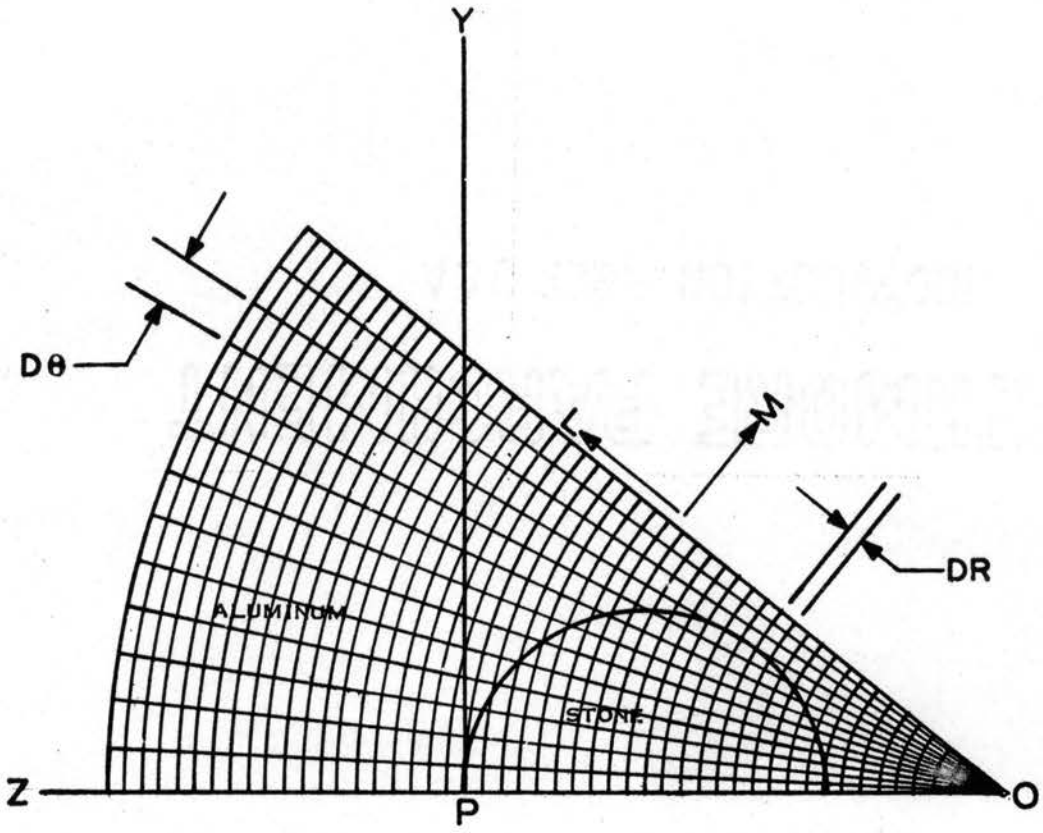

FIGURE 5 – FINITE DIFFERENCE MESH

shows many characteristics which are typical of the individual who wrote the program. There are, nevertheless, many basic techniques which are common to all good computer programs. The mixture of the basic technique and the individual characteristics for formulating the difference equations for a computer program are, in part, presented in this section as well as the conversion of the differential equations for dynamics into difference equations.

Consider a function, f, which depends on a space dimension, x, and the time, t. Express this function in the usual functional notation.

$$f = f(x,t) \tag{1}$$

The partial derivative of this function with respect to x may be approximated in finite difference form by either one of three expressions.

$$\frac{\partial f}{\partial x} = \frac{f(x,t) - f(x-\Delta x, t)}{\Delta x} \tag{2}$$

or

$$\frac{\partial f}{\partial x} = \frac{f(x+\frac{1}{2}\Delta x,t) - f(x-\frac{1}{2}\Delta x,t)}{\Delta x} \tag{3}$$

or

$$\frac{\partial f}{\partial x} = \frac{f(x+\Delta x,t) - f(x,t)}{\Delta x} \tag{4}$$

These representations, 2, 3, and 4, are called backward difference, central difference, and forward difference; respectively. The smaller the value of Δx, the better will be the approximation. Similarly, the partial derivative of f with respect to time may be approximated by either of the following expressions.

$$\frac{\partial f}{\partial t} = \frac{f(x,t) - f(x, t-\Delta t)}{\Delta t} \tag{5}$$

or

$$(6) \quad \frac{\partial f}{\partial t} = \frac{f(x, t+\frac{1}{2}\Delta t) - f(x, t-\frac{1}{2}\Delta t)}{\Delta t}$$

or

$$(7) \quad \frac{\partial f}{\partial t} = \frac{f(x, t+\Delta t) - f(x, t)}{\Delta t}$$

Again, Equation 5 is a backward difference, Equation 6 is a central difference, and Equation 7 is a forward difference. The accuracy of the approximation varies inversely with the magnitude of Δt.

In this thesis, all space derivatives are approximated by central differences, and all time derivatives are approximated by forward differences.

A typical cell in the two dimensional mesh for describing the problem is illustrated in Figure 6. The center of the cell has coordinates (R, θ) which may be calculated from the indices (L,M). Side 1 is determined by the ray, $\theta - \frac{1}{2}\Delta\theta$, and side 3 is represented by the ray, $\theta + \frac{1}{2}\Delta\theta$. Side 2 is determined by a circle of radius, $R + \frac{1}{2}\Delta R$; and side 4 is determined by a circle of radius, $R - \frac{1}{2}\Delta R$.

A shorthand notation will simplify further discussion in regard to the conversion of partial differential equations to finite difference equations. Let N represent the time, t; and (N+1) represent the time, $(t+\Delta t)$. Let L represent the radial distance, R; L - ½ the distance, $R - \frac{1}{2}\Delta R$; and L + ½ the distance, $R + \frac{1}{2}\Delta R$. Also let M represent the angle, θ; M - ½ the angle, $\theta - \frac{1}{2}\Delta\theta$; and M + ½ the angle, $\theta + \frac{1}{2}\Delta\theta$.

Consider the function,

$$f = f(r, \theta, t)$$

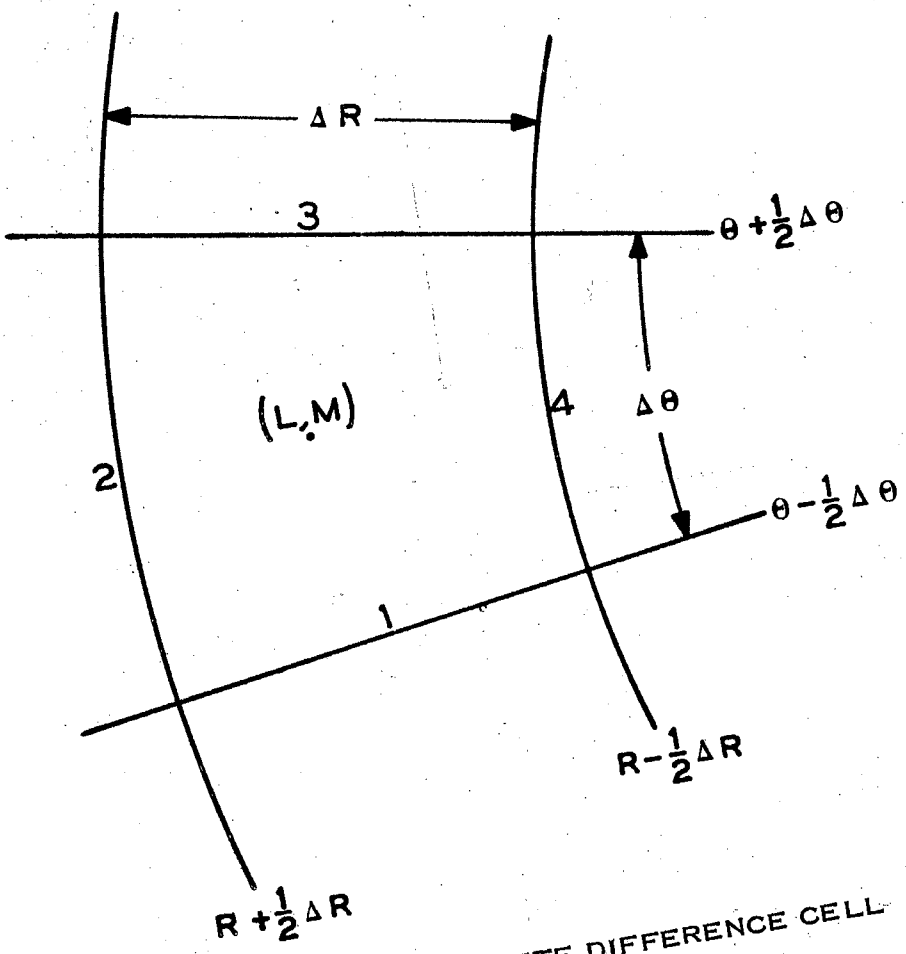

FIGURE 6 – FINITE DIFFERENCE CELL

then the following shorthand notation will be employed

$$(8) \qquad f^{N}_{L,M} \equiv f(r, \theta, t)$$

$$(9) \qquad f^{N+1}_{L,M} \equiv f(r, \theta, t+\Delta t)$$

$$(10) \qquad f^{N}_{L+1/2,M} \equiv f(r+\tfrac{1}{2}\Delta r, \theta, t)$$

$$(11) \qquad f^{N}_{L-\frac{1}{2},M} \equiv f(r-\tfrac{1}{2}\Delta r, \theta, t)$$

$$(12) \qquad f^{N}_{L,M+1/2} \equiv f(r, \theta+\tfrac{1}{2}\Delta\theta, t)$$

$$(13) \qquad f^{N}_{L,M-1/2} \equiv f(r, \theta-\tfrac{1}{2}\Delta\theta, t)$$

The partial derivatives of the function, f, at the center of cell (L,M) with respect to the space variables, r and θ, are

$$(14) \qquad \frac{\partial f}{\partial r} = \frac{f^{N}_{L+1/2,M} - f^{N}_{L-1/2,M}}{\Delta R}$$

and

$$(15) \qquad \frac{\partial f}{\partial \theta} = \frac{f^{N}_{L,M+1/2} - f^{N}_{L,M-1/2}}{\Delta \theta}$$

and the time derivative is

$$(16) \qquad \frac{\partial f}{\partial t} = \frac{f^{N+1}_{L,M} - f^{N}_{L,M}}{\Delta t}$$

The conservation of mass

$$(17)\quad \frac{\partial \rho}{\partial t} = -\frac{1}{r^2}\frac{\partial (r^2 \rho u)}{\partial r} - \frac{\frac{\partial}{\partial \theta}(\rho w \sin\theta)}{r \sin\theta}$$

may be represented in finite difference form

$$\frac{D_{L,M}^{N+1} - D_{L,M}^{N}}{\Delta t} = -\frac{(R^2 DU)^{N}_{L+1/2,M} - (R^2 DU)^{N}_{L-1/2,M}}{R^2 \Delta R}$$

$$(18)\qquad - \frac{(DW \sin\theta)^{N}_{L,M+1/2} - (DW \sin\theta)^{N}_{L,M-1/2}}{R \sin\theta\ \Delta\theta}$$

The other conservation equations for inviscid fluid flow which are:

$$(19)\quad \frac{\partial(\rho u)}{\partial t} = -\frac{1}{r^2}\frac{\partial}{\partial r}(r^2 \rho u^2) - \frac{\frac{\partial}{\partial \theta}(\rho w u \sin\theta)}{r \sin\theta} + \frac{\rho w^2}{r} - \frac{\partial p}{\partial r}$$

$$(20)\quad \frac{\partial(\rho w)}{\partial t} = -\frac{1}{r^2}\frac{\partial}{\partial r}(r^2 \rho u w) - \frac{\frac{\partial}{\partial \theta}(\rho w^2 \sin\theta)}{r \sin\theta} - \frac{\rho w u}{r} - \frac{1}{r}\frac{\partial p}{\partial \theta}$$

$$(21)\quad \frac{\partial(\rho E)}{\partial t} = -\frac{1}{r^2}\frac{\partial}{\partial r}(r^2 \rho u E) - \frac{\frac{\partial}{\partial \theta}(\rho w E \sin\theta)}{r \sin\theta} - \frac{1}{r^2}\frac{\partial}{\partial r}(r^2 p u)$$

$$- \frac{\frac{\partial}{\partial \theta}(p w \sin\theta)}{r \sin\theta}$$

may be transformed into the next three finite difference equations.

$$(22)\quad \frac{(DU)^{N+1}_{L,M} - (DU)^{N}_{L,M}}{\Delta t} = - \frac{(R^2 DU^2)^{N}_{L+1/2,M} - (R^2 DU^2)^{N}_{L-1/2,M}}{R^2 \Delta R}$$

$$- \frac{(DWU \sin\theta)^{N}_{L,M+1/2} - (DWU \sin\theta)^{N}_{L,M-1/2}}{R \sin\theta \, \Delta\theta} + \frac{(DW^2)^{N+1/2}_{L,M}}{R}$$

$$- \frac{P^{N}_{L+1/2,M} - P^{N}_{L-1/2,M}}{\Delta R}$$

$$(23)\quad \frac{(DW)^{N+1}_{L,M} - (DW)^{N}_{L,M}}{\Delta t} = - \frac{(R^2 DUW)^{N}_{L+1/2,M} - (R^2 DUW)^{N}_{L-1/2,M}}{R^2 \Delta R}$$

$$- \frac{(DW^2 \sin\theta)^{N}_{L,M+1/2} - (DW^2 \sin\theta)^{N}_{L,M-1/2}}{R \sin\theta \, \Delta\theta} - \frac{(DWU)^{N+1/2}_{L,M}}{R}$$

$$- \frac{P^{N}_{L,M+1/2} - P^{N}_{L,M-1/2}}{R \, \Delta\theta}$$

$$(24)\quad \frac{(DE)^{N+1}_{L,M} - (DE)^{N}_{L,M}}{\Delta t} = - \frac{(R^2 DUE)^{N}_{L+1/2,M} - (R^2 DUE)^{N}_{L-1/2,M}}{R^2 \Delta R}$$

$$- \frac{(DWE \sin\theta)^{N}_{L,M+1/2} - (DWE \sin\theta)^{N}_{L,M-1/2}}{R \sin\theta \, \Delta\theta}$$

$$- \frac{(R^2 PU)^{N}_{L+1/2,M} - (R^2 PU)^{N}_{L-1/2,M}}{R^2 \Delta R}$$

$$- \frac{(PW \sin\theta)^{N}_{L,M+1/2} - (PW \sin\theta)^{N}_{L,M-1/2}}{R \sin\theta \, \Delta\theta}$$

Equations 18, 22, 23, and 24 are made dimensionless by selecting

$$D = \rho/\rho_0$$
$$P = \phi/\phi_0$$
$$R = r/a$$
$$U = u/c_0$$
$$W = w/c_0$$
$$E = e/e_0$$
$$T = t/t_0$$
$$c_0^2 = \phi_0/\rho_0$$
$$e_0 = c_0^2$$
$$t_0 = a/c_0$$

where

ρ = actual mass in grams per cubic centimeters

ϕ = actual pressure in kilobars

r = actual distance in centimeters

u = actual radial flow velocity in centimeters/second

w = actual angular flow velocity in centimeters/second

e = actual total energy in joules per gram

t = actual time in seconds

ρ_0 = normal density of target

ϕ_0 = 1 kilobar

a = radius of micrometeoroid in centimeters

The computer solution which yields D, U, W, and E as functions of time and space is obtained in the following manner:

1. Specify $D^N_{L,M}$, $U^N_{L,M}$, $W^N_{L,M}$, $E^N_{L,M}$, and $P^N_{L,M}$: and the values of D, U, W, and P at the center of each cell of the mesh at time N.

2. Solve equations 18, 22, 23, and 24 for $D^{N+1}_{L,M}$, $U^{N+1}_{L,M}$, $W^{N+1}_{L,M}$, and $E^{N+1}_{L,M}$; the values of D, U, W, and E at the center of each cell in the mesh at time (N + 1).
3. Solve the equations of state for $P^{N+1}_{L,M}$.
4. Print out the values of $D^{N+1}_{L,M}$, $U^{N+1}_{L,M}$, $W^{N+1}_{L,M}$, $E^{N+1}_{L,M}$, and $P^{N+1}_{L,M}$.
5. Replace each value $D^{N}_{L,M}$ with $D^{N+1}_{L,M}$, $U^{N}_{L,M}$ with $U^{N+1}_{L,M}$, $W^{N}_{L,M}$ with $W^{N+1}_{L,M}$, $E^{N}_{L,M}$ with $E^{N+1}_{L,M}$, and $P^{N}_{L,M}$ with $P^{N+1}_{L,M}$.
6. Increase time by an amount Δt.
7. Repeat steps 2 through 5 until the desired time, t_F.

The digital process is illustrated in Figure 7.

Let X represent any of the variables D, U, W, E, or P. In order to solve equations 18, 22, 23, and 24 for $D^{N+1}_{L,M}$, $U^{N+1}_{L,M}$, $W^{N+1}_{L,M}$, and $E^{N+1}_{L,M}$, it is necessary to be able to evaluate terms of the form

$$X^{N}_{L+\frac{1}{2},M}$$

$$X^{N}_{L-\frac{1}{2},M}$$

$$X^{N}_{L,M+\frac{1}{2}}$$

$$X^{N}_{L,M-\frac{1}{2}}$$

which are the values of the variables D, U, W. E, and P at the cell sides 2, 4, 3, and 1 respectively. Three types of averaging are used to evaluate these cell side terms from the known values of the variables at the centers of the cells. The averaging schemes are discussed in references 22 and 32. Three averaging schemes are listed below:

Type I

$$X^{N}_{L+\frac{1}{2},M} = \frac{1}{2}\left(X(L,M) + X(L+1,M)\right)$$

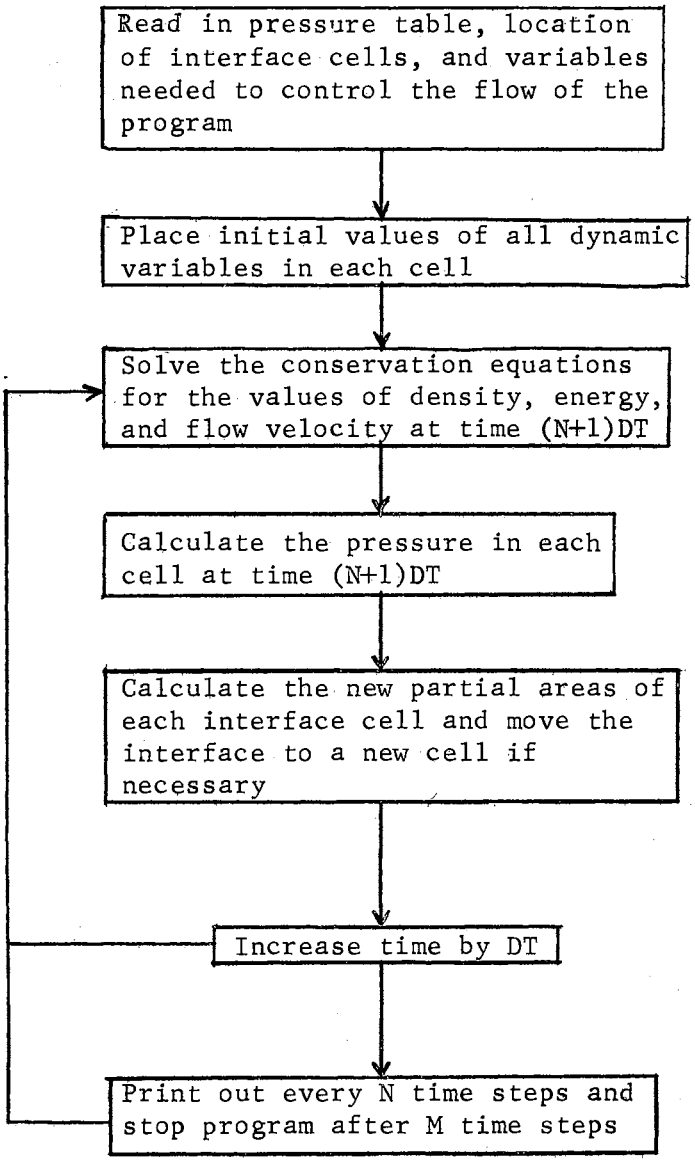

Figure 7. Flow Chart of Computer Program

$$X^{N}_{L,M+\frac{1}{2}} = \frac{1}{2}\left(X(L,M) + X(L,M+1)\right)$$

Type II

$$\begin{aligned} X^{N}_{L+1/2,M} &= X(L,M) && V>0 \\ &= 0 && V=0 \\ &= X(L+1,M) && V<0 \end{aligned}$$

$$\begin{aligned} X^{N}_{L,M+1/2} &= X(L,M) && V>0 \\ &= 0 && V=0 \\ &= X(L,M+1) && V<0 \end{aligned}$$

Type III

$$\begin{aligned} X^{N}_{L+1/2,M} &= \tfrac{3}{4}X(L,M) + \tfrac{3}{8}X(L+1,M) - \tfrac{1}{8}X(L-1,M) && V>0 \\ &= 0 && V=0 \\ &= \tfrac{3}{4}X(L+1,M) + \tfrac{3}{8}X(L,M) - \tfrac{1}{8}X(L+2,M) && V<0 \end{aligned}$$

$$\begin{aligned} X^{N}_{L,M+1/2} &= \tfrac{3}{4}X(L,M) + \tfrac{3}{8}X(L,M+1) - \tfrac{1}{8}X(L,M-1) && V>0 \\ &= 0 && V=0 \\ &= \tfrac{3}{4}X(L,M+1) + \tfrac{3}{8}X(L,M) - \tfrac{1}{8}X(L,M+2) && V<0 \end{aligned}$$

A test velocity, V, is defined as

$$V = U(L,M) + U(L+1,M)$$

for $X^{N}_{L+\frac{1}{2},M}$; and as

$$V = W(L,M) + W(L,M+1)$$

for $X^N_{L,M+\frac{1}{2}}$. The equations for $X^N_{L-\frac{1}{2},M}$ and the test velocity V are obtained by subtracting 1 from the L index. The equations for $X^N_{L,M-\frac{1}{2}}$ and its test velocity are obtained by subtracting 1 from the M index.

Special averaging techniques must be used to evaluate these cell side terms at the boundaries of the finite difference mesh since the number of neighboring cells is reduced there. The mesh coordinates are confined to

$$1 \leq L \leq LN$$

$$1 \leq M \leq MN$$

As an example, if L=1, then there is no X(L-1,M) so Types I or III cannot be used to evaluate $X^N_{L-\frac{1}{2},M}$. Similarly, if M=1, there is no X(L, M-1); if L=LN, there is no X(L+1, M); and if M=MN, there is no X(L, M+1). Different but similar problems exist. The following system is employed to evaluate the cell side variables at the mesh boundaries:

$L=1$ $\quad X^N_{L-1/2,M} = X(1,M)$

$\quad X^N_{L+1/2,M} = \text{TYPE I}$

$L=LN$ $\quad X^N_{L-1/2,M} = \text{TYPE I}$

$\quad X^N_{L+1/2,M} = X(LN,M)$

$M=MN$ $\quad X^N_{L,M-1/2} = \text{TYPE I}$

$\quad X^N_{L,M+1/2} = X(L,MN)$

$M=1$ $\quad X^N_{L,M-1/2} = X(L,1)$

$\quad X^N_{L,M+1/2} = \text{TYPE I}$

The following exception was made for the boundary, M=1, which is the Z axis. This axis is an axis of symmetry so the variables on one side of the axis are mirror images of the variables on the opposite side,

and there is no flow of material across the Z axis. As an example, for M=1, $X_{L,M-\frac{1}{2}} = 0$ if X is W, the angular flow velocity.

The finite difference forms of equations 18, 22, 23, and 24 that are incorporated into the computer program consist of the following.

$$CD(L,M) = D(L,M) + DT*((R4*R4*D4*U4 - R2*R2*D2*U2)/(R*R*DR) + (D1*W1*XT1 - D3*W3*XT2)/(R*XT*D\theta)) \quad (25)$$

$$CU(L,M) = (D(L,M)*U(L,M) + DT*((R4*R4*D4*U4*U14 - R2*R2*D2*U2*U12)/(R*R*DR) + (D1*W1*XT1*U11 - D3*W3*XT2*U13)/(R*XT*D\theta) + XND*XNW*XNW/R + (P4-P2)/DR))/CD(L,M) \quad (26)$$

$$CW(L,M) = (D(L,M)*W(L,M) + DT*((R4*R4*D4*U4*W14 - R2*R2*D2*U2*W12)/(R*R*DR) + (D1*W1*XT1*W11 - D3*W3*XT2*W13)/(R*XT*D\theta) - XND*XNW*XNU/R - (P3-P1)/(R*D\theta)))/CD(L,M) \quad (27)$$

$$CE(L,M) = (D(L,M)*E(L,M) + DT*((R4*R4*D4*U4*E14 - R2*R2*D2*U2*E12)/(R*R*DR) + (D1*W1*XT1*E11 - D3*W3*XT2*E13)/(R*XT*D\theta) + (R4*R4*P4*U14 - R2*R2*P2*U12)/(R*R*DR) + (P1*W1*XT1 - P3*W3*XT2)/(R*XT*D\theta)))/CD(L,M) \quad (28)$$

The nonsubscripted variables in the equations are the cell side values. The definition of each variable and the type of averaging used to evaluate it are listed below:

$D1 = D^N_{L,M-1/2}$	TYPE III
$D2 = D^N_{L+1/2,M}$	TYPE III
$D3 = D^N_{L,M+1/2}$	TYPE III
$D4 = D^N_{L-1/2,M}$	TYPE III
$U2 = U^N_{L+1/2,M}$	TYPE III
$U4 = U^N_{L-1/2,M}$	TYPE III
$W1 = W^N_{L,M-1/2}$	TYPE III
$W3 = W^N_{L,M+1/2}$	TYPE III
$P1 = P^N_{L,M-1/2}$	TYPE I
$P2 = P^N_{L+1/2,M}$	TYPE I
$P3 = P^N_{L,M+1/2}$	TYPE I
$P4 = P^N_{L-1/2,M}$	TYPE I
$U11 = U^N_{L,M-1/2}$	TYPE II
$U12 = U^N_{L+1/2,M}$	TYPE II
$U13 = U^N_{L,M+1/2}$	TYPE II
$U14 = U^N_{L-1/2,M}$	TYPE II
$W11 = W^N_{L,M-1/2}$	TYPE II
$W12 = W^N_{L+1/2,M}$	TYPE II
$W13 = W^N_{L,M+1/2}$	TYPE II
$W14 = W^N_{L-1/2,M}$	TYPE II
$E11 = E^N_{L,M-1/2}$	TYPE II
$E12 = E^N_{L+1/2,M}$	TYPE II
$E13 = E^N_{L,M+1/2}$	TYPE II
$E14 = E^N_{L-1/2,M}$	TYPE II

Some variables are not averaged. These variables are listed below.

$$XT1 = \sin\theta^{N}_{L,M-1/2}$$

$$XT = \sin\theta^{N}_{L,M}$$

$$XT2 = \sin\theta^{N}_{L,M+1/2}$$

$$R4 = R^{N}_{L-1/2,M}$$

$$R2 = R^{N}_{L+1/2,M}$$

$$R = R^{N}_{L,M}$$

In addition, some variables are linear time averages, rather than space averages. The time averaged quantities are

$$XND = D^{N+1/2}_{L,M}$$

$$XNU = U^{N+1/2}_{L,M}$$

$$XNW = W^{N+1/2}_{L,M}$$

These same differencing schemes are employed to convert the elastic and the plastic terms into the finite difference form. The converted elastic and plastic equations will not be given because they are quite lengthy and cumbersome to write out in detail.

Tag System

A system of cell tags was devised in order to follow the motion of the physical boundaries through the two dimensional mesh. The sign

and the magnitude of a cell tag determine the material in the cell, and the computer operations which may occur in the cell. The tags and their meanings are listed below.

Tag (L,M)	Meaning
-3.0	Cell (L,M) is completely filled with fluid rock and fluid aluminum.
-2.0	Cell (L,M) is completely filled with fluid rock.
-1.0	Cell (L,M) is partially filled with fluid rock.
0.0	Cell (L,M) is completely empty.
+1.0	Cell (L,M) is partially filled with fluid aluminum.
+2.0	Cell (L,M) is completely filled with fluid aluminum
+3.0	Cell (L,M) is partially filled with fluid rock and fluid aluminum.
+4.0	Cell (L,M) is filled with plastic aluminum
+5.0	Cell (L,M) is filled with elastic aluminum

The boundary of the rock micrometeoroid is determined by the coordinates of the cells whose tags are -3.0, -1.0, and +3.0. It must be possible to connect these coordinates with a smooth, unbroken line, or a bookkeeping error has occurred within the computer program. Every cell inside this boundary must have a tag of -2.0. The aluminum surface is determined by the coordinates of those cells whose tags are -3.0, +1.0, or +3.0.

Suppose that the boundary of the rock is to be determined. Let T represent any of the values -3.0, -1.0, or 3.0; any one of which

would imply that a rock boundary is in a particular cell. There are then six possible ways that the T's may be arranged in the two dimensional mesh so that the rock would have a continuous boundary. Each one of these six arrangements represents two possible ways that the rock could be located in the cell. The possibilities are shown in Figure 8; the shaded region represents the rock in the cell.

The twelve possible rock boundary configurations are identical to the twelve possibilities that Rich employs to describe fluid flow in a two dimensional mesh (28). A system of bookkeeping was devised which allows only these six possible arrangements of the tags -3.0, -1.0, and +3.0. The same system was used for the tags -3.0, +1.0, and +3.0 for the aluminum surface.

The rock material is moving in such a manner that a cell partially filled with rock will either completely fill, or empty. The tag of this cell will then change from -1.0 to some other tag value. The new tag value is completely determined by examining the values of ARO(L,M), the area of the cell (L,M) that is occupied by rock; and AAL(L,M), the area of cell (L,M) that is occupied by aluminum. These values are compared with the total area of the cell (L,M). Let X represent the area of cell (L,M). The following table shows the manner in which changes in ARO, or AAL may change the tag of -1.0. The methods employed to calculate the changes in ARO and AAL will be discussed in the next section.

Other allowed tag changes that involve physical boundaries are:

-3.0 may change to -2.0, +2.0 or +3.0

-2.0 may change to -1.0, or -3.0

0.0 may change to -1.0, +1.0 or +3.0

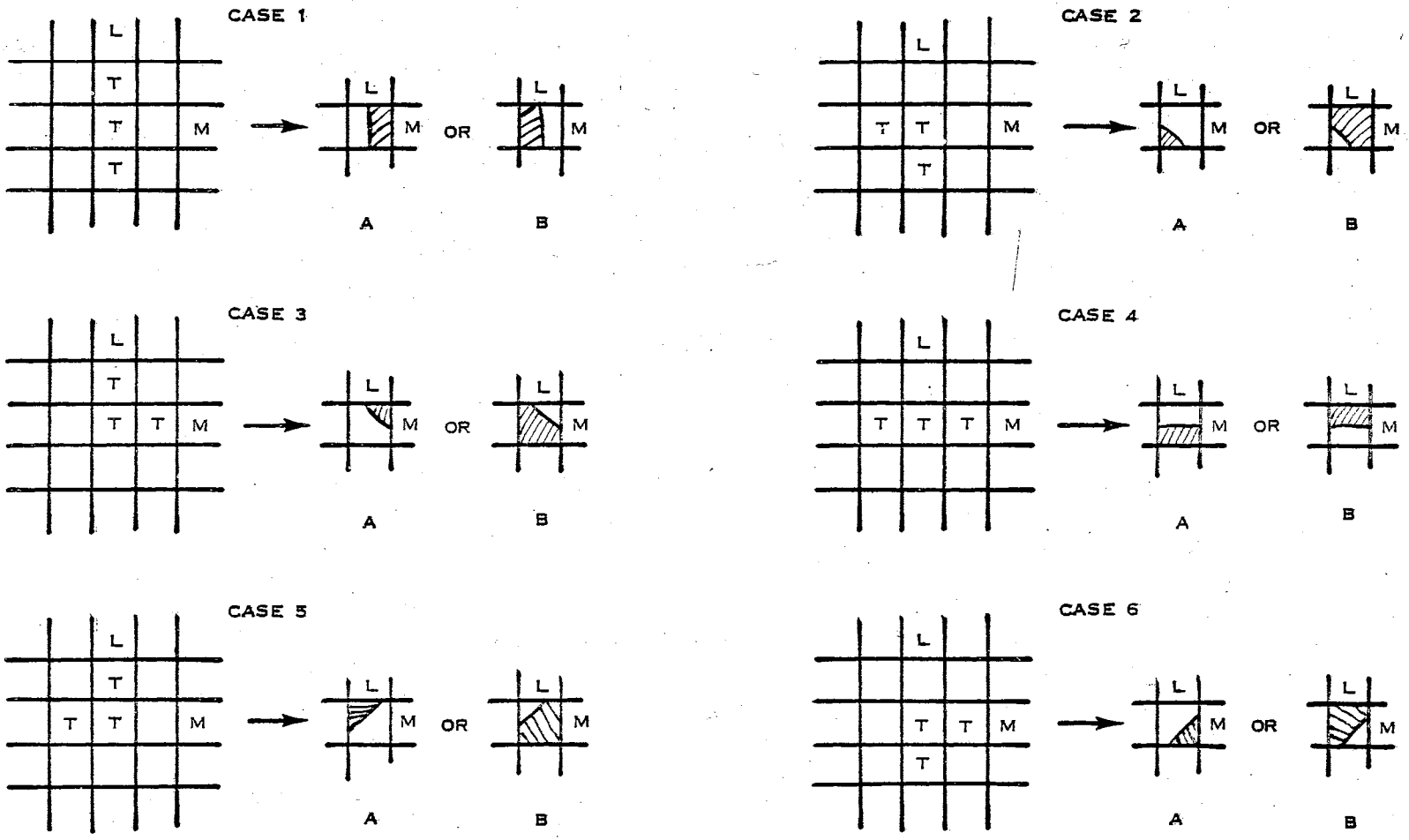

FIGURE 8 – SIX TYPES OF BOUNDARY CELLS

TABLE II

POSSIBLE TAG CHANGES FOR A CELL PARTIALLY FILLED WITH ROCK

Time = t	Time = t + Δt	New Tag Value For Cell (L,M)
AAL(L,M) = 0.0	AAL(L,M) = 0.0	0.0
0.0 < ARO(L,M) < X	ARO(L,M) = 0.0	
AAL(L,M) = 0.0	AAL(L,M) = 0.0	-2.0
0.0 < ARO(L,M) < X	ARO(L,M) $\geq$ X	
AAL(L,M) = 0.0	AAL(L,M) > 0.0	
0.0 < ARO(L,M) < X	ARO(L,M) > 0.0	+3.0
	ARO(L,M) + AAL(L,M) < X	
AAL(L,M) = 0.0	AAL(L,M) > 0.0	
0.0 < ARO(L,M) < X	ARO(L,M) > 0.0	-3.0
	ARO(L,M) + AAL(L,M) $\geq$ X	

+1.0 may change to +2.0, +3.0, -3.0 or 0.0

+2.0 may change to +1.0, or -3.0

+3.0 may change to -3.0, -1.0, 1.0 or 0.0

A change in the tag value of the cell (L,M) will always induce a tag change in neighboring cells. For example, suppose that the tag of cell (L,M) is -1.0, and the cell is represented by Case 1 of Figure 8. If TAG(L,M) changes to 0.0, then TAG(L-1,M) changes to -1.0 if the configuration is Case 1a, or the tag of cell (L+1,M) changes to -1.0 if the configuration is Case 1b. The induced tag changes for Cases 2, 3, 5, and 6 are more complicated. The induced changes when the tag of cell (L,M) is -3.0, or +3.0, is more difficult to determine for all of the Cases. The induced tag change is always governed by the fact that the final tag arrangement in cell (L,M) and its eight immediate neighbors must reduce to one of the six allowed possibilities.

Almost all numerical operations are controlled by the tag value. For example, when the pressure in cell (L,M) is calculated, there are different equations of state that could be used for the calculation. The tag of cell (L,M) determines which equation of state is used. If TAG(L,M)=+2.0, Tillotson's equation for aluminum should be used. If TAG(L,M)=-2.0, the tabular equation of state for rock should be used. If TAG(L,M)=+4.0, the plastic equation of state is used. If TAG(L,M)= 0.0, the cell contains no material so the program skips the cell and does no numerical calculations.

This tag system is the foundation upon which the entire computer program is built.

Methods to Change Partial Areas of Boundary Cells

In this thesis, a boundary cell is defined as any cell which contains an interface. A cell contains a partial area if the area of rock and/or aluminum in the cell is less than the area of the cell. The interface may be either rock-aluminum, rock-vacuum, or aluminum-vacuum. The fundamental difficulty in solving a fluid flow problem is in following the motion of such interfaces. An interface is made to move through a cell by altering the area of rock and/or aluminum in the cell. The problem of following physical boundaries is basically the determination of sufficiently accurate methods to be employed to approximate changes in the partial areas of boundary cells.

Rich suggests a method to calculate the partial area of a cell that is good for rectangular mesh cells (28). A fundamental assumption in Rich's method is that a physical boundary such as ABC in Figure 9 may be replaced by the straight line AC. This assumption allows the partial areas of cells to be calculated as the areas of triangles or parallelograms. From these areas, the intercepts of the boundary with the cells sides, such as points a and b, may be determined. The interface motion may be followed by monitoring the motion of the intercept points.

Rich's method would work quite well for any coordinate system which would have rectangular mesh cells such as a Cartesian x-y system or the plane of a cylindrical system which contains the z axis. The method would not work well for the spherical coordinate system that is employed in this study. The partial areas of the mesh cells, such as the one in Figure 10, cannot be accurately represented as the areas of triangles or parallelograms except for large radii of curvature.

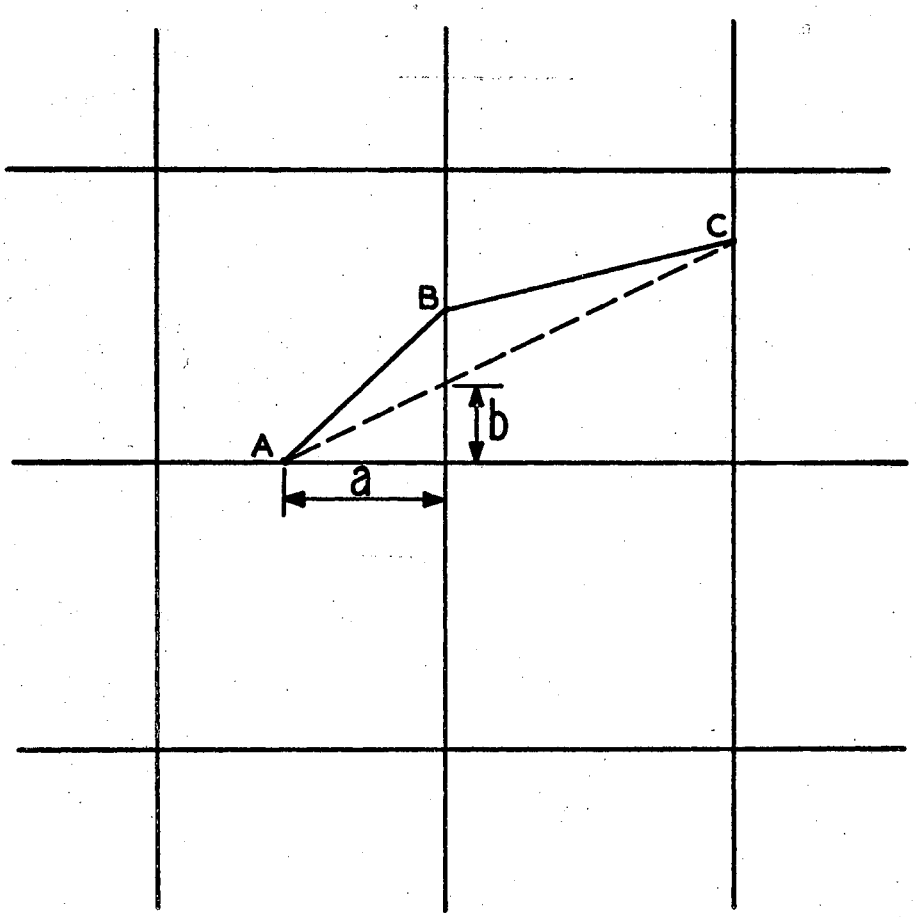

FIGURE 9 – APPROXIMATION OF PARTIAL CELL AREA IN RECTANGULAR MESH

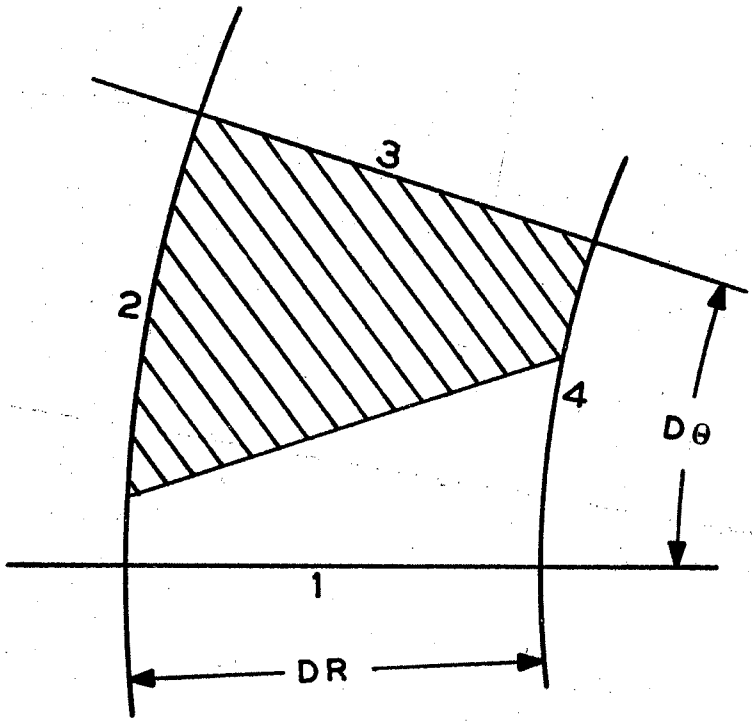

FIGURE 10 – PARTIAL AREA IN A SPHERICAL COORDINATE SYSTEM

Let A^N represent the partial area of a boundary cell at time $N\Delta t$ and A^{N+L} the area at time $(N+1)\Delta t$. Let X be the total area of the cell, DΘ the angle between cell sides 1 and 3, and DR the radial distance between sides 2 and 4. These cell sides are shown in Figure 10. Let R2 and U2 represent the radial distance and radial flow velocity at cell side 2, and R4 and U4 represent the radial distance and radial flow velocity at cell side 4. Let W1 and W3 be the angular flow velocities at sides 1 and 3 respectively.

The change in cell area is found by calculating the difference in the flow in and the flow out of the cell. The flow in or out of side 2 during time DT is

$$\pm U2 * R2 * DTH2 * DT$$

where (R2)(DTH2) is the length of side 2 that is open to cell (L+1,M). The flow in or out of side 4 during time DT is

$$\pm U4 * R4 * DTH4 * DT$$

where (R4)(DTH4) is the length of side 4 open to cell (L-1,M). These quantities are illustrated in Figure 11. The flow in or out of side 1 during time DT is

$$\pm W1 * XL1 * DT$$

where XL1 is the length of side 1 open to cell (L,M-1), and the flow in or out of side 3 during time DT is

$$\pm W3 * XL3 * DT$$

where XL3 is the length of side 3 open to cell (L,M+L). See Figure 12.

The change in cell area is given by

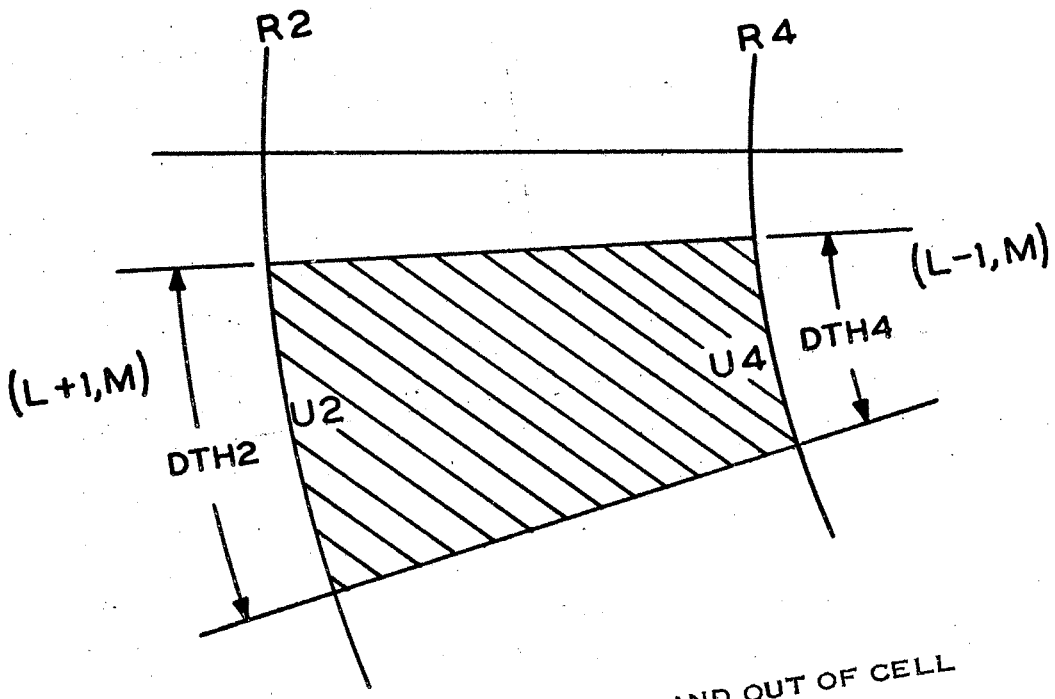

FIGURE 11 – RADIAL FLOW IN AND OUT OF CELL

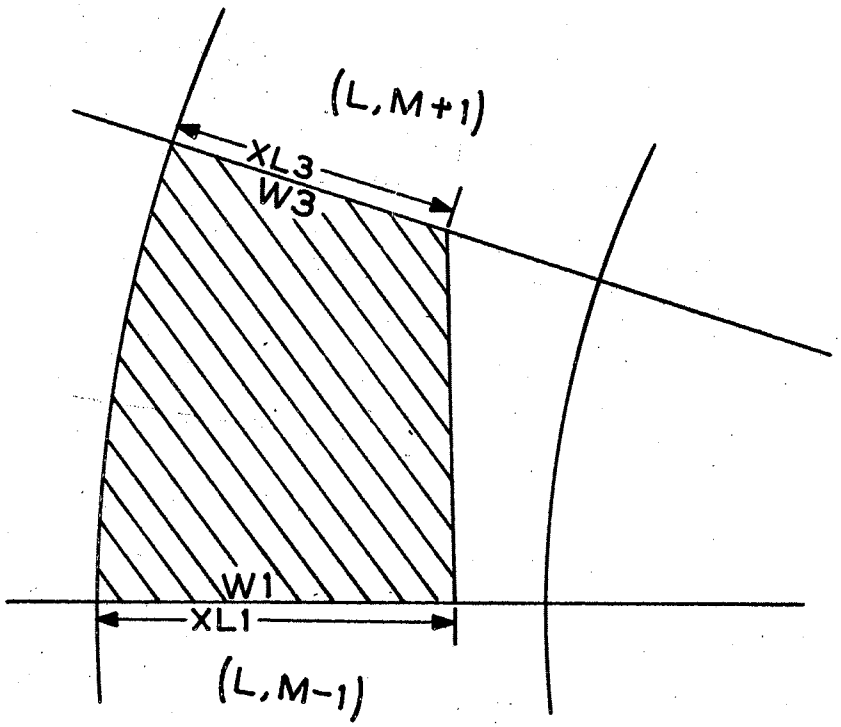

FIGURE 12 – ANGULAR FLOW IN AND OUT OF CELL

$$A^{N+1} = A^{N} + \left[\pm U2 * R2 * DTH2 \quad \pm U4 * R4 * DTH4 \right.$$
$$\left. \pm W1 * XL1 \quad \pm \quad W3 * XL3 \right] * DT$$

The algebraic sign of each term is determined by the directions of U2, U4, W1, and W3 as well as the particular case of the possible six cell tag arrangements that is being considered. The calculations of DTH2, DTH4, XL1, and XL3 for each of the six cases are summarized in Figure 13.

These interpolation equations are simple and in many cases probably do not accurately describe changes in area. It is difficult to defend these equations from a purely mathematical argument. For this reason, the equations were subjected to the following test to determine if they would perform satisfactorily. A semicircle was placed on the Z axis of Figure 5 (Chapter III) so that its center was in cell 20. Each cell in the semicircle was given U and W components of velocity so that the resultant velocity was parallel to the Z axis. A computer program was then formulated to make the semicircle move along the Z axis until its center was in cell 30. The boundary of this semicircle was moved through the mesh by using the interpolation equations to increase, or decrease, the partial areas of the boundary cells. After moving 10 cells, the final semicircle was slightly distorted, but it represented the original semicircle accurately enough for this author to have complete confidence in the simple linear interpolation that is employed to evaluate changes in the partial areas of interface cells.

The interface motion depends very strongly upon the size of the time increment DT. If DT is large enough so material traverses a cell in only two or three time steps, the interface becomes misshapened and

CASE 1

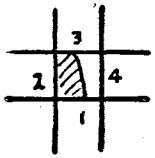

DTH2 = DΘ
DTH4 = 0
XL1 = (A/X)DR
XL2 = (A/X)DR

CASE 2

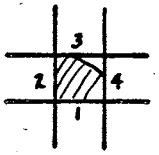

DTH2 = DΘ
XL1 = DR
A/X ~ 1/2 ⇒ XL3 ~ 0 & DTH4 ~ 0
A/X ~ 1 ⇒ XL3 ~ DR & DTH4 ~ DΘ
XL3 = (2A/X − 1)DR
DTH4 = (2A/X − 1)DΘ

CASE 3

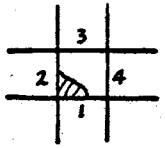

XL3 = 0
DTH4 = 0
A/X ~ 1/2 ⇒ XL1 ~ DR & DTH2 ~ DΘ
A/X ~ 0 ⇒ XL1 ~ 0 & DTH2 ~ 0
XL1 = (2A/X)DR
DTH2 = (2A/X)DΘ

CASE 4

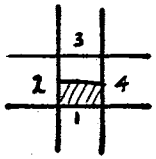

XL3 = 0
XL1 = DR
DTH2 = (A/X)DΘ
DTH4 = (A/X)DΘ

CASE 5

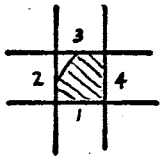

DTH2 = DΘ
XL1 = DR
A/X ~ 1 ⇒ DTH2 ~ DΘ & XL3 ~ DR
A/X ~ 1/2 ⇒ DTH2 ~ 0 & XL3 ~ 0
DTH2 = (2A/X − 1)DΘ
XL3 = (2A/X − 1)DR

CASE 6

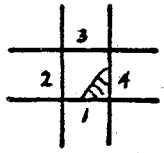

XL3 = 0
DTH2 = 0
A/X ~ 0 ⇒ XL1 ~ 0 & DTH4 ~ 0
A/X ~ 1/2 ⇒ XL1 ~ DR & DTH4 ~ DΘ
DTH4 = (2A/X)DΘ
XL1 = (2A/X)DR

FIGURE 13 – SIX CASES OF PARTIAL AREA

broken. To maintain a smooth continuous interface, and thus, to maintain a continuous impacting sphere, the time increment is chosen so that at least ten time steps are required for material to cross a mesh cell. In the computer program, DT is calculated from the equation

$$DT = \frac{DR}{C * UMAX}$$

where C is given a value between 10 and 15, and UMAX is the maximum value of the flow velocity in any cell in the mesh at time step N. Time steps of this size also result in smaller oscillations in the density, energy, and pressure profiles. The evaluation of the time step will be discussed further in the next chapter.

If the interface cell under consideration is completely filled by both aluminum and rock, the new value of the area occupied by rock is found from the interpolation equations, and the new value of the area occupied by aluminum is found from

$$AAL_{L,M}^{N+1} = X - ARO_{L,M}^{N+1}$$

where AAL is the aluminum area, ARO is the rock area, and X is the total cell area.

To conserve computer memory, the computer program that calculates the partial areas of the cells occupied by rock along the rock-vacuum interface and by aluminum along the aluminum-vacuum interface at time t = 0 was formulated and executed separately from the main impact program. The output of this area calculation program was then used as input data for the impact program.

At time t = 0.0, the rock-vacuum interface is the boundary of a semi-circle with its center at $(r, \theta, \phi) = (b, 0, 0)$ on the z axis, and it

has the radius, a. See Figures 5 and 14. The target surface is represented by a plane normal to the z axis and intersecting the axis at z = (a+b). The equation of the circle in the yz plane is

$$r^2 = a^2 + 2br\cos\theta - b^2 \tag{29}$$

and the equation of the straight line DE that represents the aluminum surface is

$$r = (a+b)/\cos\theta \tag{30}$$

The area occupied by rock at boundary cells such as at point A is evaluated as shown in Figure 15. The function $f(r, \theta)$ is the equation of the circle from Equation 29. For points such as D and C, the limits of r are changed to an integration from R_1 to $f(r, \theta)$. The area that is occupied by aluminum at a point such as E is calculated by the same expression except $f(r, \theta)$ is the equation of the straight line from Equation 30.

The complexity of the integration increases when $f(r, \theta)$ intersects either sides 2 or 4 of the cell. In such cases, the angle θ_s in Figure 16 serves as one limit of integration. This angle can be easily found by setting $f(r, \theta) = c$ where c is set equal to either R_1 or R_2.

Expansion of Mesh

Limitations of computer memory permitted only 1200 cells in the finite difference mesh. The last radial cell on the z-axis lies three sphere radii below the original position of the surface of the target (Figure 17). The mesh scale in Figure 17 is greatly exaggerated. When the shock front has propagated a distance equal to 3R, the mesh is filled, and no further time steps of the solution may be calculated

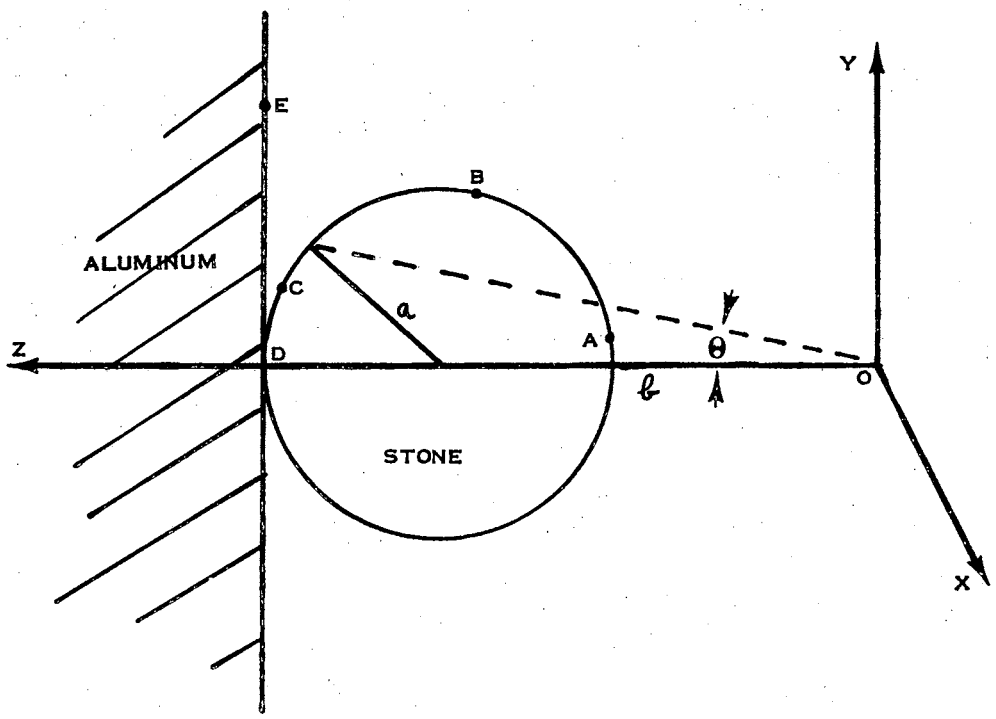

FIGURE 14 – PHYSICAL BOUNDARIES AT TIME T = O

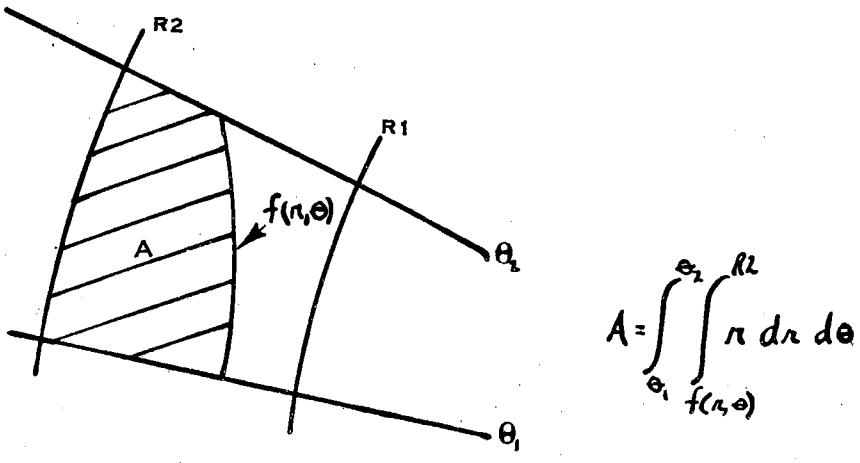

FIGURE 15 – CALCULATION OF PARTIAL AREA

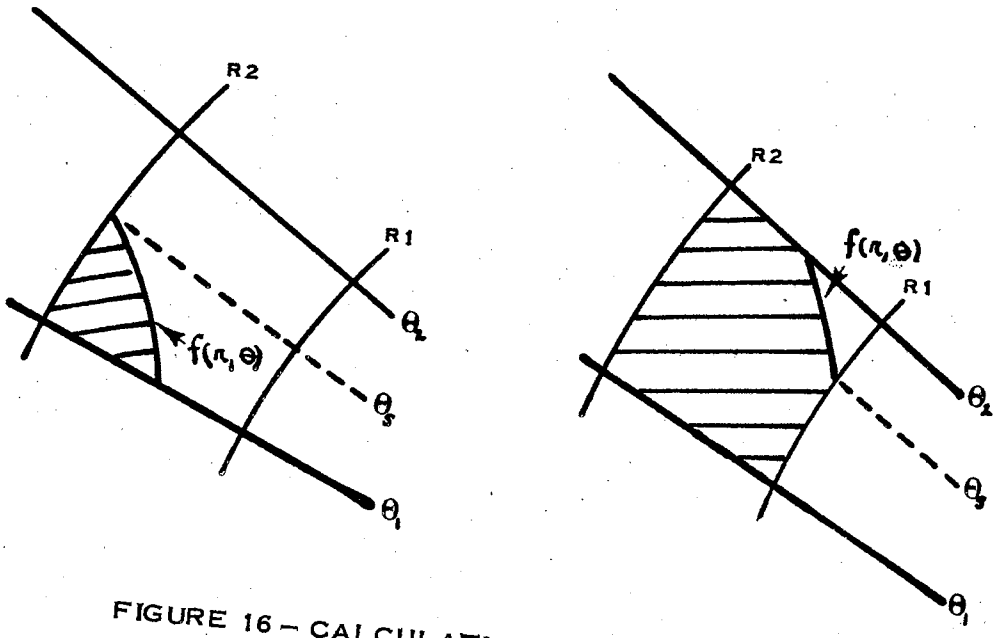

FIGURE 16 – CALCULATION OF PARTIAL AREA

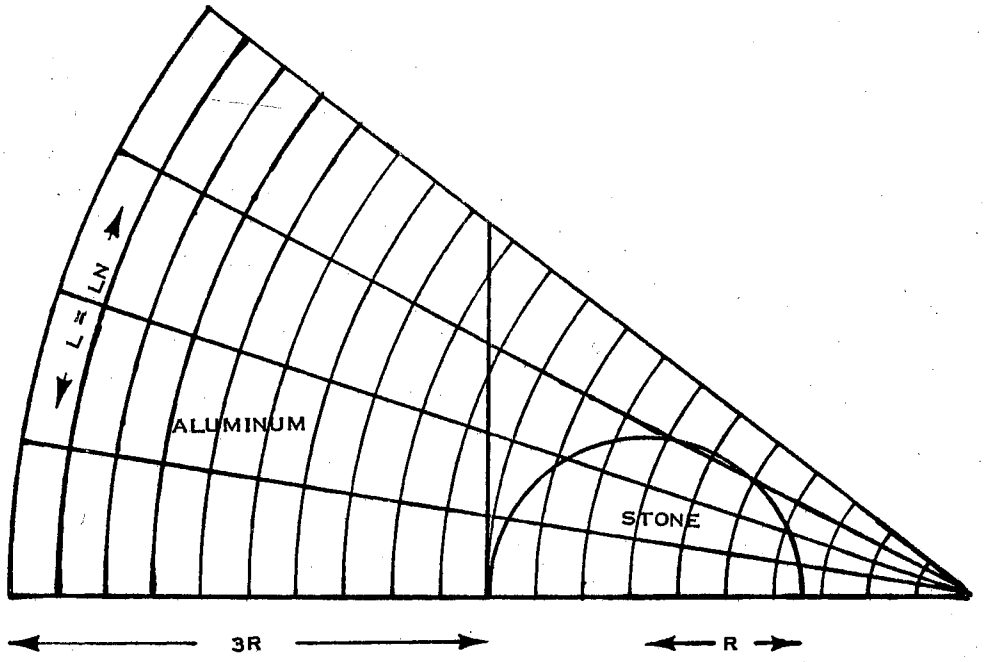

FIGURE 17 – DEPTH TO WHICH FINITE DIFFERENCE MESH PENETRATES TARGET AT TIME T = 0

until undisturbed cells are placed in front of the shocked region.

An undisturbed region is created ahead of the shock front by a condensation of the mesh. This condensation process averages the flow variables in cells (L,M) and (L-1,M), places this average in cell (L-1,M), and doubles the radial dimension of each cell. This process reduces the number of radial cells needed to describe the shocked region from LN to LN/2 and moves the shock front from L = LN to L = LN/2. A cell with L = LN/2 is still 3R below the original target surface position because the radial dimension of each cell has doubled. The radial cells from (LN/2+1,M) to (LN,M), now lies ahead of the shock front. They may be described as undisturbed cells, and the shocked region can expand into these cells. This condensation process is repeated until the shock parameters and flow variables have decreased to desired values.

This mesh condensation may be reversed if space resolution is required for any reason. Instead of combining two cells into one cell and doubling the cell size, a single cell could be divided into N cells. This mesh resolution is performed when the dual shock wave region is created. The plastic region is quite thin, and its physical width could lie totally within a single cell if several mesh condensations have occurred. A single cell could not describe the details of this region; therefore, the cell widths are decreased so that several cells are needed to traverse the width of the region. This resolution technique is illustrated in Figure 18. The widths of the cells preceding the zone (those cells for L $<$ LF) are not changed.

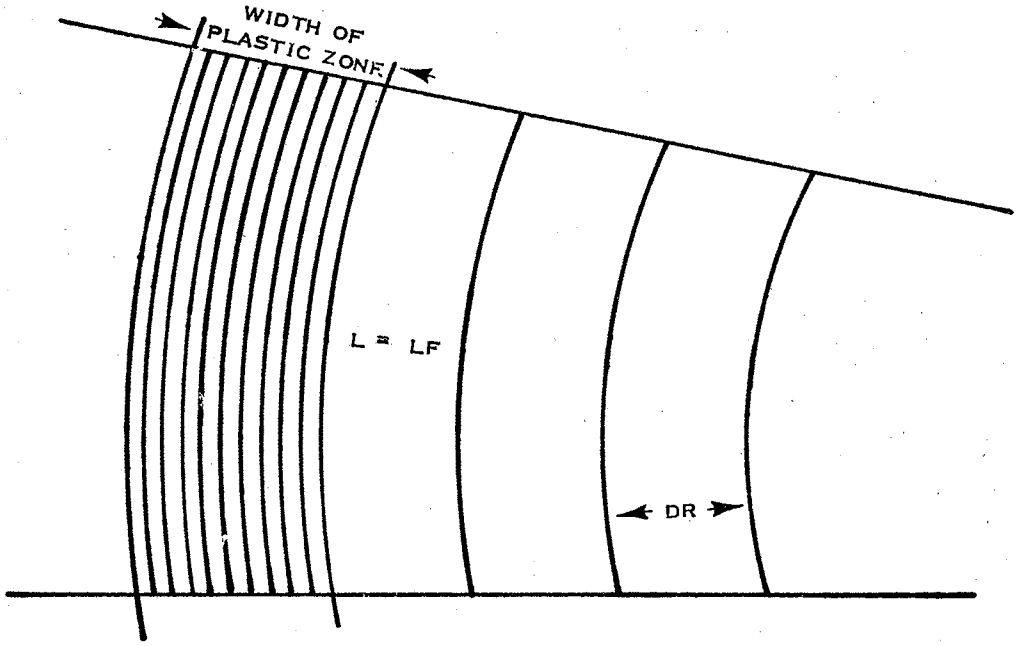

FIGURE 18 – DECREASING CELL WIDTHS TO OBTAIN RESOLUTION IN PLASTIC ZONE

CHAPTER IV

DISCUSSION OF SOLUTIONS

Uniqueness and Convergence

The solution of any initial value problem should be subjected to the following question:

1. Is the solution unique?

A finite difference solution of an initial value problem should be subjected to the additional investigation:

2. Is the finite difference solution an accurate approximation to the true solution?

Closely associated with the first question is the concept of a "well-set" initial value problem. A one dimensional initial value problem is said to be well-set in a domain D when there is one and only one solution $y = f(x,c)$ in D of the given differential equation for each given (x,c) in D, and when this solution varies continuously with c. To show that the problem is well-set; therefore, requires proving theorems of existence (there is a solution); uniqueness (there is only one solution); and continuity (the solution depends continuously on the initial value). Solutions which do not have these properties are useless physically, because no physical measurement is exact. The concept of a well-set initial value problem gives a precise mathematical interpretation to the physical concept of determinism. It is generally believed that the inviscid, compressible-fluid equations give rise to a

system of partial differential equations which define a well-set initial value problem. The effect on these properties that result from the addition of elastic, or plastic, stress tensor terms to the inviscid fluid equation is difficult to determine in a rigorous mathematical sense.

The second question, the convergence of the finite difference solution to the true solution, may be established by the following methods:

1. Compare the approximate solution to the true solution.
2. Compare the solution obtained using different values of the mesh parameters ΔR, $\Delta \theta$, and ΔT.
3. Compare the solution with the conditions demanded by the Theorem of Lax.

The first method is the most powerful of the three if a true solution exists for comparison. In the case of hypervelocity impact problems, there is no true solution against which to compare the finite difference solution because no closed mathematical solution has been obtained. The "true" solution, which must be employed, is the solution that results via experimental studies of the problem. Extensive, experimental studies have been performed at low velocities (< 10 km/sec), but it has been difficult to explore the upper range of micrometeoroid velocities (> 36 km/sec). The impact parameter measured in experimental studies is almost always the crater size. This author knows of no experimental solution which has obtained the details of the impact process; i.e., the peak pressure of the shock wave, the quantity of momenta and energy carried away by the target ejecta, the direction and magnitude of the material flow, etc. As a consequence, a comparison of

the finite difference solution to the "true" solution is necessarily confined to a comparison of the size and shape of the crater which is predicted by the computer solution to the size and shape which is established by experimental studies. These comparisons will be emphasized later in this chapter.

The second method insures that the solution is not just a set of numbers dependent upon the parameters of the finite difference mesh. If a mesh of ΔR_1, $\Delta\theta_1$, and a mesh of ΔR_2, $\Delta\theta_2$, result in substantially different numerical solutions then no unique solution exists. If the solutions do agree, the solution may or may not be unique.

The third test uses the Equivalence Theorem of Lax which states (29):

> Given a properly posed initial value problem and a finite difference approximation to it that satisfies the consistency conditions, stability is the necessary and sufficient condition for convergence.

The consistency condition requires:

1. The numerical solution depends continuously on the initial data, and
2. The difference equations convert into the partial differential equations as ΔR, $\Delta\theta$, and ΔT approach zero.

Both of these requirements are satisfied by the finite difference solution. The fact that the second requirement is satisfied is obvious. The first requirement is also satisfied since each iteration of the solution proceeds from updated initial data.

A numerical solution is stable if there are no unbounded numerical oscillations in the space and time profiles. A stable solution may be

oscillatory as long as the oscillations are small, or grow smaller with time.

Richtmyer has shown that stability can be insured by a proper choice of the time step ΔT (29). If $\vec{\Delta X}$ is the vector between two space points of interest in the finite difference mesh, then a relation that must be satisfied in order to have stable solutions in the interval $\vec{\Delta X}$ is the Courant condition

$$\Delta T \leq \frac{\vec{\Delta X}}{C + |\vec{V}|}$$

where C is the speed of sound in the medium, $\vec{V}$ is the material velocity, and ΔT is the time step. Tests conducted at Oklahoma State University have shown that stability is insured if the time step is calculated from the condition

$$\Delta T = \frac{\Delta R}{k(|V_{MAX}| + C)}$$

where k is a constant with a value between 10 and 15, V_{max} is the largest value of the material velocity which was found in the finite difference mesh, and ΔR is the smallest dimension of any cell.

The solutions obtained in this thesis have been subjected to these three tests, and the solutions do imply uniqueness and convergence to the true solution.

Presentation of Solutions

In the study of crater formation and shock propagation for this thesis, all computer solutions are for impacts onto a very thick slab of solid aluminum (semi-infinite solid). Three parameters are varied for the incident sphere (micrometeoroid); these parameters are:

1. Velocity of the incident sphere
2. Density of the incident sphere
3. Diameter of the incident sphere.

The particular combination of numerical values for these parameters in each of the solutions are listed in Table III. In the table, V is the velocity of the impacting sphere, D is the mean density of the sphere, and M is the mass of the sphere. A comment is necessary in regard to the numerical values for the density. The density of the solid aluminium target is 2.78 grams per cubic centimeter. The impacting spheres are of quartz which has a solid density of 2.5 grams per cubic centimeter. The values for the density of the spheres in the table are all for porous quartz spheres with a fare volume of 1/5 for a density of 2.0 and a fare volume of 4/5 for a density of 0.5. The treatment of the equation of state for the porous materials follows the American improvements on the initial Russian suggestions, as was discussed earlier in this thesis.

TABLE III

VALUES OF THE VELOCITY, DENSITY, AND MASS OF THE IMPACTING SPHERE

	V (km/sec)	D (gm/cc)	M (gram)
Case 1	6.25	2	10^{-9}
Case 2	7.5	2	10^{-9}
Case 3	2.0	2	10^{-9}
Case 4	20	0.5	10^{-9}
Case 5	72	0.5	10^{-9}
Case 6	20	0.5	3.4×10^{-9}

The computer output data is reduced to curves which are divided into three groups for presentation:

1. crater solutions
2. pressure profiles
3. calculation of the momentum and energy of the ejecta

Crater Solutions

Effect of Velocity and Density

The sizes and shapes of the craters that are formed by the impacts are presented in the first group of curves since the crater is doubtlessly the most prominent feature of the impact. The crater diagrams show the direction and magnitude of the velocity of flow; the interface between the rock and the aluminum; the amount of rock in the crater; as well as the volume and the position of the fluid, plastic, and elastic regions of the target. The size of the impacting sphere is shown to scale in some figures in order to illustrate the relative size of the sphere and crater. The cross-hatched region in each figure represents the volume that is filled with rock. The position of the free surface of the aluminum target is indicated by the letter S. The material velocity is represented by arrows interspersed through the shocked region. The length of the arrow shows the velocity of flow to the scale that is shown on each figure. An arrowhead with no tail means that the material velocity at that point is much smaller than the velocity scale that is placed on the figure. The labeled dots along the z-axis are spaced at intervals of one, or two radii of the impacting sphere, as is designated on each figure. The shock front is drawn as a dashed line.

The crater solutions are arranged in the order of increasing impact velocity. The solutions for low impact velocities are of particular interest since they are in the range which permit comparison with experimental studies. The formation of the craters for an impact velocity of 6.25 kilometers per second are presented in Figures 19 to 21, and those for an impact velocity of 7.5 kilometers per second are presented in Figures 22 to 25. These craters are discussed as a group since they are just above the transition zone from high velocity to hypervelocity impact. True hypervelocity impact is usually not achieved until the impact velocity is more than twice the speed of sound in the impacting target. For aluminum, this would require a velocity that is greater than 10 kilometers per second.

The mass of micrometeoroids is defined to be less than 10^{-4} grams. The mass of the impacting spheres in these two solutions and in most subsequent solutions was selected to be 10^{-9} grams. The radius of a sphere of this mass is of the order of 10^{-4} centimeters. The magnitude of this diameter is very significant in order to appreciate the small time increments between each stage of the crater formation. The times are of the order of nanoseconds. The lowest velocity sphere (6.25 km/sec) will require less than two nanoseconds to travel a distance equal to its diameter when in free flight. The very small diameter explains the very short time for the early stages of the cratering. Most solutions in the literature are for larger projectiles which have masses of several grams, and the cratering times are of the order of microseconds.

These computer solutions for the formation of craters may be compared with experimental studies. One research group has studied the impact of aluminum projectiles on an aluminum target where the impact

velocity was 7.32 kilometers per second (34). The depths of the craters formed in these impacts averaged 2½ times larger than the radius of the impacting projectile. This crater size lies between the crater sizes calculated for 6.25 and 7.5 kilometers per second impacts, and this suggests that the numerical solutions are good. Kinslow has also studied hypervelocity impact on aluminum (15). At an impact velocity of 25,000 feet per second, the crater depth was slightly less than three projectile radii. This result agrees well with the computer calculations. In both of these studies, the aluminum projectiles had a density 25% greater than the density of the rock sphere used in this study.

The shock front propagates at approximately the same velocity as the velocity of the sphere until the sphere has penetrated a distance about equal to one sphere radius. At this point, the shock front separates from the rock-aluminum interface and steadily moves away from the slower traveling rock material. This behavior is illustrated in Figures 19 and 22. When the separation between the shock wave and the rock-aluminum interface is about R (R is the radius of the incident sphere), there is a distinct movement of material toward the periphery of the crater. Figures 20 and 23 illustrate this movement. This movement is the initiation of the ejecta and the resulting crater lip. Practically all of the material behind the shock front is in the fluid state.

The shock wave travels slower along the free surface where the pressure is zero, and this results in the shocked region assuming the shape of a pear. This shape occurred for all of the impact solutions that were obtained. The shaded regions in the figures represent the

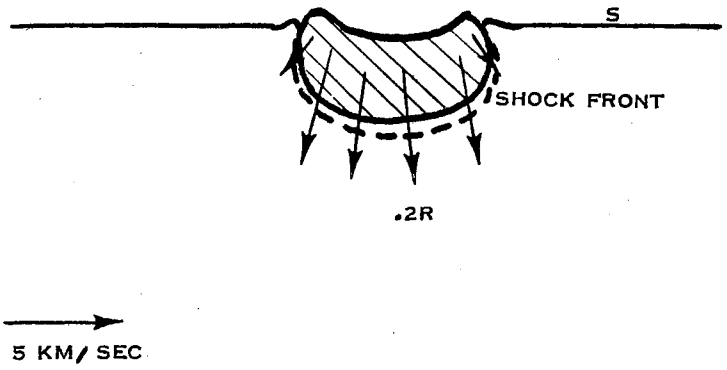

Figure 19. Crater at 7.9×10^{-10} second for sphere of density 2.0 gm/cc impacting at 6.25 km/sec.

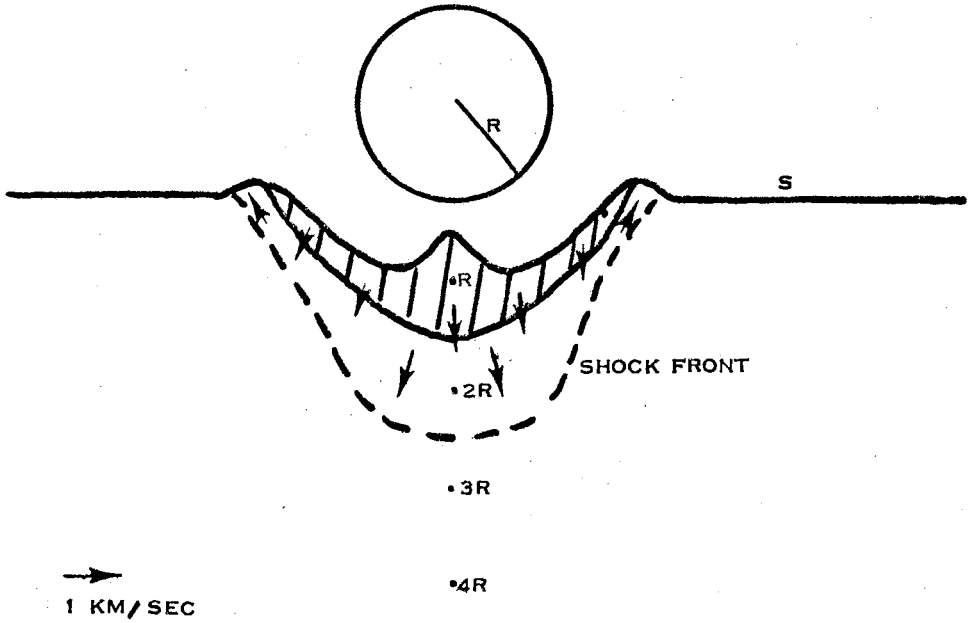

Figure 20. Crater at 1.6×10^{-9} second for sphere of density 2.0 gm/cc impacting at 6.25 km/sec.

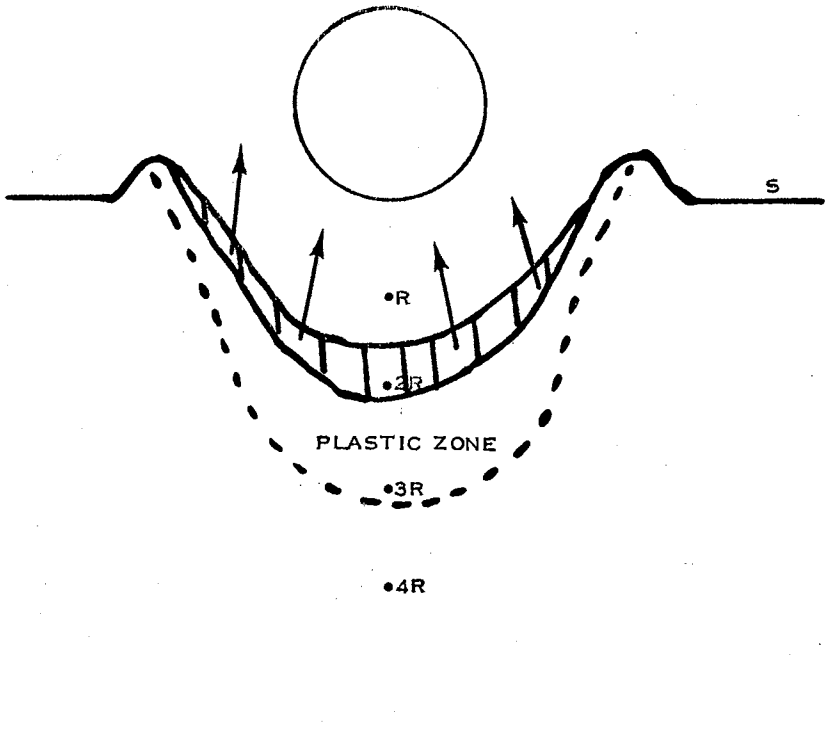

Figure 21. Crater at 2.5×10^{-9} second for sphere of density 2.0 gm/cc impacting at 6.25 km/sec.

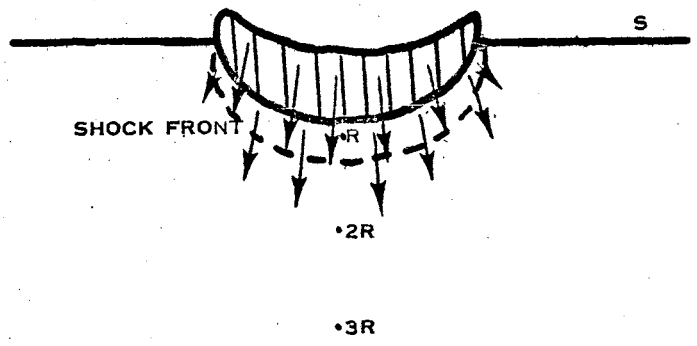

3.5 KM/SEC

Figure 22. Crater at 6.5×10^{-10} second for sphere of density 2.0 gm/cc impacting at 7.5 km/sec.

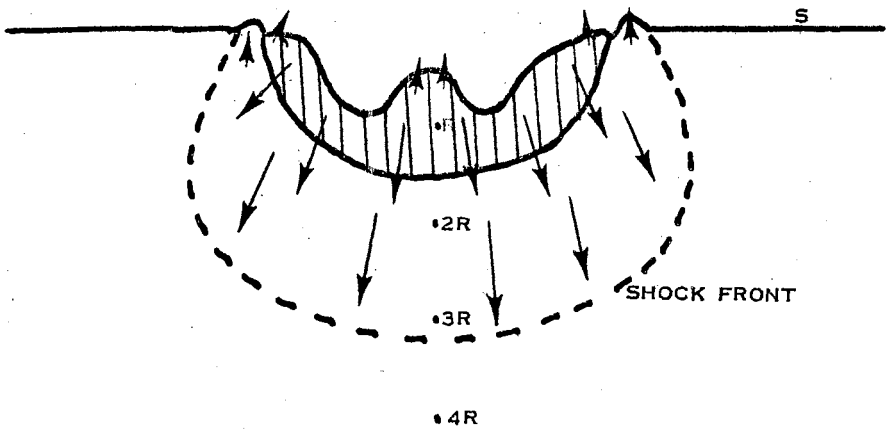

Figure 23. Crater at 1.9×10^{-9} second for sphere of density 2.0 gm/cc impacting at 7.5 km/sec.

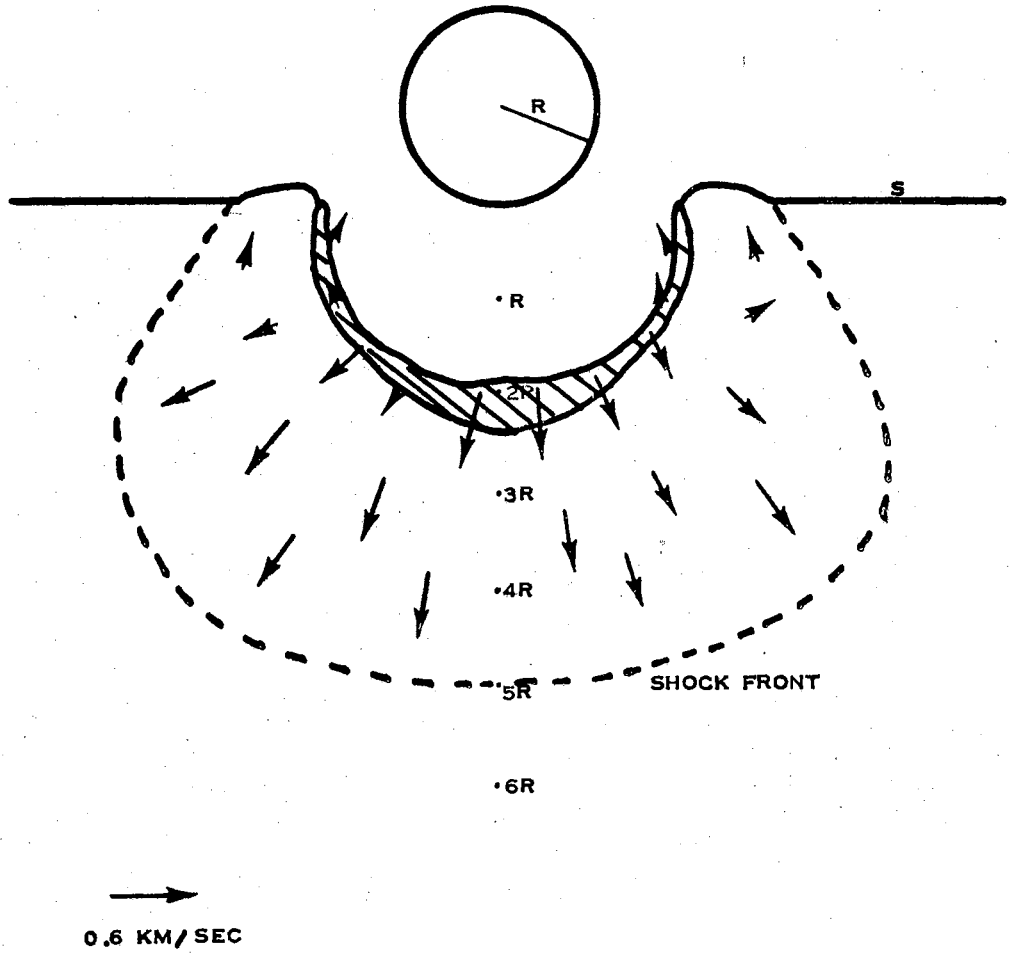

Figure 24. Crater at 3.0×10^{-9} second for sphere of density 2.0 gm/cc impacting at 7.5 km/sec.

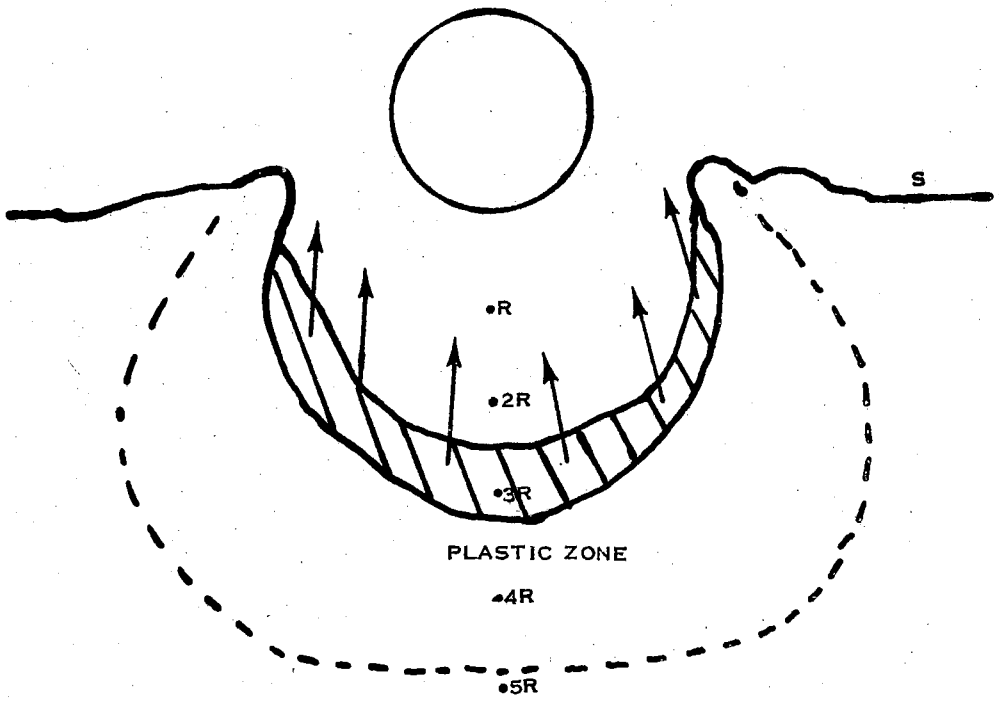

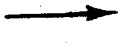

Figure 25. Crater at 4.7×10^{-9} second for sphere of density 2.0 gm/cc impacting at 7.5 km/sec.

volume occupied by rock. After the sphere penetrates a short distance into the target, the rock material becomes fluid, and the majority of it converts to a plasma.

The crater profiles in the last figure of the solution for each set of parameters shows a region which is labeled the "plastic zone". The boundary of this region that is nearer the target surface was determined with the following instructions to the computer. The computer was programmed to monitor the peak pressure of the propagating shock wave in the inviscid fluid until the peak pressure decreased to 137 kb. At that time, the energy in each cell was investigated and compared to the energy which is required to melt aluminum at zero pressure. The fluid-plastic boundary was placed on the line which separated the molten from the solid aluminum, as determined by the preceding instructions. This position is always in the region which has been over-run by the shock with a pressure in excess of 137 kb. The boundary between the plastic and the elastic regions was the position at which the pressure of the shock front decreases below 5.9 kb.

There is considerable uncertainty in the indicated procedure but this is a first approximation. A solution with this approximation serves to indicate the nature of the difficulties that are involved and to compare the results with experiment. The energy content to melt aluminum is probably somewhat dependent on the pressure (6). Available references are not very clear. Measurements on gallium show a 27.4 ^{o}C decrease in the melting point with a 12 kb increase in the pressure (40). In the form of the periodic table that shows the long periods, the elements from top to bottom in the same group are B, Al, Ga, In and Tl.

Between the two boundaries that define the plastic region, the shock wave has a dual wave structure which consists of an elastic precurssor wave that travels at the speed of sound in the elastic region and this wave is followed by a slower plastic wave. The viscosity terms were included in the equations of motion in this region. The total stress in this region and in the elastic region is defined as the quantity, t_{ij}, which is given by

$$t_{ij} = -P\delta_{ij} + S_{ij}$$

where P is the hydrodynamic pressure which is calculated from an equation of state, and S_{ij} is the stress from Equation 5 in Chapter II.

The difference between these solutions and those in the literature is in the location and the size of the plastic region. Very few hypervelocity impact solutions have been published which attempt to reveal the elastic-plastic conditions at long solution times. Previous solutions by Wagner, et al., and by Kinslow ignore the existence of any plastic material and place the elastic region immediately below the crater (38, 15). Riney has published a visco-plastic solution, but the solution time is too short to reveal the extent of the plastic region (30). His solution was run only 10 time cycles, and the impacting body entered only half way into the target. The elastic-plastic solution of these low velocity impacts may be compared with experiment. A metallographic study of a crater which was supplied by Soully has been prepared. A picture of the crater was published by Sodek (33). The plastic region appears to be considerably thinner than is obtained from the solutions in Figures 21 and 25. More experimental work should be performed to accurately define the location and extent of the plastic

deformation region.

The comments and descriptions of these low velocity impacts also apply to the remaining impact solutions. The crater solutions for these solutions are shown as Figures 26 to 38. In each impact solution, the material behind the shock front, shortly after impact, is in a fluid state except for the last figure in each solution. These figures are 29, 33, and 38. A good illustration of the violent ejection of the fluid material from the crater lip is shown in Figures 27 and 28. A particularly large amount of ejecta is shown in Figure 37. The dashed line in this latter figure marks the boundary of the ejecta and the position at which the free surface of the crater will be after the material is ejected. The conditions to release the ejecta are presented in a following section on ejecta.

The last figure in each sequence shows the elastic and plastic regions. The final crater surface will lie at the shallower boundary of the plastic region because the melted material above this region will be forced out of the target.

The effects of the velocity and the density of the impacting body on the crater parameters is summarized in Table IV. The symbol R in Table IV indicates the radius of the impacting sphere.

Effect of Sphere Diameter on the Crater

In the previous section, the effects are summarized for the velocity and the density of the impacting body. One effect has not been examined, and that effect is the diameter of the impacting sphere. The concept of late stage equivalence, which is the foundation of several proposed scaling laws, is based on the assumption that the influence of

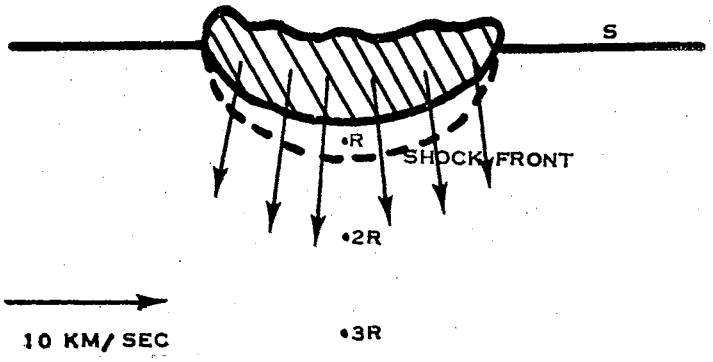

Figure 26. Crater at 2.6×10^{-10} second for sphere of density 2.0 gm/cc impacting at 20 km/sec.

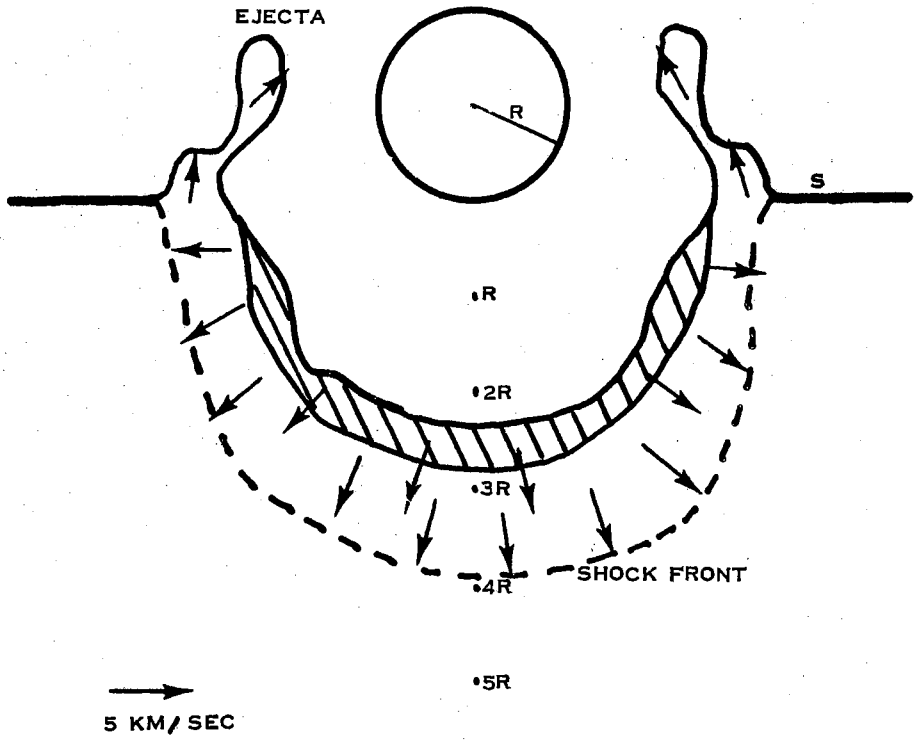

Figure 27. Crater at 1.3×10^{-9} second for sphere of density 2.0 gm/cc impacting at 20 km/sec.

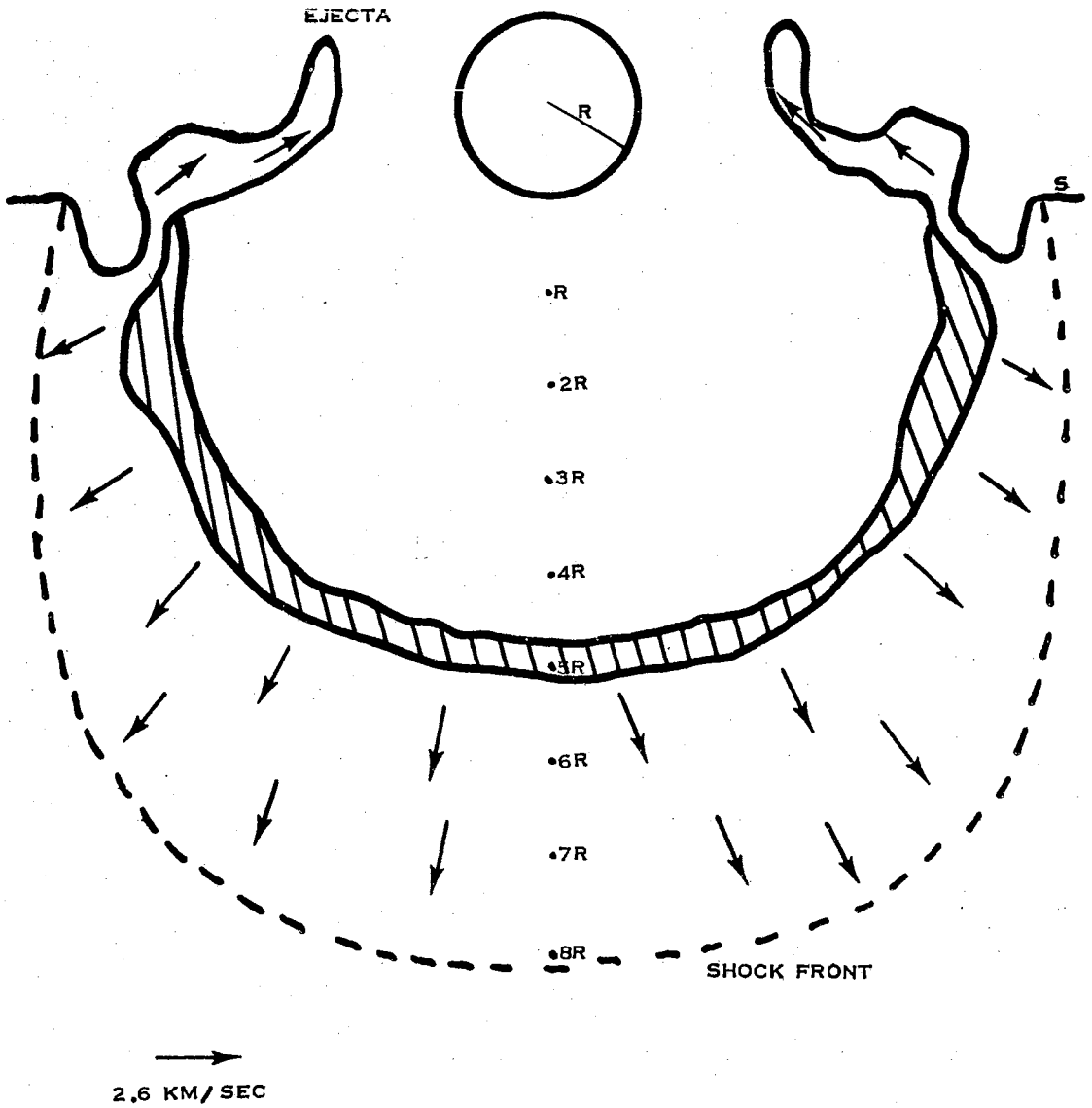

Figure 28. Crater at 3.6×10^{-9} second for sphere of density 2.0 gm/cc impacting at 20 km/sec.

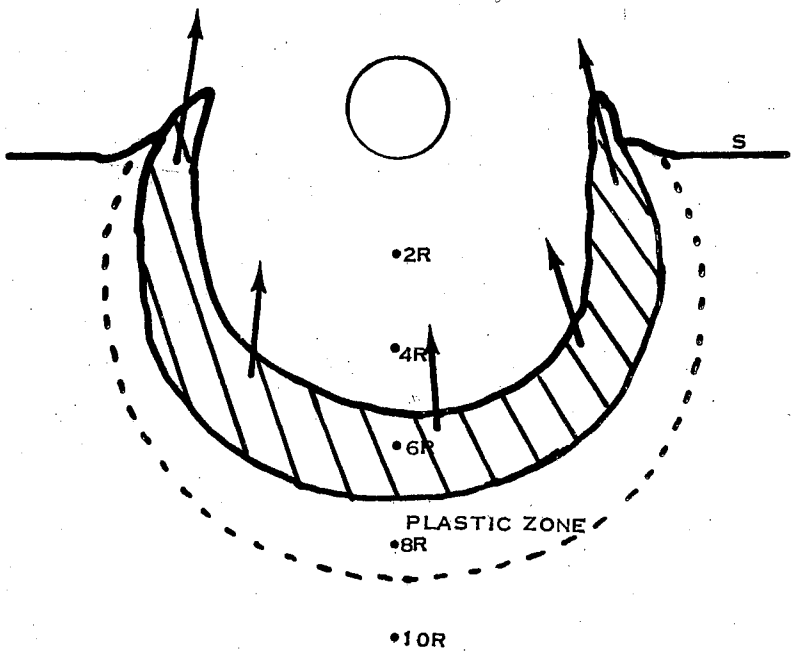

0.1 KM/SEC

Figure 29. Crater at 6.5×10^{-9} second for sphere of density 2.0 gm/cc impacting at 20 km/sec.

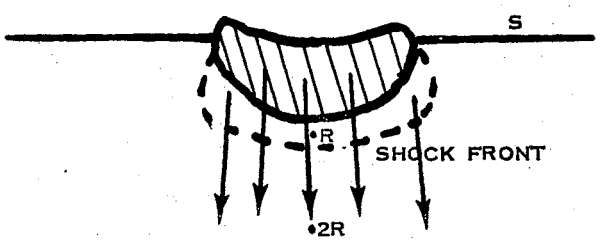

Figure 30. Crater at 4.0×10^{-10} second for sphere of density 0.5 gm/cc impacting at 20 km/sec.

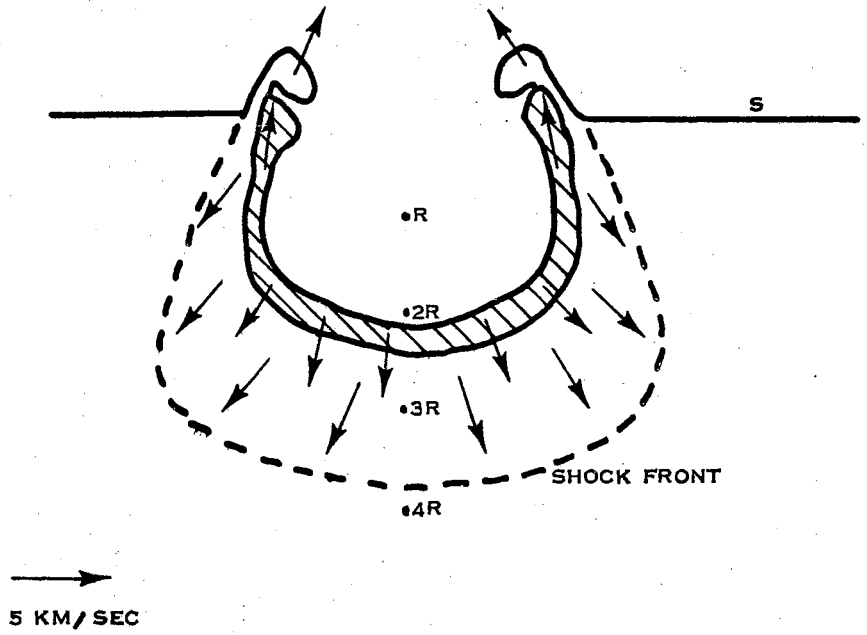

Figure 31. Crater at 1.1×10^{-9} second for sphere of density 0.5 gm/cc impacting at 20 km/sec.

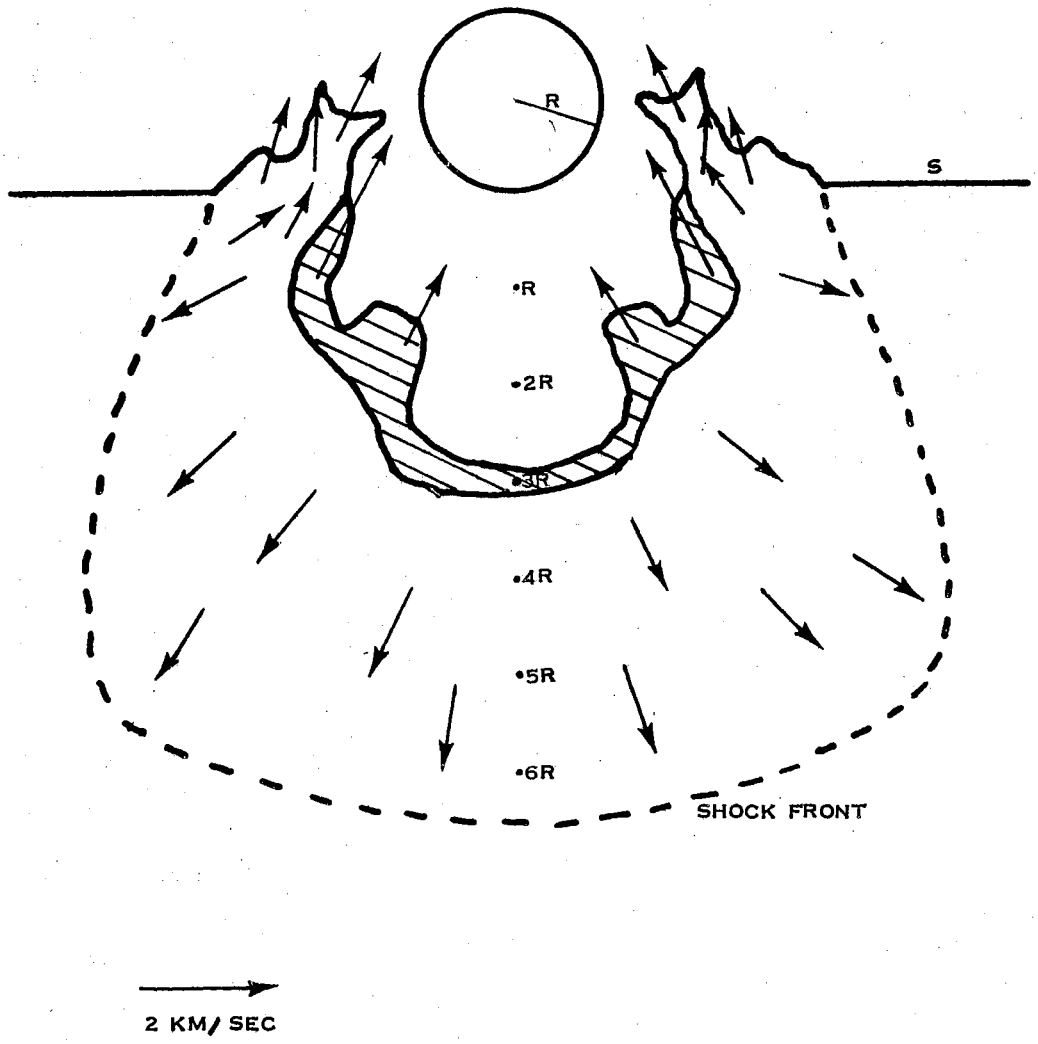

Figure 32. Crater at 4.9×10^{-9} second for sphere of density 0.5 gm/cc impacting at 20 km/sec.

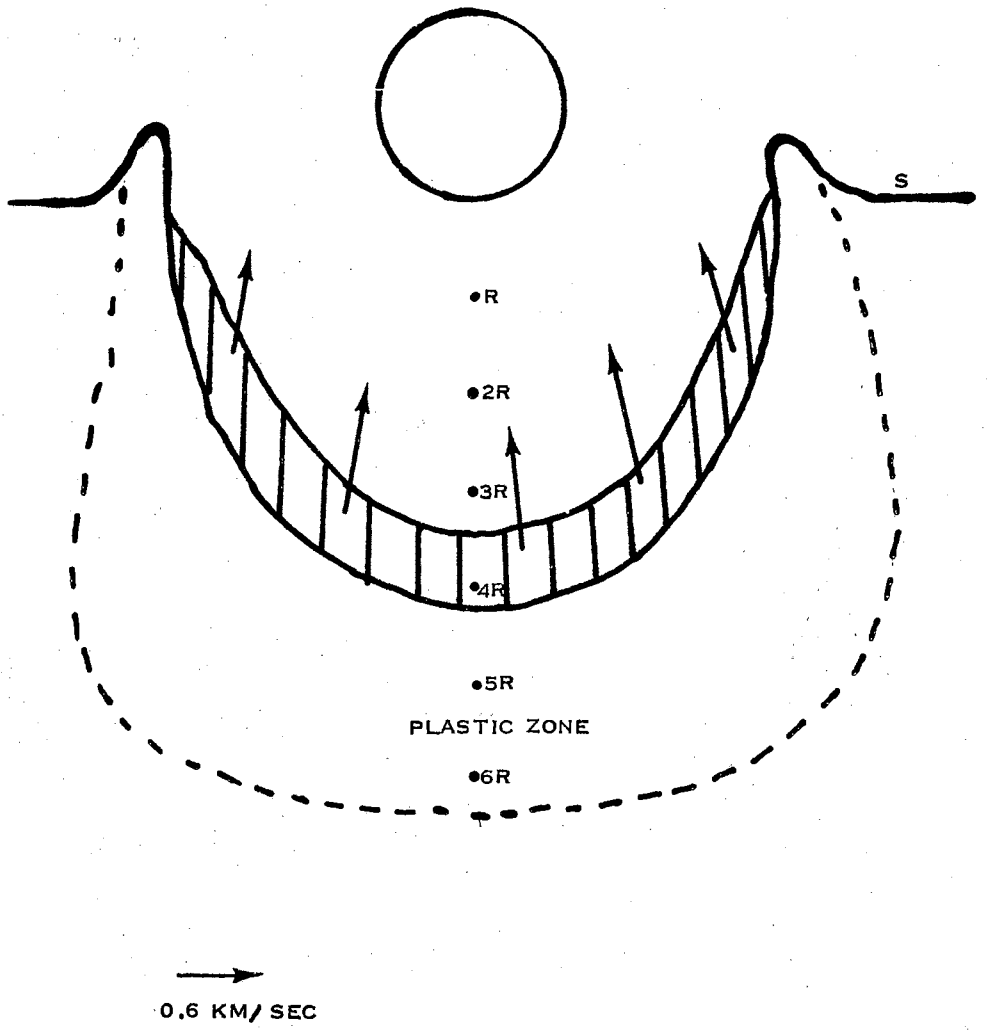

Figure 33. Crater at 6.3×10^{-9} second for sphere of density 0.5 gm/cc impacting at 20 km/sec.

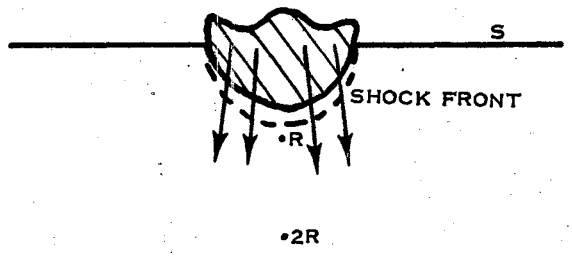

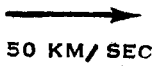

Figure 34. Crater at 1.2×10^{-10} second for sphere of density 0.5 gm/cc impacting at 72 km/sec.

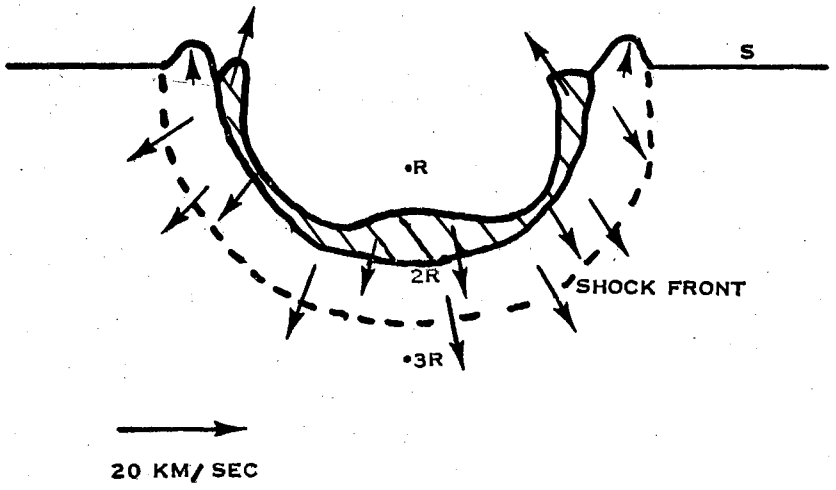

Figure 35. Crater at 9.3×10^{-10} second for sphere of density 0.5 gm/cc impacting at 72 km/sec.

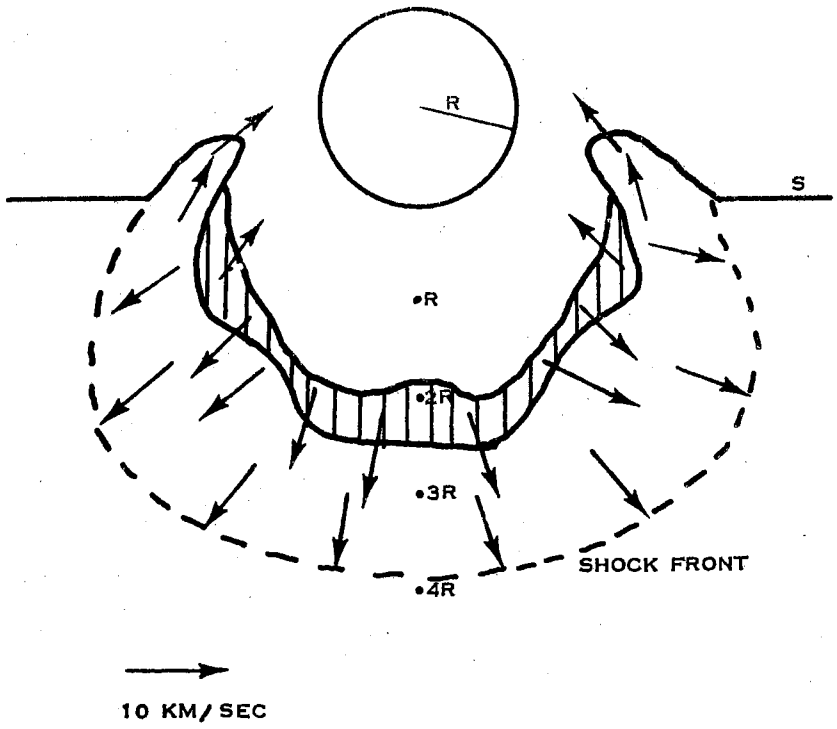

Figure 36. Crater at 1.5×10^{-9} second for sphere of density 0.5 gm/cc impacting at 72 km/sec.

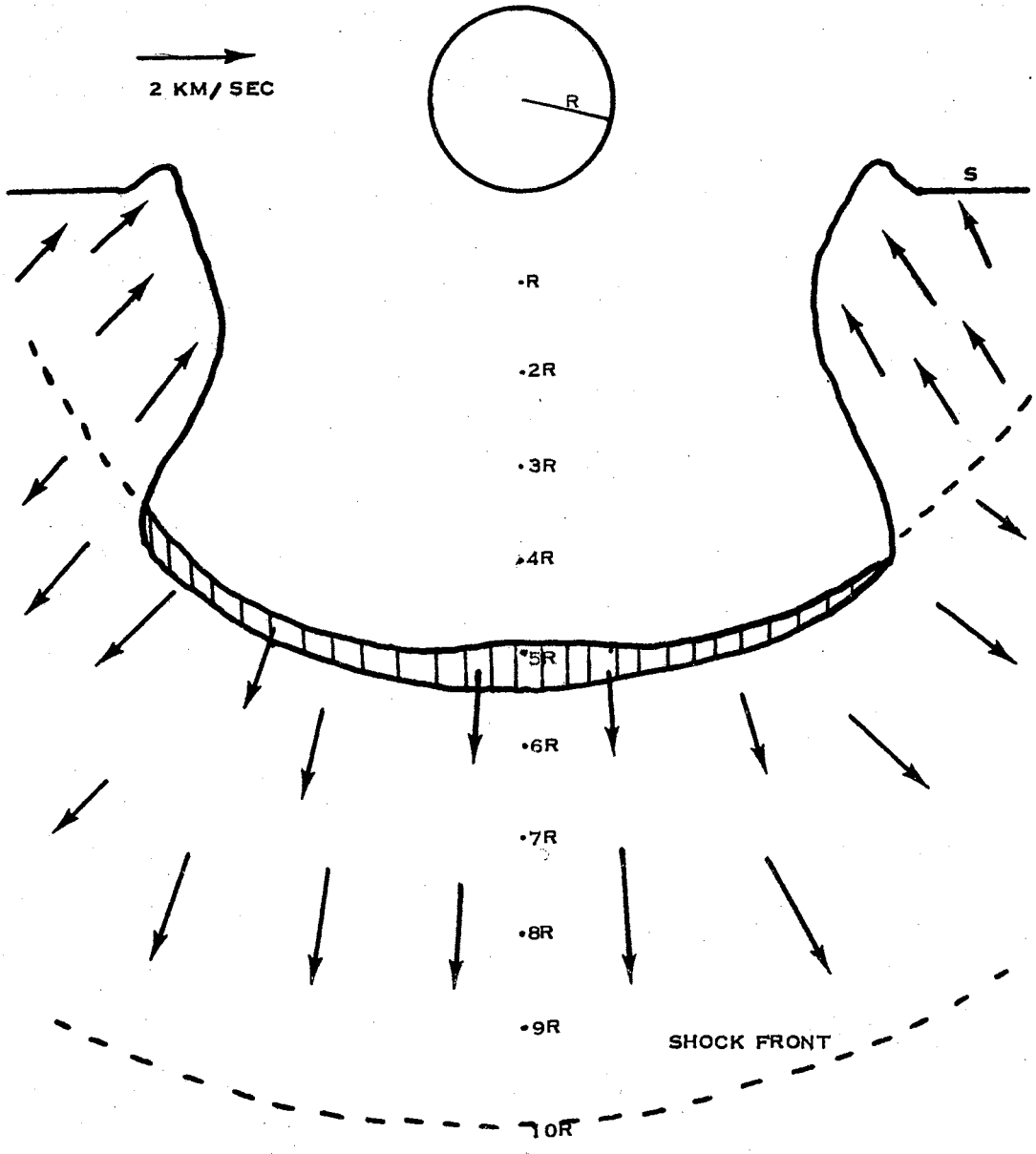

Figure 37. Crater at 5.9×10^{-9} second for sphere of density 0.5 gm/cc impacting at 72 km/sec.

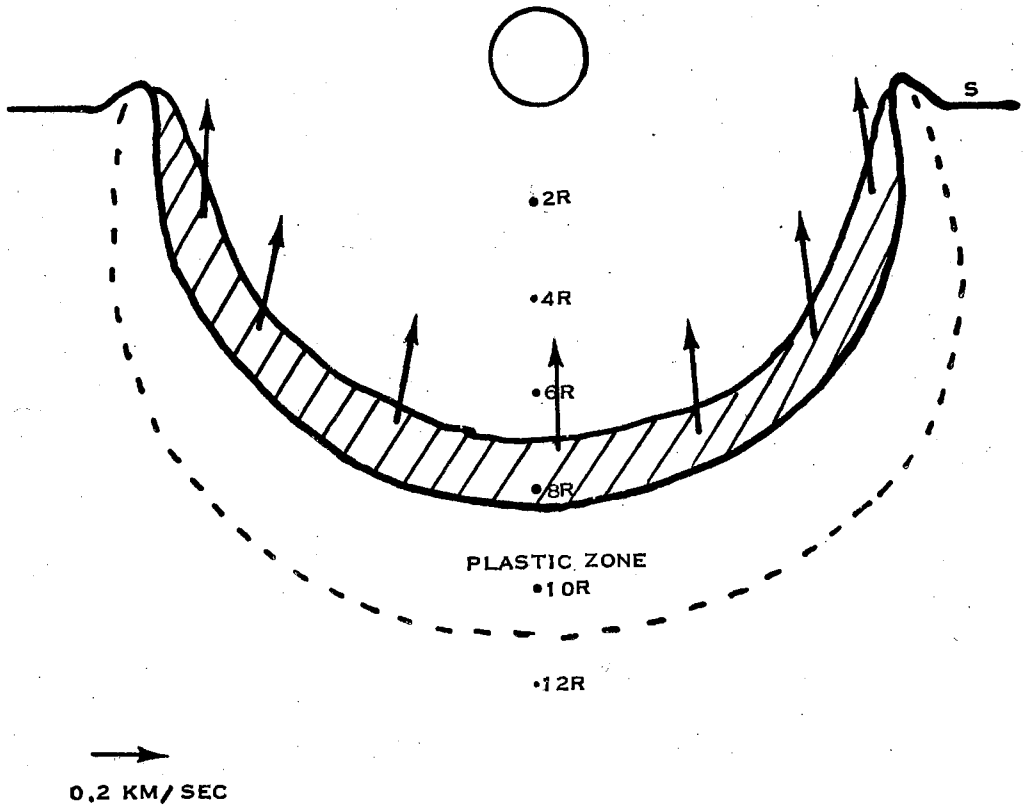

Figure 38. Crater at 1.2×10^{-8} second for sphere of density 0.5 gm/cc impacting at 72 km/sec.

material viscosity and strength effects on crater dimensions scales with size. The verification of this assumption is virtually impossible by experiment. This statement follows since late stage equivalence is asserted to be valid only at impact velocities above 2C, where C is the velocity of sound in the target. Experimental data is difficult to obtain for most metals at such velocities.

TABLE IV

CRATER PARAMETERS RESULTING FROM IMPACTS

Velocity	Density	Depth of Crater	Width of Plastic Zone
6.25 km/sec	2.0 gm/sec	2.1 R	R
7.5 km/sec	2.0 gm/sec	3.3 R	1.5 R
20.0 km/sec	2.0 gm/sec	7.1 R	1.8 R
20.0 km/sec	0.5 gm/sec	4.3 R	2.1 R
72.0 km/sec	0.5 gm/sec	8.3 R	2.4 R

Several research groups have proposed simple scaling laws. Riney and Heyda state that the flow fields are identical for bodies of different size provided the kinetic energy of the impacting body is held constant, and that the density of the impacting body has no effect on the late stages of the impact process if the mass of the body does not change (31). Their scaling law proposes that the crater depth is proportional to the 2/3 power of the impact velocity. Bjork's recent paper refutes the idea that a simple, density scaling law of the form $K(\rho_p/\rho_T)^{\beta}$ can suitably account for the dependence of penetration on density (38). The work of other groups could be cited, but their scaling laws would only be another form of the equation $k_i(V/C)^{2/3}$

or $K_i(\rho_p/\rho_T)^{\beta_i}$. These scaling laws are based on the concept that the mechanical coupling between the projectile and the target arises only through the agency of a shock. The scaling assumptions do not account for the increase in input momentum from the effect of the ejected material.

The fundamental fact, on which the investigators in this area agree, is that there is some type of power dependence between crater penetration and impact velocity. If this assumption is true, then the crater created by a sphere of radius 1.5R should be 1.5 times deeper than a crater created by a sphere of radius R. To test this assumption, a solution was sought for a sphere of density 0.5 gram/centimeter and a radius 11.7×10^{-4} centimeter which impacted at 20 kilometers per second. The crater solutions are shown in Figures 39 to 42. These solutions should be compared with Figures 30 to 33, which are the solutions for a sphere that is identical except for a radius of 7.8×10^{-4} centimeter.

The first figure in the series was chosen to illustrate the shock wave in the rock sphere. This wave is present in the preceding impacts but was not illustrated. It never moves much farther away from the original aluminum surface than the position in Figure 39.

The development of the crater does not differ from any which has been reported. The last stage of the crater shows an interesting picture of the ejecta. The previous solutions show a thin layer of rock vapor lining the crater. In Figure 42, this rock lining has been broken, and a considerable quantity of aluminum vapor is ejecting through this rupture in the rock lining.

The comparison of the parameters of this crater with the crater

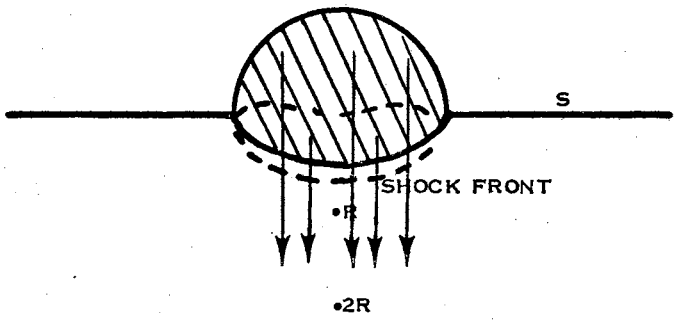

Figure 39. Crater at 4.5×10^{-10} second for sphere of density 0.5 gm/cc impacting at 20 km/sec.

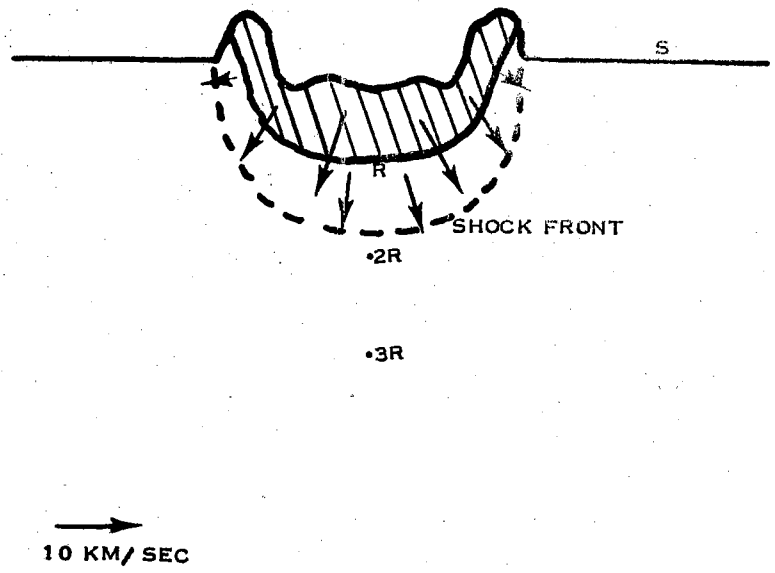

Figure 40. Crater at 2.5×10^{-9} second for sphere of density 0.5 gm/cc impacting at 20 km/sec.

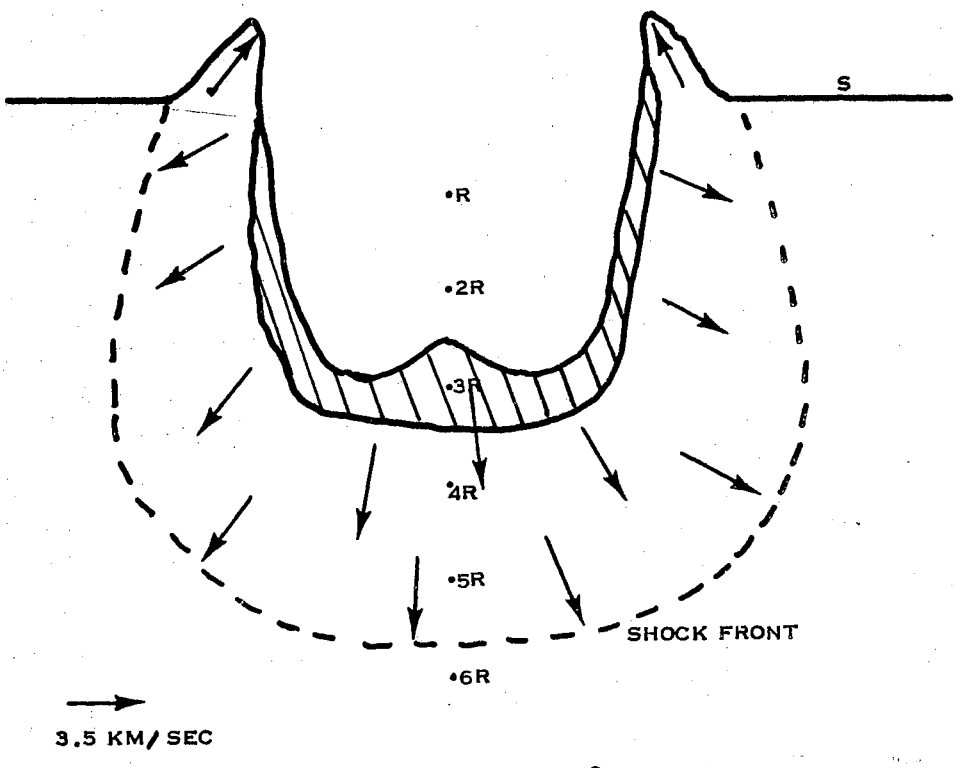

Figure 41. Crater at 1.0×10^{-8} second for sphere of density 0.5 gm/cc impacting at 20 km/sec.

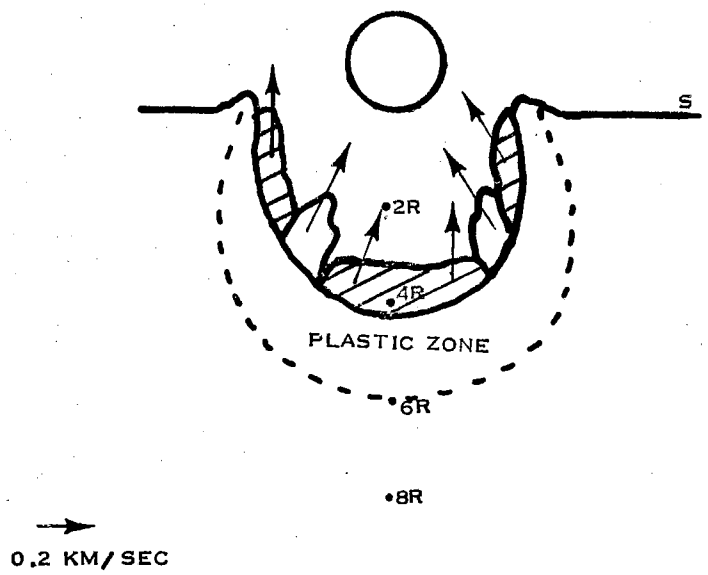

Figure 42. Crater at 1.9×10^{-8} second for sphere of density 0.5 gm/cc impacting at 20 km/sec.

from the impact of the smaller sphere is summarized in Table V. All of the crater parameters agree quite well; therefore, the crater size scales linearly or practically lineraly with projectile size in this instance. More solutions are required to prove that the dependence is linear when the diameter is varied further.

TABLE V

CRATER PARAMETERS CREATED BY SPHERES OF RADIUS R AND RADIUS 3/2 R

Radius of Sphere	Depth of Crater	Width of Plastic Zone
R	4.3 R	2.1 R
3/2 R	4.2 R	1.8 R

Pressure Profiles

Certain features of the impact process are best illustrated by examining the distribution of pressure behind the shock front. The pressure profiles emphasize the violent churning and mixing of the highly compressed material, and they also show the existence of a dual wave structure in the plastic zone. Neither of these phenomena are revealed in detail in the crater diagrams. The pressure profiles created by the impacts are shown in Figures 43 to 66. The letter, S, in the figures indicates the original position of the aluminum surface; the letter R represents a distance equal to one sphere radius.

The profiles are plotted for a fixed value of θ which is $7\frac{1}{2}^{o}$ away from the Z axis. The churning and mixing of the shocked material is indicated in these figures by the change in amplitude of the pressure profiles. Specific examples are shown in Figures 46, 48, 53, 61, 65,

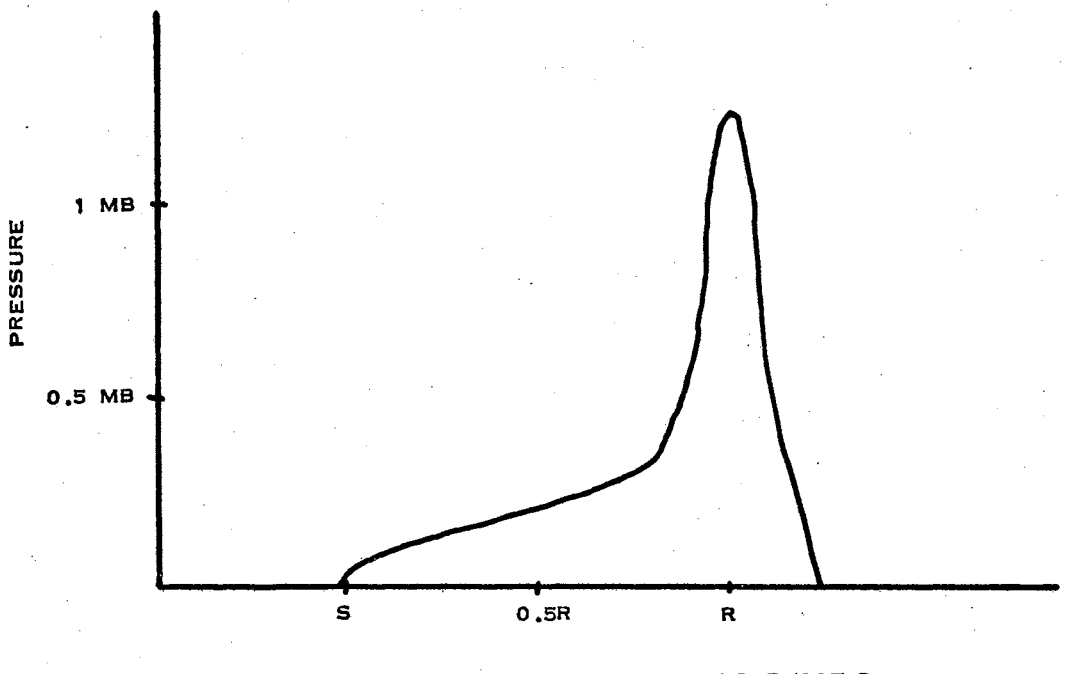

Figure 43. Pressure profile at 7.9×10^{-10} second for sphere of density 2.0 gm/cc impacting at 6.25 km/sec.

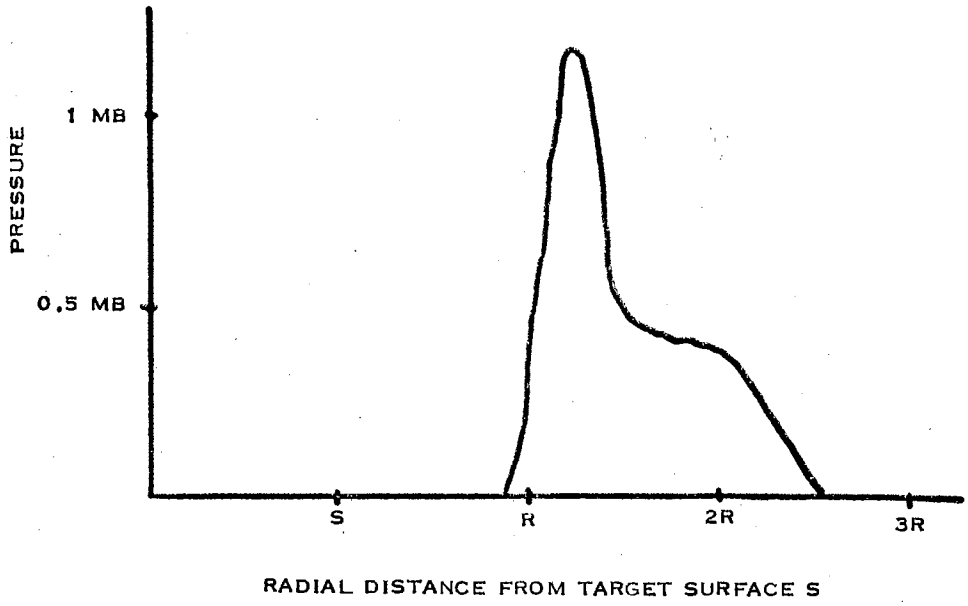

Figure 14. Pressure profile at 1.6×10^{-9} second for sphere of density 2.0 gm/cc impacting at 6.25 km/sec.

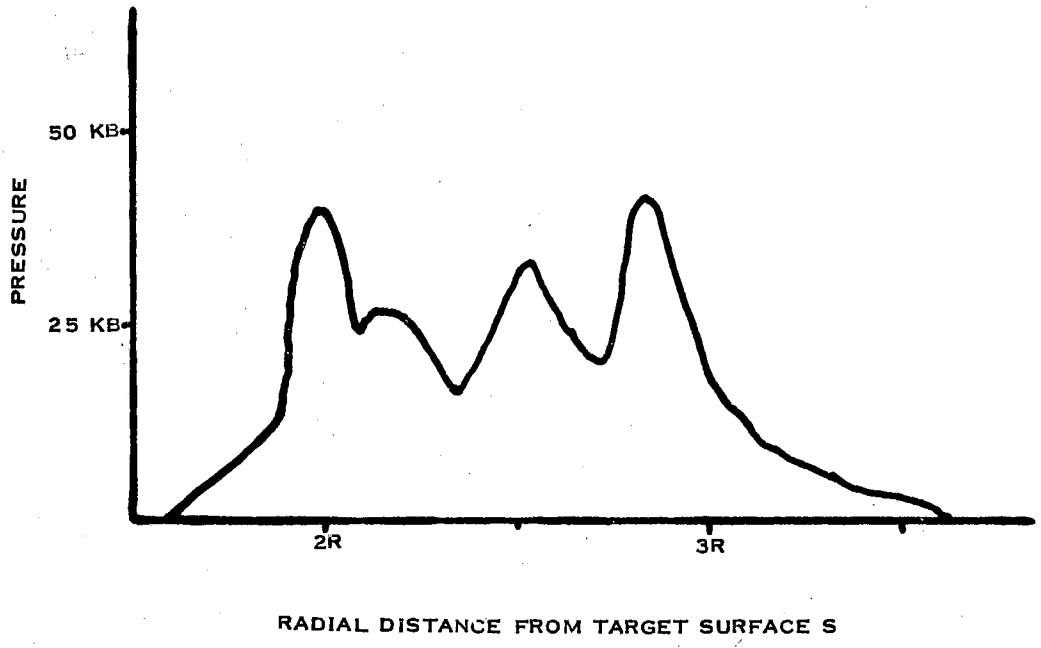

Figure 45. Pressure profile at 2.5×10^{-9} second for sphere of density 2.0 gm/cc impacting at 6.25 km/sec.

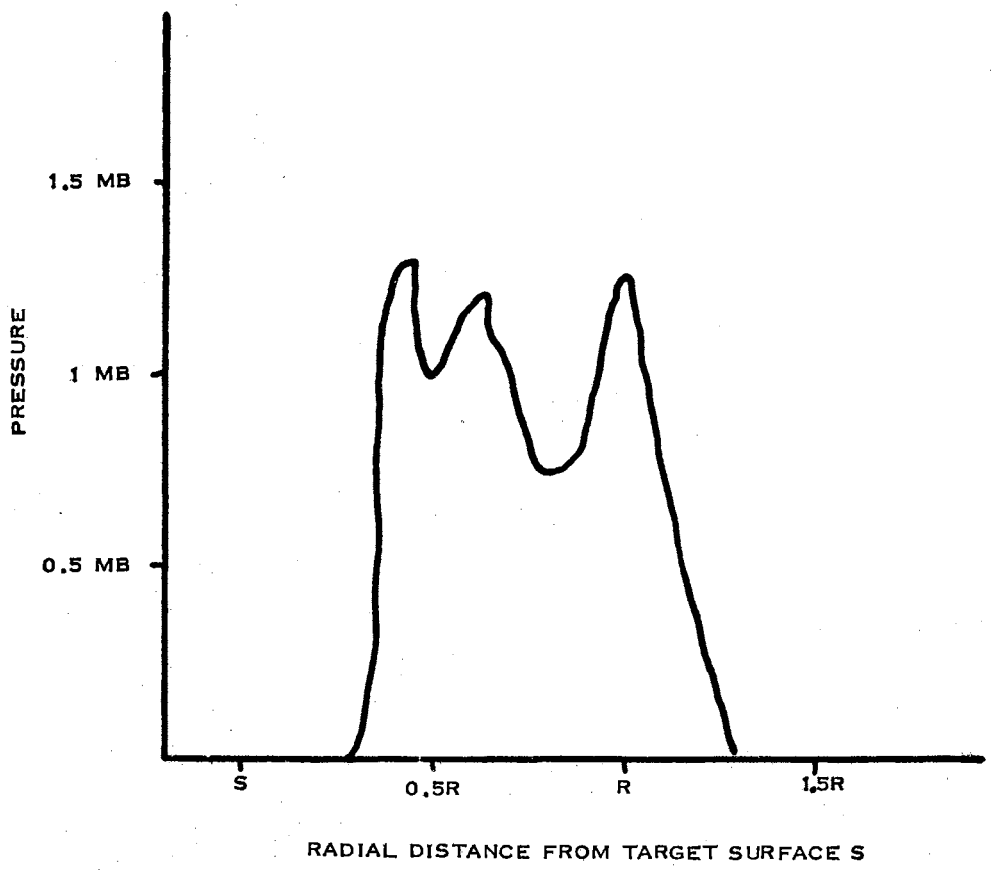

Figure 46. Pressure profile at 6.5×10^{-10} second for sphere of density 2.0 gm/cc impacting at 7.5 km/sec.

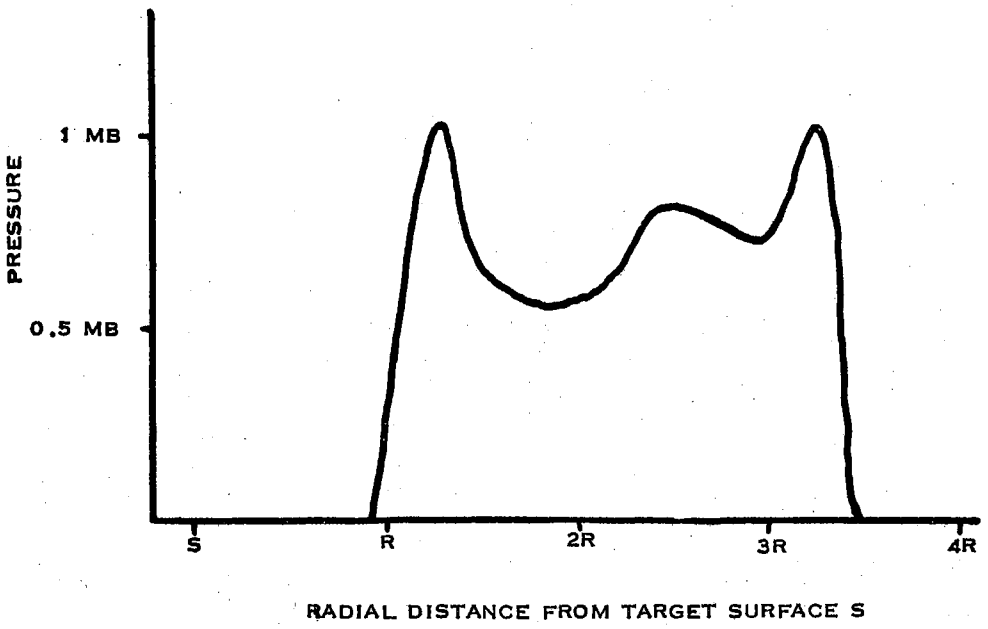

Figure 47. Pressure profile at 1.9×10^{-9} second for sphere of density 2.0 gm/cc impacting at 7.5 km/sec.

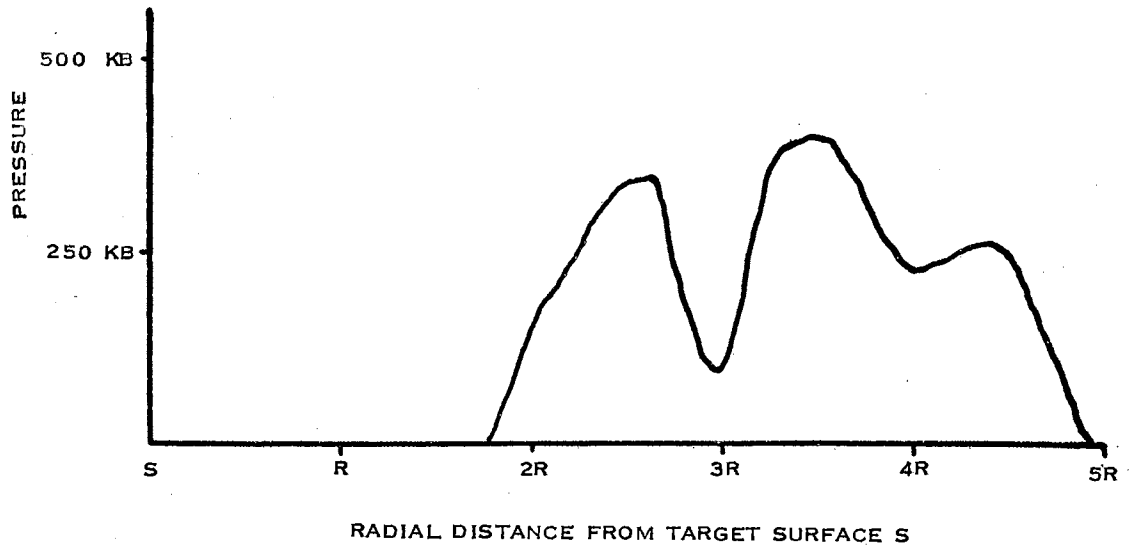

Figure 48. Pressure profile at 3.0×10^{-9} second for sphere of density 2.0 gm/cc impacting at 7.5 km/sec.

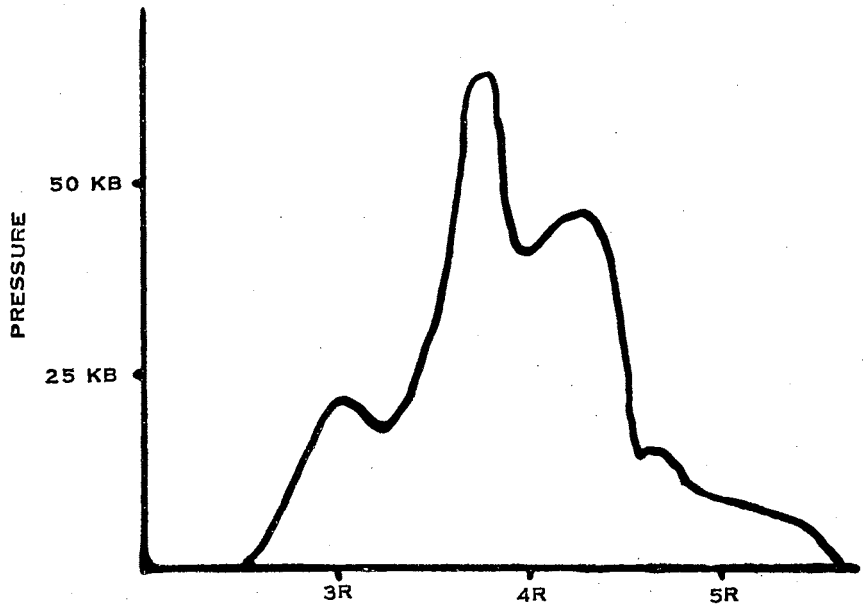

Figure 49. Pressure profile at 4.7×10^{-9} second for sphere of density 2.0 gm/cc impacting at 7.5 km/sec.

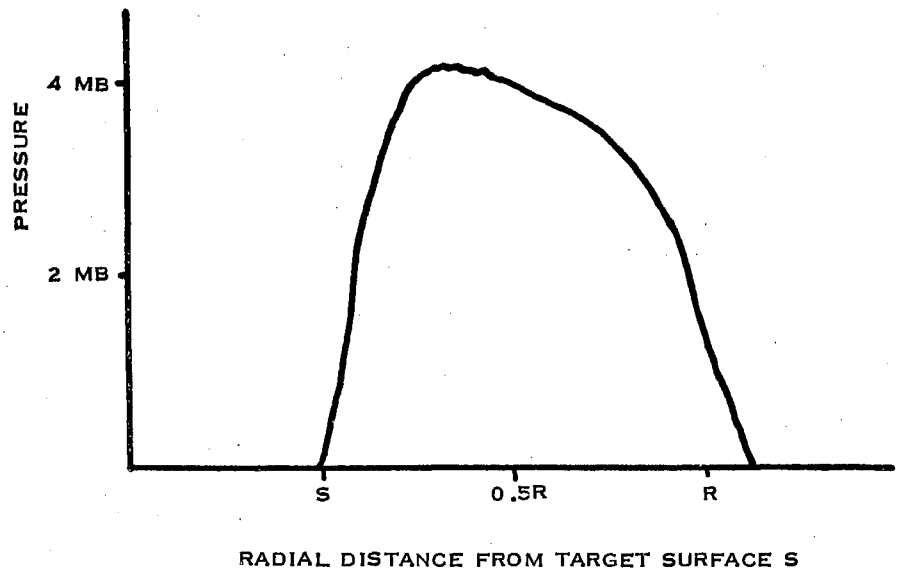

Figure 50. Pressure profile at 2.6×10^{-10} second for sphere of density 2.0 gm/cc impacting at 20 km/sec.

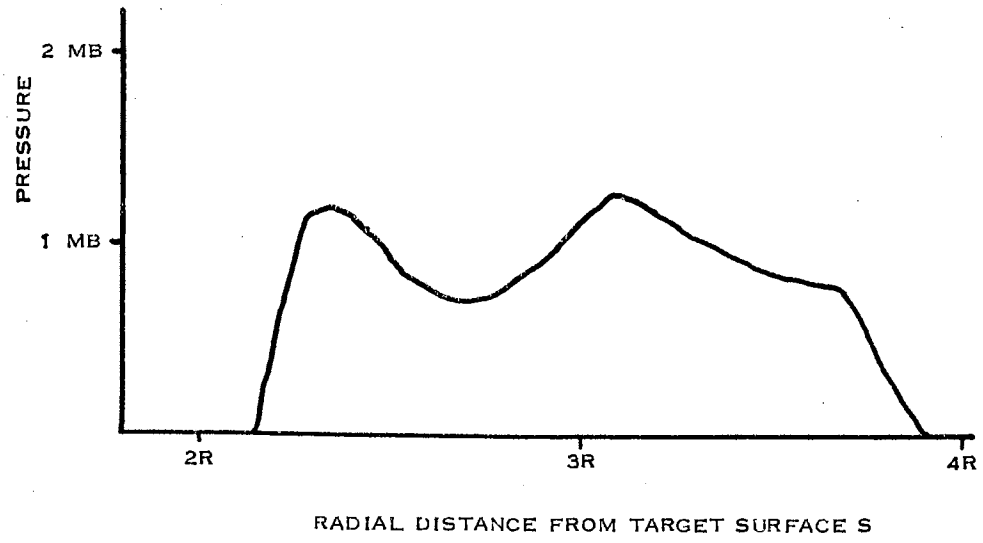

Figure 51. Pressure profile at 1.3×10^{-9} second for sphere of density 2.0 gm/cc impacting at 20 km/sec.

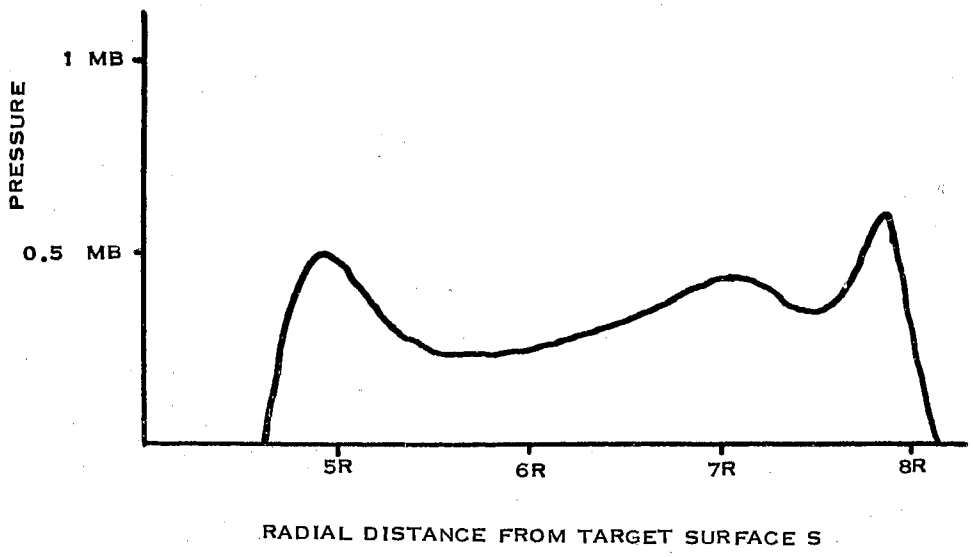

Figure 52. Pressure profile at 3.6×10^{-9} second for sphere of density 2.0 gm/cc impacting at 20 km/sec.

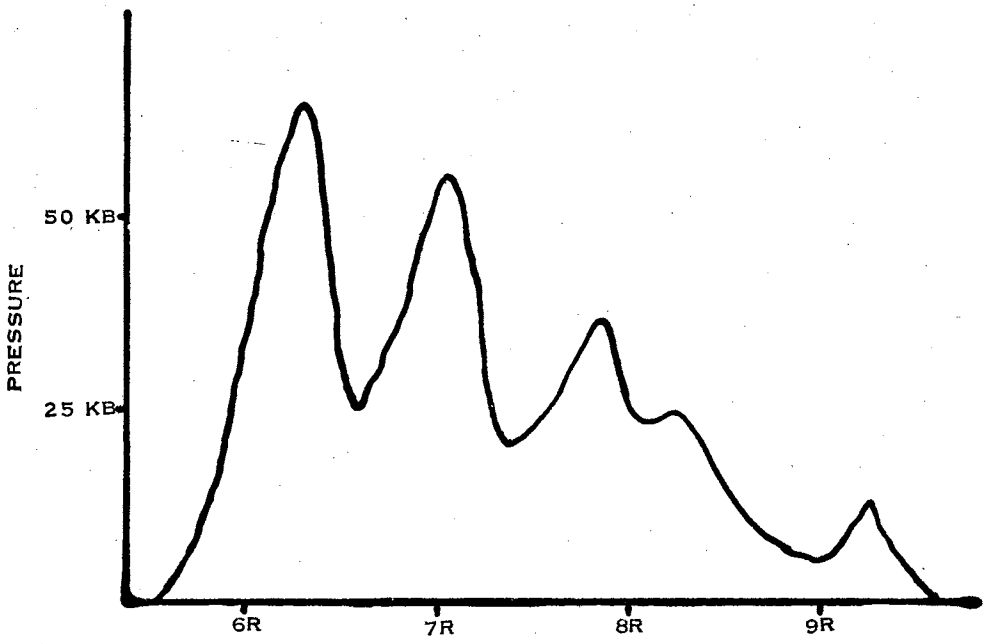

Figure 53. Pressure profile at 6.5×10^{-9} second for sphere of density 2.0 gm/cc impacting at 20 km/sec.

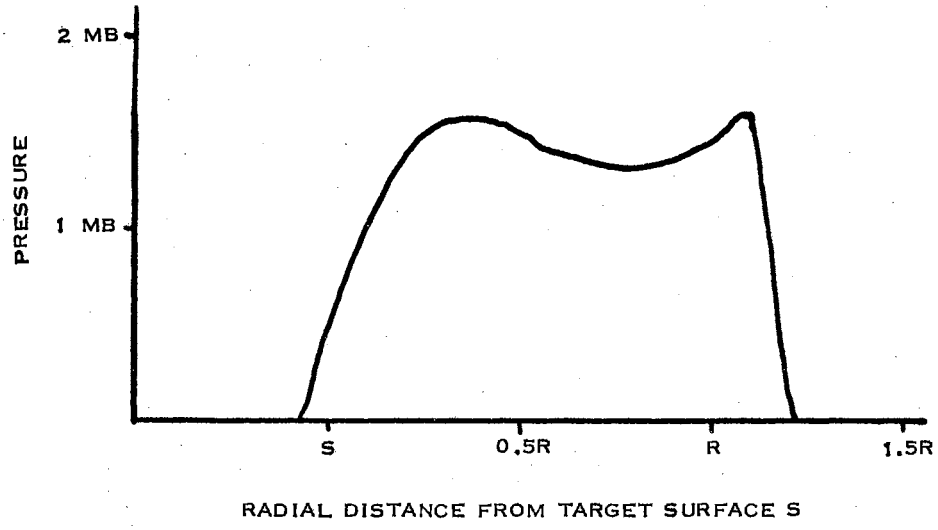

Figure 54. Pressure profile at 4.0×10^{-10} second for sphere of density 0.5 gm/cc impacting at 20 km/sec.

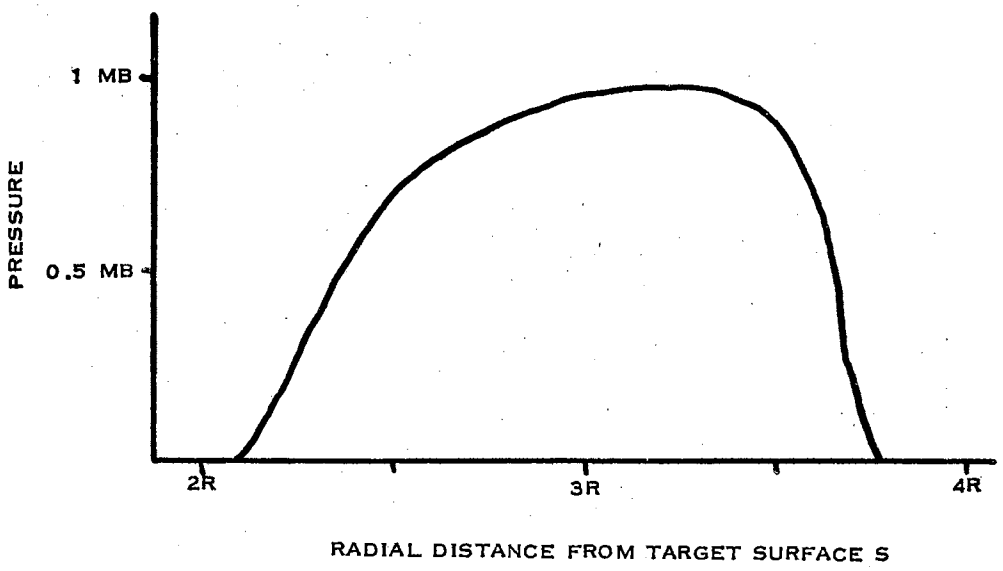

Figure 55. Pressure profile at 1.1×10^{-9} second for sphere of density 0.5 gm/cc impacting at 20 km/sec.

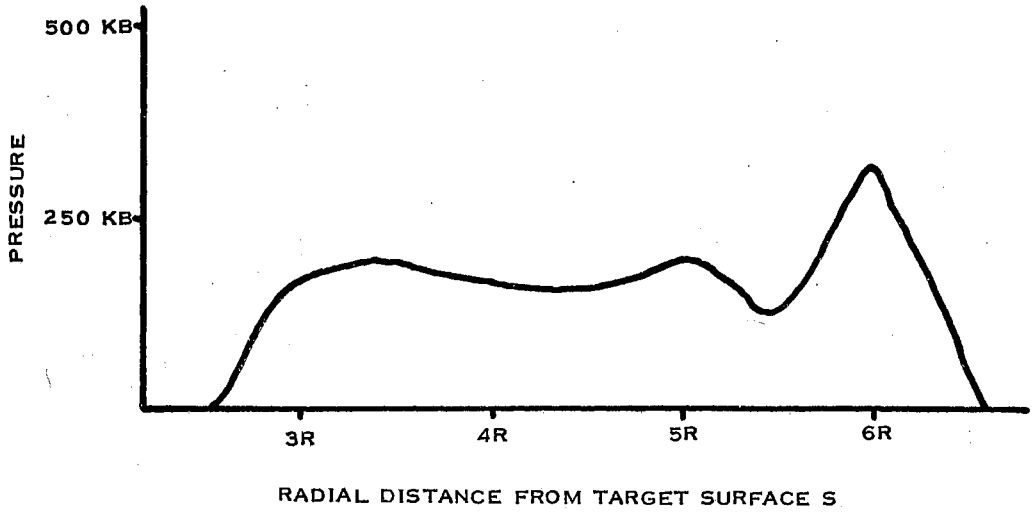

Figure 56. Pressure profile at 4.9×10^{-9} second for sphere of density 0.5 gm/cc impacting at 20 km/sec.

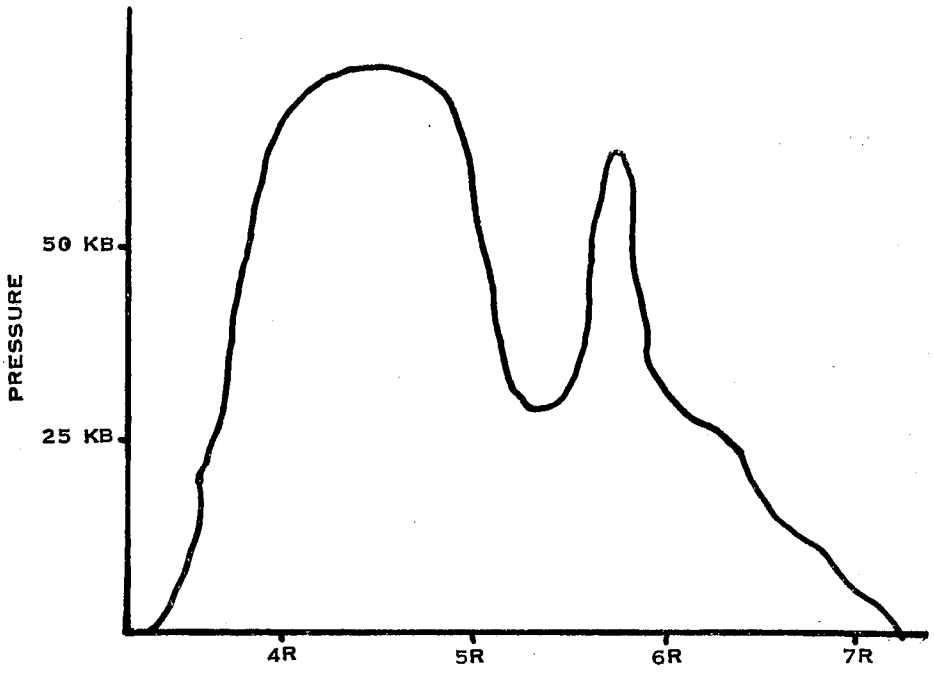

Figure 57. Pressure profile at 6.3×10^{-9} second for sphere of density 0.5 gm/cc impacting at 20 km/sec.

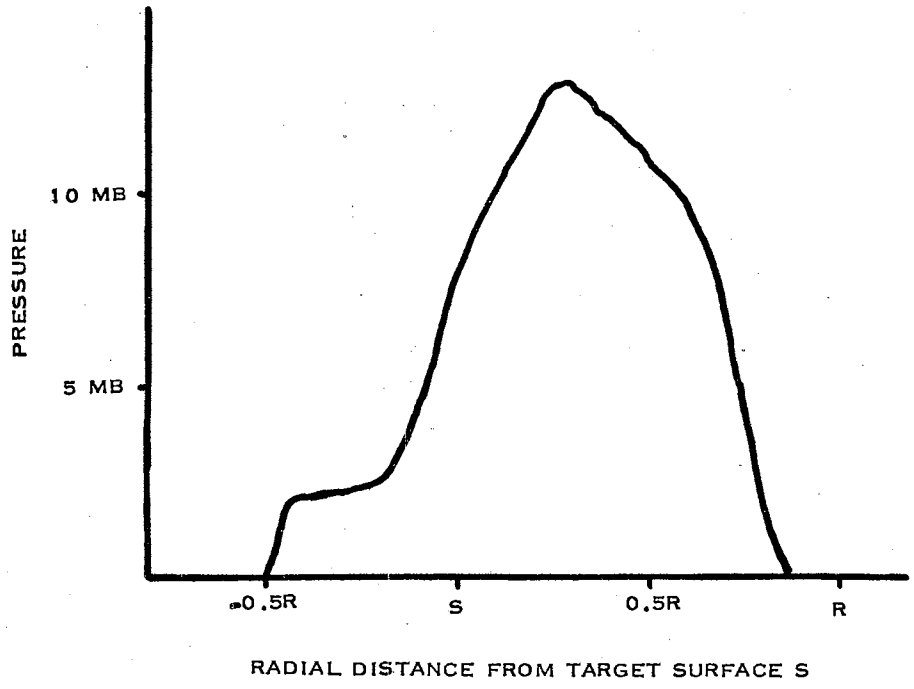

Figure 58. Pressure profile at 1.2×10^{-10} second for sphere of density 0.5 gm/cc impacting at 72 km/sec.

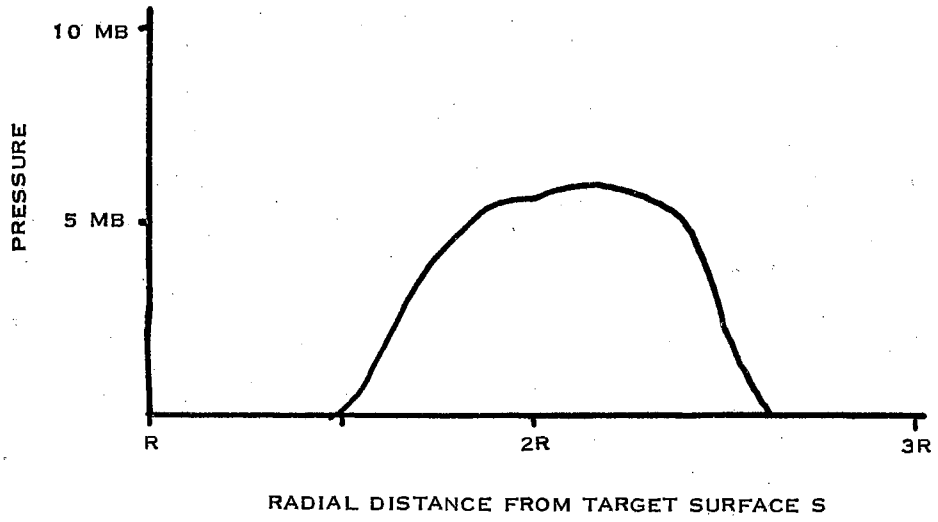

Figure 59. Pressure profile at 9.3×10^{-10} second for sphere of density 0.5 gm/cc impacting at 72 km/sec.

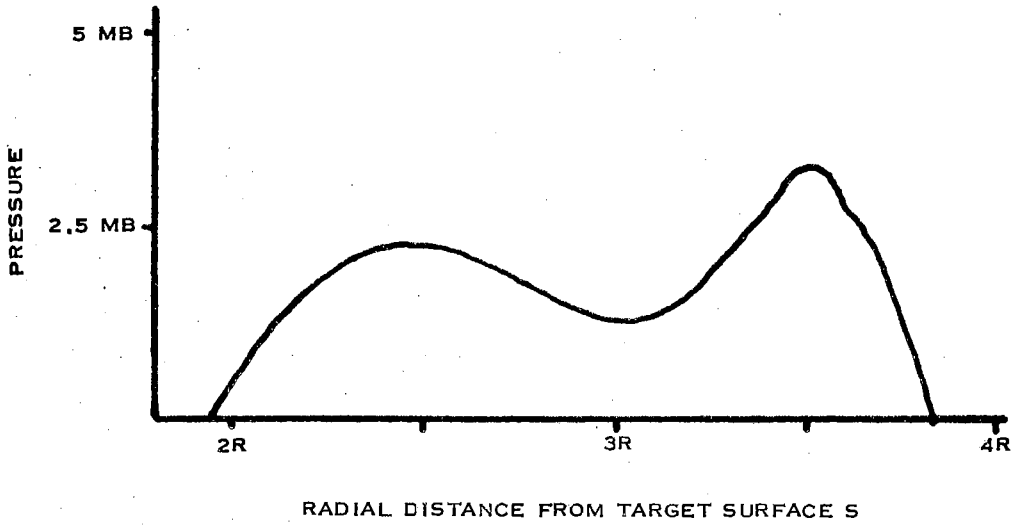

Figure 60. Pressure profile at 1.5×10^{-9} second for sphere of density 0.5 gm/cc impacting at 72 km/sec.

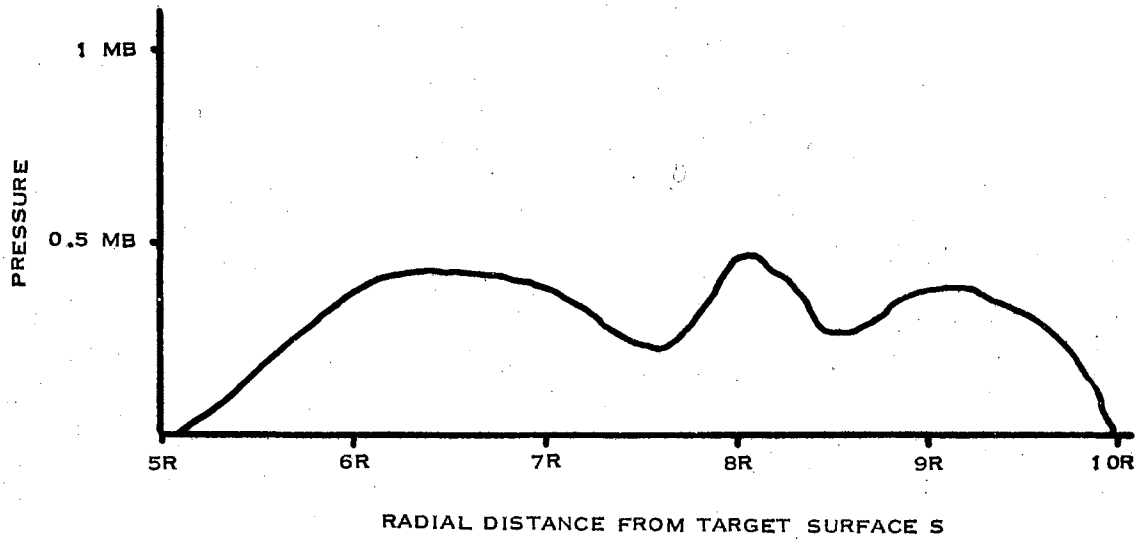

Figure 61. Pressure profile at 5.9×10^{-9} second for sphere of density 0.5 gm/cc impacting at 72 km/sec.

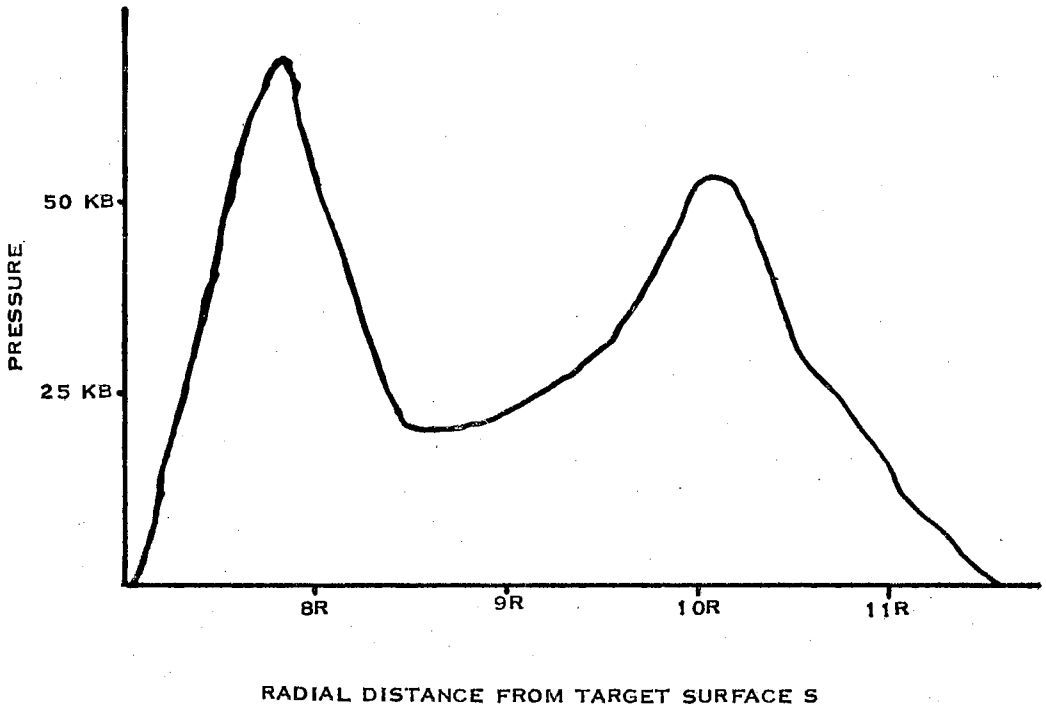

Figure 62. Pressure profile at 1.2×10^{-8} second for sphere of density 0.5 gm/cc impacting at 72 km/sec.

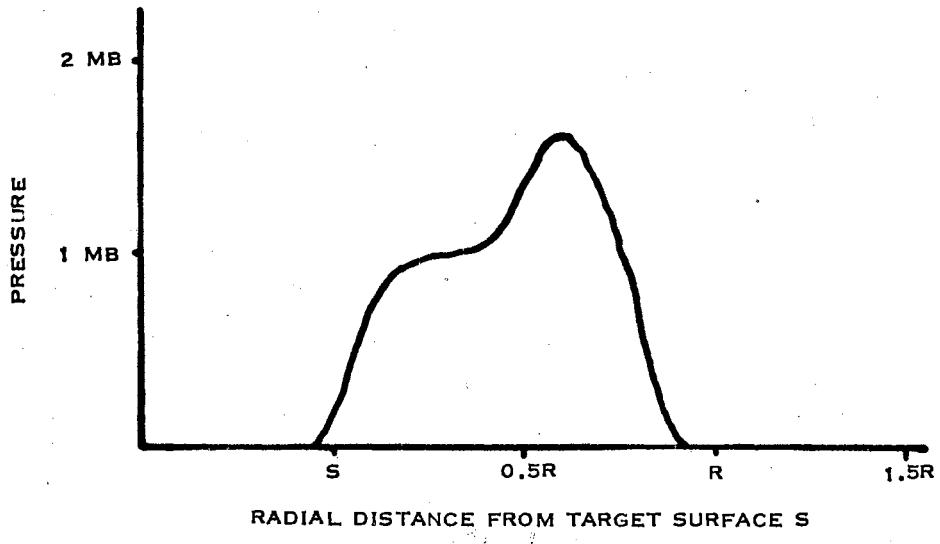

Figure 63. Pressure profile at 4.5×10^{-10} second for sphere of density 0.5 gm/cc impacting at 20 km/sec.

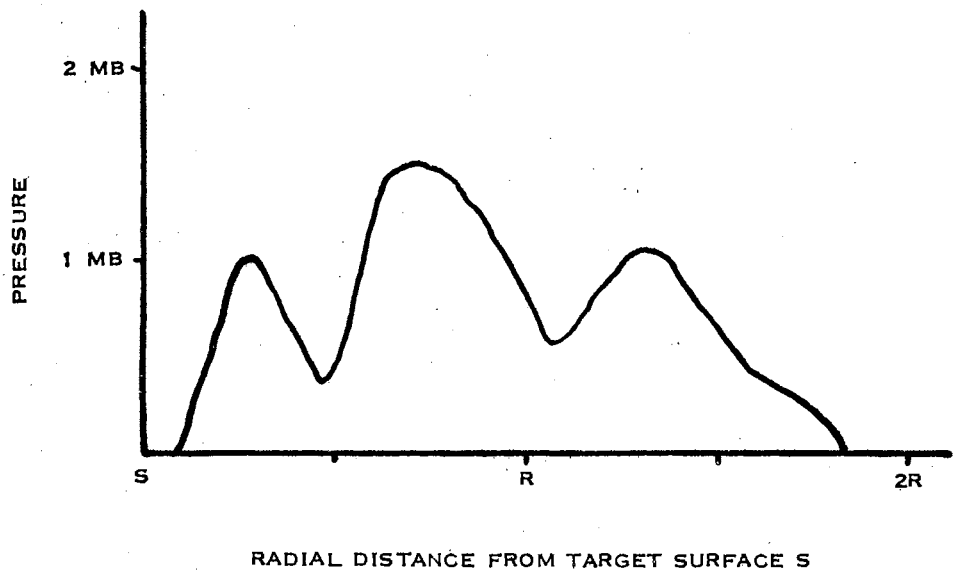

Figure 64. Pressure profile at 2.5×10^{-9} second for sphere of density 0.5 gm/cc impacting at 20 km/sec.

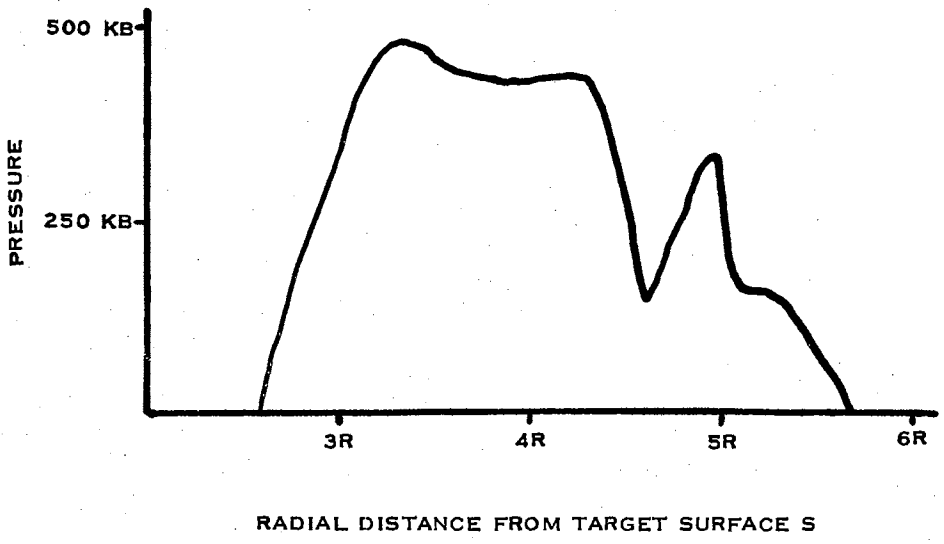

Figure 65. Pressure profile at 1.0×10^{-8} second for sphere of density 0.5 gm/cc impacting at 20 km/sec.

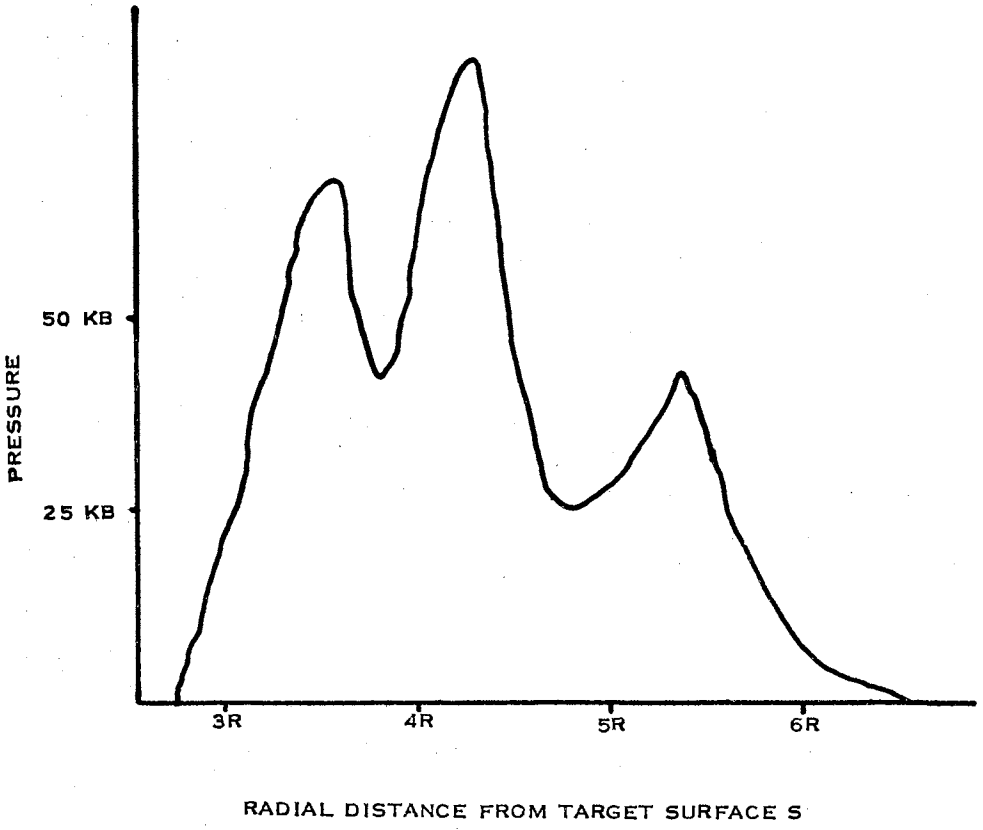

Figure 66. Pressure profile at 1.9×10^{-8} second for sphere of density 0.5 gm/cc impacting at 20 km/sec.

and 66. A certain amount of oscillation results in any numerical solution, but these oscillations are too extreme to believe that they are completely a result of numerical techniques. The presence of the pressure oscillations in the solution, independent of the computer characteristics, was demonstrated by computing a second solution with a different size of cell. The pressure amplitudes in the second solution were roughly the same as in the first solution. Kinslow has made excellent photographs of an impact at 21,000 feet per second, and these photographs show rough edges around the shocked material (15). These non-symmetrical extrusions imply the existence of vortices and swirls in the material which would result from such oscillations. Kinslow states that the spalling surface moves eratically after the shock has reached it. This behavior also indicates that there must be strong oscillations in the pressure wave that is incident on the surface. The data collected from atomic bomb blasts reveals that swirls and eruptive outbreaks occur inside the blast sphere. This, too, implies that there are strong pressure concentrations at certain spots in a highly shocked region. A close examination of the figures will show that the oscillations move to and fro and are not stationary.

It is well known that a shock wave exists as a single wave when the peak pressure is of the order of several megabars. After the shock pressure decreases to 137 kilobars (according to previous assumptions), there is a transition from the fluid state to the plastic state. At this position, the shock ceases to exist as a single wave. The shock develops the dual wave structure that is illustrated in Figure 67.

There is a precursor wave that raises the pressure to the elastic limit of the material, and behind this wave is a stronger wave that

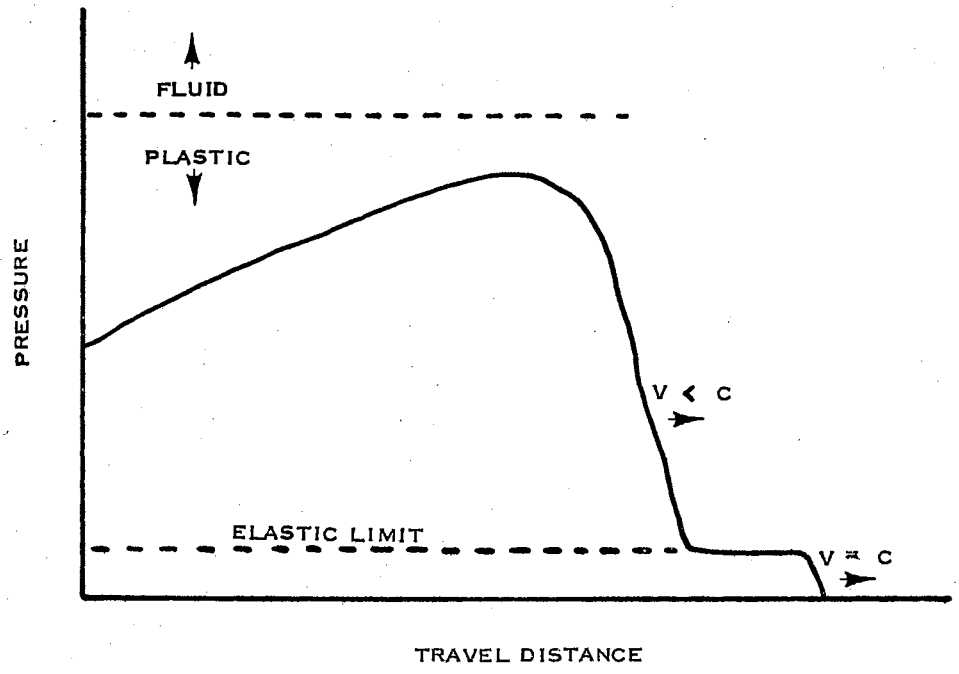

FIGURE 67 – DUAL WAVE STRUCTURE IN PLASTIC REGION

raises the pressure to its peak value. The first wave is called the elastic precursor, and it travels with the velocity of sound in the medium. The trailing wave is called the plastic wave, and its velocity of propagation is less than the speed of sound. As the shock continues onward, the plastic wave is attenuated until its peak decreases to the elastic limit. The shock wave now consists of a single acoustic wave. This elastic-plastic wave is shown in Figures 45, 49, 53, 57, 62, and 66.

Calculation of the Momentum and Energy of the Ejecta

An important part of this solution is an estimation of the momentum and energy carried away by the ejected target material. The shock process in any cell in the finite difference mesh may be described by consideration of the pressure cycle in the cell. A typical cycle is illustrated in Figure 68. As the shock moves through the cell, the pressure rises along the Hugoniot curve from A to B. After the shock front passes the cell, the pressure releases along the adiabat BCD. A question to be answered when the material returns to some point between C and D is: "Is the material fluid or solid?" If it is solid, then it cannot be ejected from the target; if it is fluid, it may be ejected provided the velocity components are such that the fluid would be carried away from the shocked region. The decision of whether the material is fluid or solid is made in the following manner:

1. Check the density, d, in each cell behind the shock front.
2. Calculate the ratio $R=d/d_o$ where d_o is the undisturbed density.

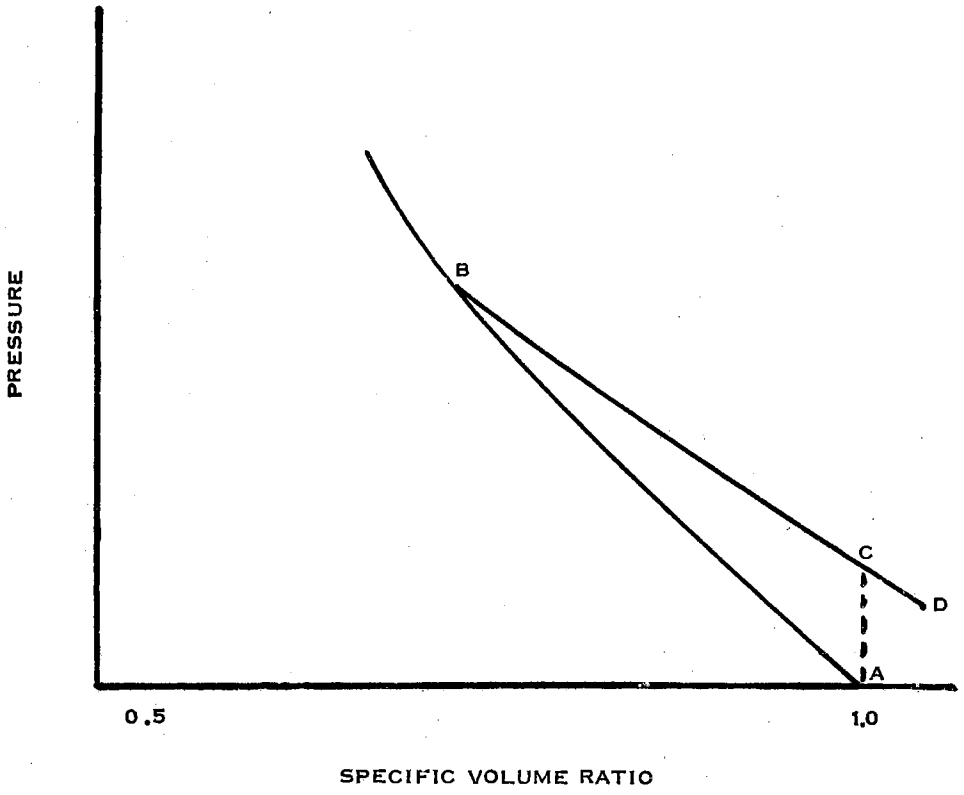

FIGURE 68 – PRESSURE CYCLE IN CELL

3. If $R > 1.0$, skip the ejecta calculation because the material has not released to point C.
4. If $R \leq 1.0$, check the internal energy, EIN, in the cell.
5. If EIN is less than the latent heat of fusion, skip the ejecta calculation because the material is a solid under tension and is not free to be ejected.
6. If EIN is greater than the latent heat of fusion, allow the material to be ejected since it is a fluid.

Whenever the material in a cell is ejected, the tag value of that cell is set equal to zero so that the computer program records that the material has left the cell. The energy and momentum in the cell are stored in the computer, and their values are printed when desired. A running total of these quantities is kept throughout the "run" of the program.

This technique with the computer conserves energy and momentum, but volume is not conserved. It is obvious in the latter stages of cratering that the volume of the rock layer which lines the crater is greater than the volume of the incident sphere. This increase in volume results primarily from the numerical method that was employed to follow the interface motion. The present computer code cannot permit a rock-vacuum interface and a rock-aluminum interface to be in one cell at the same time. With this restriction, it is necessary for the rock layer to always be thicker than one cell width; e.g., the rock-aluminum interface can be in cell (L,M), but the rock-vacuum interface can be no closer than cell (L-1,M). As the crater increases in size, the dimensions of the cell increase (see Expansion of Mesh, Chapter III). Forcing the rock layer to always be thicker than one cell width causes the

rock layer to increase in thickness, since the cells periodically increase in size.

It should be emphasized that in each solution, the rock will be entirely ejected from the crater, even though it is still shown in the crater in the last figure of each solution. The velocity vectors in each of these figures indicate that the fluid rock is ejected away from the "set" plastic aluminum. The amounts of momenta and energy found to be carried away by the ejected material, both rock and aluminum, are summarized in Table VI.

TABLE VI

ENERGY AND MOMENTUM OF THE EJECTA AND ENERGY NEEDED TO MELT CRATER

V(km/sec)	D(gm/cc)	RP	RE	RM	E/E_{inc}
6.25	2.0	0.18	0.0001	0.352	0.65
7.5	2.0	0.45	0.002	0.660	0.34
20	2.0	8.99	0.176	0.713	0.11
20	0.5	3.12	0.152	0.590	0.26
72	0.5	12.11	0.240	0.545	0.215

In the table, V is the initial velocity of the sphere and D is the density. The numbers listed under RP are the ratios of the normal component of the momentum that is ejected perpendicularly away from the target to the momentum of the incident sphere. It is quite interesting to note that, for high velocities, the ejected momentum is several times larger than the incident momentum. This momentum from ejecta in the -z direction imparts an equal momentum to the target in the +z

direction. Any experiment which measures the impulse that is imparted to the target should measure an impulse that is larger than the incident momentum. This fact must be kept in mind when interpreting space probe experiments that measure micrometeoroid velocities.

The numbers listed under RE are the ratios of the ejected energy to the energy of the incident sphere. The numbers under RM are the fractions of the energy of the incident sphere that is required to melt a quantity of aluminum which is equal to the volume of the crater. The energy to create the plastic region and to provide the acoustic energy is

$$E = (1 - RE - RM) E_{INC}$$

where E_{inc} is the incident energy of the sphere. It is evident that only a small percentage of the energy appears as plastic deformation and acoustic energy at the higher impact velocities.

CHAPTER V

CONCLUSIONS AND SUGGESTIONS FOR FUTURE WORK

Conclusions

This thesis has presented a numerical solution to extend the theory of shock wave propagation and crater formation that results from hypervelocity impacts. The solution examines the impact of porous, spherical, stone spheres upon a solid aluminum slab. The solution is extended beyond the time when inviscid fluid flow is a valid assumption. Appropriate dynamical equations are developed that account for the viscosity effects of the plastic and elastic zones. Considerable effort is exerted to obtain a valid equation of state for compressed porous rock. An equation of state that was proposed by Tillotson is employed for the fluid range of aluminum, and a curve fitted equation of state is employed for the plastic region of aluminum. The dynamic equations are converted to finite difference equations in an Eulerian coordinate system.

A tag system is developed that permits the physical boundaries of the problem to be accurately tracked through the finite difference mesh. Certain approximations are introduced in order to calculate the partial areas of the cells that are occupied by the physical boundary.

The uniqueness and convergence of the numerical solutions are investigated. The theorem of Lax and the Courant condition are of paramount importance in these investigations.

The numerical solutions are presented in the form of crater diagrams and pressure profiles. Each of these presentations of the numerical results illustrates the effects of the velocity and of the density on the solution. The solutions reveal the presence of strong oscillations within the shocked region and a dual shock wave structure in the plastic region of the problem.

One solution compares the crater created by a sphere of radius (3/2)R with a crater created by a sphere of radius R. The crater depths scale linearly with the diameter of the impacting sphere.

Probably the most important part of the solution is the calculation of the momentum increase and energy decrease by the ejecta. A knowledge of the ejected energy and momentum permits an accurate interpretation of the data from ballistic type micrometeoroid detectors. The ejected momentum is larger than the momentum of the incident sphere, except at low impact velocities. The ratio of the ejecta to sphere momentum increases as the impact velocity increases. The energy of the ejecta is negligible at the lower hypervelocities. It becomes a significant fraction of the incident energy at the higher hypervelocities. The ratio of energy lost in the ejecta to the incident energy also increases as the impact velocity increases.

Suggestions for Future Work

The size of the plastic region obtained in the numerical calculations appears to be too large. The extent of this zone is controlled by the viscosity model that is used in the conservation equations. The viscosity effects of aluminum at pressures above 100 kilobars requires further investigation in order to obtain a more accurate

viscosity model. The pressure at which aluminum converts from a fluid to a plastic material also needs to be established. The calculated thickness of the plastic zone could be in error because the viscosity effects were not included at higher pressures.

More impact solutions are required in order to reach any definitive conclusions about the scaling laws that some have proposed to predict crater depths. The one comparison that was made implies a linear scaling with projectile size, but it cannot be assumed that this linear behavior is valid over the entire range of velocities and densities.

The calculations of the ejected momentum and energy are extremely interesting. Only six points in the entire domain of allowed sphere velocities and densities were evaluated. Similar solutions are desired for several velocity and density values. With these values, perhaps some type of functional dependence between ejected momentum and energy and impact velocity and density may be established.

SELECTED BIBLIOGRAPHY

1. Al'tshuler, L. V., A. A. Bakanova, and R. F. Trunin, Shock Adiabats and Zero Isotherms of Seven Metals at High Pressure, Soviet Phys. - JETP, Vol. 11, No. 1, July, 1962, 65-74.

2. Al'tshuler, L. V., S. B. Kormer, A. A. Bakanova, and R. F. Trunin, Equation of State for Aluminum, Copper, and Lead in the High Pressure Region., Soviet Phys. - JETP, Vol. 11, No. 3, Sept., 1960, 573-579.

3. American Institute of Physics Handbook, McGraw-Hill, 1957, 3-29.

4. Bell, J. F., Single, Temperature-Dependent Stress-Strain Law for the Dynamic Plastic Deformation of Annealed Face-Centered Cubic Metals, J. Appl. Phys., 34, No. 1, Jan., 1963, 1934-141.

5. Bird, R. B., W. E. Stewart, and E. N. Lightfoot, Transport Phenomema, Wiley, 1960.

6. Bradley, R. S., High Pressure Physics and Chemistry, Vol. 2, Academic Press, 1963.

7. Bruce, R. E., A Model and Calculations for the Properties of an Exploding Plasma Sphere, PhD Thesis, Oklahoma State University, 1966.

8. Charters, A. C., Scientific American, Vol. 203, Oct., 1960, 128, ff.

9. Cohen, L. H., W. Klement, and G. C. Kennedy, Melting of Copper, Silver, and Gold at High Pressures, Phy. Rev., 145, No 2, 519-525.

10. Condon, E. U., and H. Odishaw, Handbook of Physics, McGraw-Hill, 1958.

11. 1. c. 10, pp. 3-12.

12. Donn, Bertram, The Origin and Nature of Solid Particles in Space, Annals New York Academy of Science, Vol. 119, Article 1, Nov., 1964.

13. Eirich, F. R., Rheology, Vol. 1, Academic Press, 1956.

14. Gilvarry, J. J., Thermodynamics of the Thomas Fermi Atom at Low Temperatures, The Rand Corporation, P-474, Jan., 1954.

15. Kinslow, R., Properties of Spherical Shock Waves Produced by Hypervelocity Impact. Proc. of Sixth Hypervelocity Impact Symposium, 1963.

16. Kormer, S. B. and V. D. Urlin, Interpolation Equations of State for the Region of Ultrahigh Pressures, Soviet Phys-Doklady, Vol. 5, No. 2, Sept., 1960, 317-320.

17. Kormer, S. B., V. D. Urlin, and L. T. Popova, Interpolation Equation of State and Its Application to Experimental Data on Impact Compression of Metals., Soviet Phys-Solid State, Vol., 3, No. 7, Jan., 1962, 1547-1553.

18. Lake, H. R., Digital Computer Solution for Propagation of a Spherical Shock Wave in Aluminum, Master's Thesis, Oklahoma State University, 1962.

19. Landau, L. D. and E. M. Lifshitz, Theory of Elasticity, Addison-Wesley, 1959, 1-36.

20. Landshoff, R., A Numerical Method for Treating Fluid Flow in the Presence of Shocks, Los Alamos Report LAMS-2379, April, 1959.

21. Latter, R., Equation of State on the Thomas-Fermi Model - Part I: Non-Zero Temperature, Rand Corporation, RM-1227 (AD116576), 1954.

22. Longley, H. J., Methods of Differencing in Eulerian Hydrodynamics, Los Alamos Report LAMS-2379, April, 1959.

23. Lundergan, C. D., The Hugoniot Equation of State of 6061-T6 Aluminum at Low Pressures, SC-4637 (RR), Sept., 1961.

24. Lundergan, C. D. and W. Herrmann, Equation of State of 6061-T6 Aluminum at Low Pressures, J. Appl. Phys., 34, No. 7, July, 1963, 2046-2052.

25. McCloskey, D. J., An Analytical Formulation of Equations of State, Rand Corporation, RM-3905-PR, Feb., 1964.

26. Morse, P. M. and H. Feshbach, Methods of Theoretical Physics, McGraw-Hill, 1953.

27. 1. c. 26, 142.

28. Rich, M., A Method for Eulerian Fluid Dynamics, LAMS-2826, Dec., 1962.

29. Richtmyer, R. D., Difference Methods for Initial-Value Problems, New York: Interscience Publishers, 1957.

30. Riney, T. D., Visco-Plastic Solution of Hypervelocity Impact Cratering Phenomenon, Proc. Sixth Symposium on Hypervelocity Impact, Vol. II, Part 1, Aug., 1963.

31. Riney, T. D. and J. F. Heyda, Hypervelocity Impact Calculations, Proc. Sixth Hypervelocity Impact Symposium, 1963.

32. Sodek, B. A., A Hydrodynamic Model of Micrometeoroid Impact, PhD thesis, Oklahoma State University, 1966.

33. Sodek, B. A. and F. C. Todd, Penetration of an Initially Radial Shock Wave Through an Aluminum-Glass Interface, Proc. Okla. Acad. Sci., Vol. 43, 173-182.

34. Sullivan, E., Theoretical Division, Goddard Space Flight Center, Greenbelt, Maryland, Private Communication.

35. Tillotson, J. H., Metallic Equations of State for Hypervelocity Impact, General Atomic GA-3216, July, 1962.

36. Stewart, H. J., The Energy Equation for a Viscous Compresible Fluid, Proc. Nat. Acad. Sci., Vol. 28, 161-164, (1942).

37. Von Neuman, J., and R. D. Richtmyer, A Method for the Numerical Calculations of Hydrodynamic Shocks, J. Appl. Phys., 21, (1950), 232-237.

38. Wagner, M. H., N. B. Brooks, and R. L. Bjork, Impact of a Porous Aluminum Projectile on Aluminum at 20 and 72 Km/sec., Proc. of Sixth Hypervelocity Impact Symposium, Vol. II, 1963.

39. Walsh, J. M., M. H. Rice, R. G. McQueen and F. Yarger, Shock-Wave Compression of Twenty-Seven Metals. Equations of State of Metals. Phy. Rev. 108, No. 2, Oct., 1957.

40. Smithells, C. J., Metals Reference Book, Volume II, Butterworths Scientific Publications, 1955.

APPENDIX A

EVALUATION OF VISCOUS AND STRAIN RATE TERMS TO USE IN DYNAMICAL EQUATIONS DESCRIBING PLASTIC FLOW

For inviscid fluid flow the radial equation of motion is

$$\frac{\partial}{\partial t}(\rho u) = -\frac{1}{r^2}\frac{\partial}{\partial r}(r^2 \rho u^2) - \frac{\frac{\partial}{\partial \theta}(\rho w u \sin\theta)}{r \sin\theta} + \frac{\rho w^2}{r} - \frac{\partial p}{\partial r} \tag{A1}$$

and the angular equation of motion is

$$\frac{\partial}{\partial t}(\rho w) = -\frac{1}{r^2}\frac{\partial}{\partial r}(r^2 \rho u w) - \frac{\frac{\partial}{\partial \theta}(\rho w^2 \sin\theta)}{r \sin\theta} - \frac{\rho w u}{r} - \frac{1}{r}\frac{\partial p}{\partial \theta} \tag{A2}$$

In plastic flow, viscous terms must be added to these equations of motion. These terms are the r and θ components of the divergence of the stress tensor which is

$$\begin{aligned} \operatorname{div} S_{ij} = {} & \frac{1}{3}\eta\,\vec{\nabla}(\vec{\nabla}\cdot\vec{V}) + \eta\,\nabla^2(\vec{V}) - \frac{2}{3}(\vec{\nabla}\cdot\vec{V})\,\vec{\nabla}\eta \\ & + 2(\vec{\nabla}\eta\cdot\vec{\nabla})\vec{V} + \vec{\nabla}\eta \times (\vec{\nabla}\times\vec{V}) \end{aligned} \tag{A3}$$

In spherical coordinates

$$\vec{\nabla}\cdot\vec{V} = \frac{1}{r^2}\frac{\partial}{\partial r}(r^2 u) + \frac{\frac{\partial}{\partial \theta}(w \sin\theta)}{r \sin\theta} \tag{A4}$$

so the first term of A3 is

$$\frac{1}{3}\eta\,\vec{\nabla}(\vec{\nabla}\cdot\vec{V}) = \frac{1}{3}\eta\left\{\vec{a}_r\frac{\partial}{\partial r}\left[\frac{1}{r^2}\frac{\partial}{\partial r}(r^2u) + \frac{\frac{\partial}{\partial\theta}(w\sin\theta)}{r\sin\theta}\right]\right.$$

(A5)

$$\left. + \vec{a}_\theta\frac{1}{r}\frac{\partial}{\partial\theta}\left[\frac{1}{r^2}\frac{\partial}{\partial r}(r^2u) + \frac{\frac{\partial}{\partial\theta}(w\sin\theta)}{r\sin\theta}\right]\right\}$$

The second term is given by Morse and Feshbach as (26)

$$\eta\nabla^2\vec{V} = \eta\,\vec{a}_r\left[\frac{1}{r^2}\frac{\partial}{\partial r}\left(r^2\frac{\partial u}{\partial r}\right) + \frac{\frac{\partial}{\partial\theta}\left(\frac{\partial u}{\partial\theta}\sin\theta\right)}{r^2\sin\theta}\right.$$

$$\left. - \frac{2u}{r^2} - \frac{2}{r^2\sin\theta}\frac{\partial}{\partial\theta}(w\sin\theta)\right]$$

(A6)

$$+ \eta\,\vec{a}_\theta\left[\frac{1}{r^2}\frac{\partial}{\partial r}\left(r^2\frac{\partial w}{\partial r}\right) + \frac{\frac{\partial}{\partial\theta}\left(\frac{\partial w}{\partial\theta}\sin\theta\right)}{r^2\sin\theta}\right.$$

$$\left. - \frac{w}{r^2\sin^2\theta} + \frac{2}{r^2}\frac{\partial u}{\partial\theta}\right]$$

The third term of A3 is

$$-\frac{2}{3}(\vec{\nabla}\cdot\vec{V})\vec{\nabla}\eta = -\frac{2}{3}\left[\frac{1}{r^2}\frac{\partial}{\partial r}(r^2u) + \frac{\frac{\partial}{\partial\theta}(w\sin\theta)}{r\sin\theta}\right]$$

(A7)

$$*\left[\vec{a}_r\frac{\partial\eta}{\partial r} + \vec{a}_\theta\frac{\partial\eta}{r\partial\theta}\right]$$

and the fourth term is

$$2(\vec{\nabla}\eta\cdot\vec{\nabla})\vec{V} = 2\vec{a}_r\left[\frac{\partial\eta}{\partial r}\frac{\partial u}{\partial r} + \frac{1}{r^2}\frac{\partial\eta}{\partial\theta}\frac{\partial u}{\partial\theta}\right]$$

(A8)

$$+ 2\vec{a}_\theta\left[\frac{\partial\eta}{\partial r}\frac{\partial w}{\partial r} + \frac{1}{r^2}\frac{\partial\eta}{\partial\theta}\frac{\partial w}{\partial\theta}\right]$$

To obtain the last term of A3 let

$$\vec{F} = \vec{\nabla}\times\vec{V} = \frac{1}{r^2\sin\theta}\begin{vmatrix} \vec{a}_r & \vec{a}_\theta & r\sin\theta\,\vec{a}_\phi \\ \frac{\partial}{\partial r} & \frac{\partial}{\partial\theta} & 0 \\ u & rw & 0 \end{vmatrix}$$

then

$$\vec{\nabla}\eta\times(\vec{\nabla}\times\vec{V}) = \begin{vmatrix} \vec{a}_r & \vec{a}_\theta & \vec{a}_\phi \\ \frac{\partial\eta}{\partial r} & \frac{1}{r}\frac{\partial\eta}{\partial\theta} & 0 \\ 0 & 0 & F_\phi \end{vmatrix}$$

or

$$\vec{\nabla}\eta\times(\vec{\nabla}\times\vec{V}) = \vec{a}_r\frac{1}{r}\frac{\partial\eta}{\partial\theta}(F_\phi) - \vec{a}_\theta\frac{\partial\eta}{\partial r}(F_\phi)$$

or

$$\vec{\nabla}\eta \times (\vec{\nabla} \times \vec{V}) = \vec{a}_r \left\{ \frac{1}{r^2} \frac{\partial \eta}{\partial \theta} \left[\frac{\partial}{\partial r}(rw) - \frac{\partial u}{\partial \theta} \right] \right\}$$

$$+ \vec{a}_\theta \frac{\partial \eta}{r \partial r} \left[\frac{\partial u}{\partial \theta} - \frac{\partial}{\partial r}(rw) \right] \tag{A9}$$

The radial equation of motion describing plastic flow is the sum of A1 and the 4 components of A5, A6, A7, A8, and A9 and is

$$\frac{\partial(\rho u)}{\partial t} = -\frac{1}{r^2}\frac{\partial}{\partial r}(r^2 \rho u^2) - \frac{\frac{\partial}{\partial \theta}(\rho w u \sin\theta)}{r \sin\theta} + \frac{\rho w^2}{r} - \frac{\partial p}{\partial r}$$

$$+ \frac{1}{3}\eta \frac{\partial}{\partial r}\left[\frac{1}{r^2}\frac{\partial}{\partial r}(r^2 u) + \frac{\frac{\partial}{\partial \theta}(w \sin\theta)}{r \sin\theta} \right]$$

$$+ \eta \left[\frac{1}{r^2}\frac{\partial}{\partial r}\left(r^2 \frac{\partial u}{\partial r}\right) + \frac{\frac{\partial}{\partial \theta}\left(\frac{\partial u}{\partial \theta}\sin\theta\right)}{r^2 \sin\theta} - \frac{2u}{r^2} \right.$$

$$\left. - \frac{2\frac{\partial}{\partial \theta}(w \sin\theta)}{r^2 \sin\theta} \right] - \frac{2}{3}\frac{\partial \eta}{\partial r}\left[\frac{1}{r^2}\frac{\partial}{\partial r}(r^2 u) \right.$$

$$\left. + \frac{\frac{\partial}{\partial \theta}(w \sin\theta)}{r \sin\theta} \right] + 2\left[\frac{\partial \eta}{\partial r}\frac{\partial u}{\partial r} + \frac{\partial \eta}{r^2 \partial \theta}\frac{\partial u}{\partial \theta} \right]$$

$$+ \frac{1}{r^2}\frac{\partial \eta}{\partial \theta}\left[\frac{\partial}{\partial r}(rw) - \frac{\partial u}{\partial \theta} \right] \tag{A10}$$

The θ component of the equation of motion is the sum of A2 and the θ components of A5, A6, A7, A8, and A9 and is

$$\frac{\partial(\rho w)}{\partial t} = -\frac{1}{r^2}\frac{\partial}{\partial r}(r^2\rho uw) - \frac{\frac{\partial}{\partial\theta}(\rho w^2\sin\theta)}{r\sin\theta} - \frac{\rho wu}{r} - \frac{1}{r}\frac{\partial p}{\partial\theta}$$

$$+\frac{1}{3}\eta\frac{1}{r}\frac{\partial}{\partial\theta}\left[\frac{1}{r^2}\frac{\partial}{\partial r}(r^2u) + \frac{\frac{\partial}{\partial\theta}(w\sin\theta)}{r\sin\theta}\right] + \eta\left[\frac{1}{r^2}\frac{\partial}{\partial r}\left(r^2\frac{\partial w}{\partial r}\right)\right.$$

(A11)

$$\left. + \frac{\frac{\partial}{\partial\theta}\left(\frac{\partial w}{\partial\theta}\sin\theta\right)}{r^2\sin\theta} - \frac{w}{r^2\sin^2\theta} + \frac{2}{r^2}\frac{\partial u}{\partial\theta}\right]$$

$$-\frac{2}{3}\frac{\partial\eta}{r\partial\theta}\left[\frac{1}{r^2}\frac{\partial}{\partial r}(r^2u) + \frac{\frac{\partial}{\partial\theta}(w\sin\theta)}{r\sin\theta}\right]$$

$$+2\left[\frac{\partial\eta}{\partial r}\frac{\partial w}{\partial r} + \frac{1}{r^2}\frac{\partial\eta}{\partial\theta}\frac{\partial w}{\partial\theta}\right] - \frac{1}{r}\frac{\partial\eta}{\partial r}\left[\frac{\partial}{\partial r}(rw) - \frac{\partial u}{\partial\theta}\right]$$

For inviscid fluid flow, the energy equation is

$$\frac{\partial(\rho E)}{\partial t} = -\frac{1}{r^2}\frac{\partial}{\partial r}(r^2\rho uE) - \frac{\frac{\partial}{\partial\theta}(\rho wE\sin\theta)}{r\sin\theta}$$

(A12)

$$-\frac{1}{r^2}\frac{\partial}{\partial r}(r^2pu) - \frac{\frac{\partial}{\partial\theta}(pw\sin\theta)}{r\sin\theta}$$

The viscous effects of plastic flow are included in the energy equation by adding $\nabla\cdot(S_{ij}V_i)$ to A12. $S_{ij}\ V_i$ is the vector of rank one resulting from the product of the dyad S with the flow velocity V.

(A13) $$\nabla\cdot(S_{ij}V_i) = S_{ij}\,\nabla\cdot V_i + V_i\,\nabla\cdot S_{ij}$$

The term $\nabla \cdot S_{ij}$ has already been evaluated in equations A3 to A9. The last term of A13 is then

$$
\begin{aligned}
V_i \; \nabla \cdot S_{ij} = u \Bigg\{ & \frac{1}{3}\eta \frac{\partial}{\partial r}\left[\operatorname{div} \vec{V}\right] + \eta\left[\frac{1}{r^2}\frac{\partial}{\partial r}\left(r^2 \frac{\partial u}{\partial r}\right)\right. \\
& + \frac{\frac{\partial}{\partial \theta}\left(\frac{\partial u}{\partial \theta}\sin\theta\right)}{r^2 \sin\theta} - \frac{2u}{r^2} - \frac{2\frac{\partial}{\partial \theta}(w \sin\theta)}{r^2 \sin\theta} \\
& - \frac{2}{3}\frac{\partial \eta}{\partial r} \operatorname{div} \vec{V} + 2\left[\frac{\partial \eta}{\partial r}\frac{\partial u}{\partial r} + \frac{1}{r^2}\frac{\partial \eta}{\partial \theta}\frac{\partial u}{\partial \theta}\right] \\
& \left. + \frac{1}{r^2}\frac{\partial \eta}{\partial \theta}\left[\frac{\partial}{\partial r}(rw) - \frac{\partial u}{\partial \theta}\right] \right\} \\
& + w \Bigg\{ \frac{1}{3}\eta \frac{\partial}{r \partial \theta}\left[\operatorname{div} \vec{V}\right] + \eta\left[\frac{1}{r^2}\frac{\partial}{\partial r}\left(r^2 \frac{\partial w}{\partial r}\right)\right. \\
& + \frac{\frac{\partial}{\partial \theta}\left(\frac{\partial w}{\partial \theta}\sin\theta\right)}{r^2 \sin\theta} - \frac{w}{r^2 \sin^2\theta} + \frac{2}{r^2}\frac{\partial u}{\partial \theta}\Bigg] \\
& - \frac{2}{3}\frac{\partial \eta}{r \partial \theta}\left[\operatorname{div} \vec{V}\right] + 2\left[\frac{\partial \eta}{\partial r}\frac{\partial w}{\partial r} + \frac{1}{r^2}\frac{\partial \eta}{\partial \theta}\frac{\partial w}{\partial \theta}\right] \\
& \left. - \frac{1}{r}\frac{\partial \eta}{\partial r}\left[\frac{\partial}{\partial r}(rw) - \frac{\partial u}{\partial \theta}\right] \right\}
\end{aligned}
\tag{A14}
$$

In the two dimensions, r and ~~θ~~, used in this problem, the components of S_{ij} are

$$S_{rr} = \frac{\partial u}{\partial r}$$

$$S_{\theta\theta} = \frac{1}{r}\frac{\partial w}{\partial \theta} + \frac{u}{r}$$

(A15)

$$S_{r\theta} = \frac{1}{2}\left(\frac{1}{r}\frac{\partial u}{\partial \theta} + \frac{\partial w}{\partial r} - \frac{w}{r}\right)$$

$$S_{\phi\phi} = \frac{u}{r} + \frac{w \cot\theta}{r}$$

A useful identity is

$$\operatorname{div} \vec{V} = \frac{1}{r^2}\frac{\partial}{\partial r}(r^2 u) + \frac{\frac{\partial}{\partial \theta}(w \sin\theta)}{r \sin\theta} = \frac{\partial u}{\partial r} + \frac{2u}{r} + \frac{\partial w}{r\,\partial\theta} + \frac{w\cot\theta}{r}$$

or

$$\text{(A16)} \qquad \operatorname{div} \vec{V} = S_{rr} + S_{\theta\theta} + S_{\phi\phi}$$

Thus the first term of A13 is

$$S_{ij}\,\vec{\nabla}_i \vec{V} = \left(S_{rr} + S_{\theta\theta} + S_{\phi\phi} + S_{r\theta}\right) \operatorname{div} \vec{V}$$

or

$$\text{(A17)} \quad S_{ij}\,\vec{\nabla}_i \vec{V} = \left[\operatorname{div} \vec{V} + \frac{1}{2}\left(\frac{1}{r}\frac{\partial u}{\partial \theta} + \frac{\partial w}{\partial r} - \frac{w}{r}\right)\right] \operatorname{div} \vec{V}$$

The energy equation for the plastic zone is obtained by adding

A14 and A17 to the right side of A12.

The conservation of mass equation for the plastic zone is identical to the form used in the inviscid fluid model.

APPENDIX B

EVALUATION OF THE ELASTIC STRESS TENSOR TERMS TO INCLUDE IN THE DYNAMICAL EQUATIONS DESCRIBING THE ELASTIC ZONE

In the elastic zone, the elastic stress tensor must be included in the equation of motion and the energy equation. The conservation of mass equation is not changed from the form used in the inviscid fluid model.

The elastic stress tensor is

$$S_{ij} = \lambda e_{ij} \delta_{ij} + 2\mu e_{ij} \tag{B1}$$

where the e_{ij} are the components of the strain tensor

$$e_{ij} = \frac{1}{2}\left(\frac{\partial y_i}{\partial x_j} + \frac{\partial y_j}{\partial x_i}\right) \tag{B2}$$

The y_i and y_j are the components of the displacement vector of the material resulting from elastic deformation only. Let u be the flow velocity of the material in the radial direction, and w be the flow velocity in the θ direction. The radial elastic displacement during a short time dt is then

$$y_r = u\,dt \tag{B3}$$

and the elastic displacement in the θ direction during dt is

$$y_\theta = w\,dt \tag{B4}$$

It should be emphasized that u and w are not the components of the elastic wave velocity but are the components of the material flow velocity behind the elastic wave front.

The elastic constants λ and μ are given by

$$\lambda = \frac{E\sigma}{(1-2\sigma)(1+\sigma)} \tag{B5}$$

and

$$\mu = \frac{E}{2(1+\sigma)} \tag{B6}$$

where E is Young's modulus, and σ is Poisson's ratio.

The term which must be added to the equation of motion is (27)

$$\nabla \cdot S_{ij} = (\lambda+\mu)\,\vec{\nabla}(\vec{\nabla}\cdot\vec{r}) + \mu\nabla^2(\vec{r}) \tag{B7}$$

$\vec{r}$ is the displacement vector, and in the two dimensions r and θ

$$\vec{r} = (y_r, y_\theta, 0)$$

Therefore

$$\vec{\nabla}\cdot\vec{r} = \frac{1}{r^2}\frac{\partial}{\partial r}(r^2 y_r) + \frac{\frac{\partial}{\partial\theta}(y_\theta \sin\theta)}{r\sin\theta}$$

and the first term of B7 is

$$(\lambda+\mu)\vec{\nabla}(\vec{\nabla}\cdot\vec{r}) = \vec{a}_r(\lambda+\mu)\frac{\partial}{\partial r}\left[\frac{1}{r^2}\frac{\partial}{\partial r}(r^2 y_r) + \frac{\frac{\partial}{\partial\theta}(y_\theta\sin\theta)}{r\sin\theta}\right]$$

$$+\vec{a}_\theta(\lambda+\mu)\frac{\partial}{r\partial\theta}\left[\frac{1}{r^2}\frac{\partial}{\partial r}(r^2 y_r) + \frac{\frac{\partial}{\partial\theta}(y_\theta\sin\theta)}{r\sin\theta}\right] \tag{B8}$$

The second term in B7 can be found from a vector identity (26)

$$\mu\nabla^2(\vec{\pi}) = \vec{a}_r\mu\left[\nabla^2 y_r - \frac{2}{r^2}y_r - \frac{2\frac{\partial}{\partial\theta}(y_\theta\sin\theta)}{r^2\sin\theta}\right]$$

$$+\vec{a}_\theta\mu\left[\nabla^2 y_\theta - \frac{y_\theta}{r^2\sin^2\theta} + \frac{2}{r^2}\frac{\partial y_r}{\partial\theta}\right]$$

or

$$\mu\nabla^2(\vec{\pi}) = \vec{a}_r\mu\left[\frac{1}{r^2}\frac{\partial}{\partial r}\left(r^2\frac{\partial y_r}{\partial r}\right) + \frac{\frac{\partial}{\partial\theta}\left(\frac{\partial y_\theta}{\partial\theta}\sin\theta\right)}{r^2\sin\theta}\right.$$

(B9)

$$\left. - \frac{2y_r}{r^2} - \frac{2\frac{\partial}{\partial\theta}(y_\theta\sin\theta)}{r^2\sin\theta}\right] + \vec{a}_\theta\mu\left[\frac{1}{r^2}\frac{\partial}{\partial r}\left(r^2\frac{\partial y_r}{\partial r}\right)\right.$$

$$\left. + \frac{\frac{\partial}{\partial\theta}\left(\frac{\partial y_\theta}{\partial\theta}\sin\theta\right)}{r^2\sin\theta} - \frac{y_\theta}{r^2\sin^2\theta} + \frac{2}{r^2}\frac{\partial y_r}{\partial\theta}\right]$$

The radial motion equation describing elastic flow is obtained by adding the r components of B8 and B9 to the inviscid fluid radial motion equation; the result is

$$\frac{\partial(\rho u)}{\partial t} = -\frac{1}{r^2}\frac{\partial}{\partial r}(r^2\rho u^2) - \frac{\partial_\theta(\rho w u\sin\theta)}{r\sin\theta} + \frac{\rho w^2}{r} - \frac{\partial p}{\partial r}$$

$$+(\lambda+\mu)\frac{\partial}{\partial r}\left[\frac{1}{r^2}\frac{\partial}{\partial r}(r^2 y_r) + \frac{\frac{\partial}{\partial\theta}(y_\theta\sin\theta)}{r\sin\theta}\right] + \mu\left[\frac{1}{r^2}\frac{\partial}{\partial r}\left(r^2\frac{\partial y_r}{\partial r}\right)\right.$$

(B10)

$$\left. + \frac{\frac{\partial}{\partial\theta}\left(\frac{\partial y_\theta}{\partial\theta}\sin\theta\right)}{r^2\sin\theta} - \frac{2y_r}{r^2} - \frac{2\frac{\partial}{\partial\theta}(y_\theta\sin\theta)}{r^2\sin\theta}\right]$$

Adding the θ component of B8 and B9 to the θ motion equation describing inviscid fluid flow gives the elastic motion equation

$$\frac{\partial(\rho w)}{\partial t} = -\frac{1}{r^2}\frac{\partial}{\partial r}(r^2 \rho u w) - \frac{\frac{\partial}{\partial \theta}(\rho w^2 \sin\theta)}{r \sin\theta} - \frac{\rho w u}{r} - \frac{1}{r}\frac{\partial p}{\partial \theta}$$

$$+ (\lambda+\mu)\frac{\partial}{r\partial\theta}\left[\frac{1}{r^2}\frac{\partial}{\partial r}(r^2 y_r) + \frac{\frac{\partial}{\partial\theta}(y_\theta \sin\theta)}{r\sin\theta}\right] + \mu\left[\frac{1}{r^2}\frac{\partial}{\partial r}\left(r^2\frac{\partial y_\theta}{\partial r}\right)\right. \tag{B11}$$

$$\left. + \frac{\frac{\partial}{\partial\theta}\left(\frac{\partial y_\theta}{\partial\theta}\sin\theta\right)}{r^2\sin\theta} - \frac{y_\theta}{r^2\sin^2\theta} + \frac{2}{r^2}\frac{\partial y_r}{\partial\theta}\right]$$

The elastic energy equation must include the term $div(S_{ij} V_i)$ which is

$$div(S_{ij} V_i) = S_{ij} \nabla \cdot V_i + V_i \nabla \cdot S_{ij} \tag{B12}$$

The S_{ij} components are (19)

$$S_{rr} = \frac{\partial y_r}{\partial r}$$

$$S_{\theta\theta} = \frac{1}{r}\frac{\partial y_\theta}{\partial\theta} + \frac{y_r}{r}$$

$$S_{\phi\phi} = \frac{y_\theta}{r}\cot\theta + \frac{y_r}{r}$$

$$S_{r\theta} = \frac{1}{2}\left(\frac{\partial y_\theta}{\partial r} - \frac{y_\theta}{r} + \frac{1}{r}\frac{\partial y_r}{\partial\theta}\right)$$

The first term of B12 is then

$$\left[\frac{\partial \gamma_r}{\partial r} + \frac{1}{r}\frac{\partial \gamma_\theta}{\partial \theta} + 2\frac{\gamma_r}{r} + \frac{1}{2}\left(\frac{\partial \gamma_\theta}{\partial r} - \frac{\gamma_\theta}{r} + \frac{1}{r}\frac{\partial \gamma_r}{\partial \theta}\right) + \frac{\gamma_\theta}{r}\cot\theta\right] \operatorname{div} \vec{V} \tag{B13}$$

The second term of B12 is the dot product of the flow vector

$$\vec{V} = (u, w, 0)$$

with the vector $\nabla \cdot S_{ij}$ evaluated in B7 to B9. Adding this dot product and the terms in B13 to the energy equation for inviscid fluid flow gives the energy equation for the elastic zone.

VITA

Bob Adrian Hardage

Candidate for the Degree of

Doctor of Philosophy

Thesis: HYPERVELOCITY IMPACT WITH FLOW AND SHOCK PENETRATION THROUGH FLUID, PLASTIC, AND ELASTIC ZONES

Major Field: Physics

Biographical:

Personal Data: Born in Checotah, Oklahoma, April 5, 1939, the son of Charles M. and Edna Hardage.

Education: Graduated from Onapa Public School, 1957; received Bachelor of Science degree from Oklahoma State University, with a major in Physics, in May, 1961. Entered the Oklahoma State University Graduate College in 1961; completing requirements for the Master of Science and Doctor of Philosophy degrees in 1967.

Professional Experience: Employed as programmer by Oklahoma State University computing center in summer of 1960, and as teaching assistant for the Physics Department in summer of 1961. Employed as research physicist for Phillips Petroleum Company in 1966. Member of Oklahoma Academy of Science and Society of Exploration Geophysicists.